

2009

A FLOW-THROUGH ACOUSTIC WAVEGUIDE FOR TWO-PHASE BUBBLY FLOW VOID FRACTION MEASUREMENT

<https://hdl.handle.net/2144/1382>

Boston University

BOSTON UNIVERSITY
COLLEGE OF ENGINEERING

Thesis

**A FLOW-THROUGH ACOUSTIC WAVEGUIDE FOR
TWO-PHASE BUBBLY FLOW VOID FRACTION MEASUREMENT**

by

CHRISTOPHER EDWARD ORMONDE

B. S., Boston University, 2006

Submitted in partial fulfillment of the

requirements for the degree of

Master of Science

2009

© Copyright

CHRISTOPHER EDWARD ORMONDE

2009

Approved by

Advisor:

Ronald A. Roy, Ph.D.
Chairman, Mechanical Engineering

Second Reader:

R. Glynn Holt, Ph.D.
Associate Professor, Mechanical Engineering

Third Reader:

J. Gregory McDaniel, Ph.D.
Associate Professor, Mechanical Engineering

ACKNOWLEDGEMENTS

Graduate research almost always involves spending long days alone, pushing buttons on oscilloscopes and muttering profanities late at night in an empty lab. However, when writing a thesis or dissertation and trying to bring a degree to a close, there is always a long list of people who have supported that student in many ways during those long periods of solitary confinement.

As an only child from a small family, thanks first and foremost will always go to my parents, Henry and Lesley, in everything that I do. Their support and willingness to bend over backwards to help me in any possible way has never faltered. From showing up with some groceries during a time of particular distress, to giving me their valued opinions making difficult life decisions, they are always there. They are truly the best parents a child could ask for.

To my 'chief' advisor, Ronald A. Roy, I owe a huge 'thank you'. Ron, although always busy, was always available for a discussion or brainstorm session. Many a time I would catch Ron with his coat on, intending to finally head home for the night after a long and busy day, instead to find us both in the lab for another hour bouncing ideas off of each other. Ron is truly an 'outside the box' thinker and his patience, guidance, and desire to help me at all times will not be forgotten.

To my 'other' advisors and readers, I also owe much thanks.

Robin O. Cleveland has always been available with an office door ajar, even at odd hours. In weekly meetings he would always keep sight of the end goal, and provide helpful scientific suggestions. R. Glynn Holt has provided much guidance both directly project related and otherwise. His ability to get down to the nitty-gritty physics was always helpful in diagnosing problems as well. J. Gregory McDaniel's interest in this project and willingness to join the committee is also greatly appreciated.

To my fellow graduate students I also owe thanks. Between helping to diagnose an issue in the lab to just having someone to chat with, they are the only other folks who know what graduate research entails and are always around to take a quick breather. Zachary Waters, Jon Kracht, and Nick Manzi, specifically, have been not only fellow students but also friends.

To all of my non-engineering friends, although it may have been difficult to balance work and pleasure at times, I owe much thanks for their patience and all the good times I was able to have when escaping the insanity of graduate school for short periods of time. The support of my best friend and 'pseudo-sister', Ellyn Roth, although expected and never doubted, is greatly appreciated.

This work was supported by the Oak Ridge National Laboratory (ORNL) Spallation Neutron Source (SNS), which is managed by UT-Battelle, LLC, under contract DE-AC05-00OR22725 for the U.S. Department of Energy (US-DOE). This gracious financial assistance is greatly appreciated.

Bernie Riemer, Mark Wendel, and Dave Felde are also owed thanks for their support of this project and input from the SNS camp.

**A FLOW-THROUGH ACOUSTIC WAVEGUIDE FOR
TWO-PHASE BUBBLY FLOW VOID FRACTION MEASUREMENT**

CHRISTOPHER EDWARD ORMONDE

ABSTRACT

In the Spallation Neutron Source (SNS) facility at Oak Ridge National Laboratory (ORNL), the deposition of a high-energy proton beam into the liquid mercury target forms bubbles whose asymmetric collapse cause Cavitation Damage Erosion (CDE) to the container walls, thereby reducing its usable lifetime. One proposed solution for mitigation of this damage is to inject a population of microbubbles into the mercury, yielding a compliant and attenuative medium that will reduce the resulting cavitation damage. This potential solution presents the task of creating a diagnostic tool to monitor bubble population in the mercury flow in order to correlate void fraction and damage.

Details of an acoustic waveguide for the eventual measurement of two-phase mercury-helium flow void fraction are discussed. The assembly's waveguide is a vertically oriented stainless steel cylinder with 5.08cm ID, 1.27cm wall thickness and 40cm length. For water experiments, a 2.54cm thick stainless steel plate at the bottom supports the fluid, provides an acoustically rigid boundary condition, and is the mounting point for a hydrophone. A port near the bottom is the inlet for the fluid of interest. A spillover reservoir welded to the upper portion of the main tube

allows for a flow-through design, yielding a pressure release top boundary condition for the waveguide. A cover on the reservoir supports an electrodynamic shaker that is driven by linear frequency sweeps to excite the tube. The hydrophone captures the frequency response of the waveguide. The sound speed of the flowing medium is calculated, assuming a linear dependence of axial mode number on modal frequency (plane wave). Assuming that the medium has an effective-mixture sound speed, and that it contains bubbles which are much smaller than the resonance radii at the highest frequency of interest (Wood's limit), the void fraction of the flow is calculated. Results for water and bubbly water of varying void fraction are presented, and serve to demonstrate the accuracy and precision of the apparatus. [Supported by the ORNL Spallation Neutron Source, which is managed by UT-Battelle, LLC, under contract DE-AC05-00OR22725 for the U.S. Department of Energy.]

Table of contents

1	Introduction and Background	1
1.1	Context and Motivation.....	1
1.1.1	SNS Facility Description and Function	1
1.1.2	Cavitation.....	8
1.1.3	Target Damage Effect.....	9
1.1.4	Possible Cavitation Mitigation Solution.....	13
1.1.5	Statement of Posed Problem	15
1.2	Previous Bubbly Flow Characterization Techniques	16
1.2.1	Electrical methods.....	16
1.2.2	Fluidic Methods.....	17
1.2.3	Irradiation Methods.....	18
1.2.4	Optical Methods	18
1.2.5	Acoustic Methods	19
1.3	Formal Problem Statement	20
2	Theory	21

2.1	Bubbly Fluid Acoustics.....	22
2.1.1	Bubbly Fluid Sound Speed Derivation.....	22
2.1.2	Sound Propagation Including Bubble Dynamics.....	25
2.1.3	Low Frequency Sound Propagation.....	38
2.2	Waveguide Acoustics.....	42
2.2.1	Standing Plane Wave Propagation in a Rigid-wall Tube.....	43
2.2.2	Resonances of a Driven Tube.....	46
2.2.3	Plane Wave Resonance Modes.....	51
2.2.4	Non-ideal End Conditions.....	52
2.2.5	Elastic Waveguide Effect.....	52
2.3	Combination.....	62
3	Materials and Methods.....	63
3.1	Acoustic Resonator Development.....	63
3.1.1	Basic Proposed Design.....	64
3.1.2	Parameter Choices and Justifications.....	68
3.2	Acoustic Resonator Description.....	82

3.2.1	Main Resonator Assembly.....	82
3.2.2	Flow Loop.....	90
3.2.3	Bubbler and Gas Metering System.....	91
3.2.4	Auxiliary Equipment.....	95
3.3	Overall System.....	97
3.4	Experimental Method.....	99
3.4.1	Experimental Setup - Pure Water.....	99
3.4.2	Experimental Setup – Bubbly Water.....	100
3.4.3	MATLAB Code – Initialization and Signal Generation.....	101
3.4.4	MATLAB Code – Data Output and Acquisition.....	103
3.4.5	MATLAB Code – Post-processing and modeling.....	103
3.4.6	Image Processing – Bubbly Water.....	105
4	Results and Discussion.....	107
4.1	Pure Water Results.....	107
4.2	Bubbly Water Results.....	119
4.2.1	Wall Attachment Phenomenon.....	119

4.2.2	Bubbly Water Benchmark Experiment.....	127
4.2.3	Bubble Rise Velocity Correction and Results.....	133
5	Conclusion and Path Forward.....	150
A	Engineering Drawings.....	153
	Bibliography.....	163
	Vita.....	171

List of Tables

Table 3.1: Tables of material parameters used for simulations and calculations 69

Table 3.2: Relevant values that determine the dimensions of the cylindrical resonator for water 79

Table 3.3: Relevant values that determine the dimensions of the cylindrical resonator for Mercury 79

List of Figures

Figure 1.1: Layout of the ORNL SNS Complex (neutrons.ornl.gov).....	3
Figure 1.2: The SNS Liquid-mercury-filled Stainless Steel Target Chamber (Courtesy B. Riemer, ORNL SNS)	6
Figure 1.3: A cutaway view of the SNS mercury target, showing flow path, relative size scale, and cooling channels (courtesy B. Riemer, ORNL SNS)	7
Figure 1.4: A bubble implodes near a solid surface. The presence of the solid causes the collapse to be asymmetrical, forming a high-speed jet of liquid that impacts the surface. (from L. A. Crum, Ph.D., University of Washington, Applied Physics Laboratory). Bubble diameter approximately 1mm.....	10
Figure 1.5: High-speed camera photo series of bubble cloud collapse mechanism on a rigid target due to a single shock wave. Shock waves were fired from an electromagnetic Storz SLX lithotripter with the target positioned at the focus. The first frame (top left) was taken 200 microseconds after the lithotripter was triggered, successive photos were taken every 50 microseconds following. Left to right, top to bottom indicate increasing time (Courtesy Jon Kracht and Robin Cleveland).....	12
Figure 2.1: Phase speed versus frequency for a monodisperse bubbly mixture of water and air with bubble radius 1mm and void fraction 1E-3 from Equation (2.14)	29
Figure 2.2: Attenuation versus frequency for a monodisperse bubbly mixture of water and air with bubble radius of 1mm and void fraction 1E-3 from Equation (2.15)	30

Figure 2.3: Phase speed versus frequency for three monodisperse bubbly mixtures of water and air with bubble radius 1mm and void fractions of 1E-5 (gray dotted line), 1E-4 (dashed line), and 1E-3 (solid line) from Equation (2.14) 33

Figure 2.4: Attenuation versus frequency for three monodisperse bubbly mixtures of water and air with bubble radius 1mm and void fractions of 1E-5 (gray dotted line), 1E-4 (dashed line), and 1E-3 (solid line) from Equation (2.15)..... 34

Figure 2.5: Phase speed versus frequency for three monodisperse bubbly mixtures of water and air with void fraction 1E-3 and bubble radii of 0.1mm (gray dotted line), 1mm (dashed line), and 5mm (solid line) from Equation (2.14) 35

Figure 2.6: Attenuation versus frequency for three monodisperse bubbly mixtures of water and air with void fraction 1E-3 and bubble radii of 0.1mm (gray dotted line), 1mm (dashed line), and 5mm (solid line) from Equation (2.15)..... 36

Figure 2.7: Relationship between sound speed and void fraction for air bubbles in water at STP (solid line) and helium bubbles in mercury (dashed line) from Equation (2.18)..... 41

Figure 2.8: Waterfall plot of frequency responses (response level versus frequency) versus position for a stainless steel waveguide of length 69cm, radius 2.5cm, and wall thickness 2.5cm, filled with degassed water and driven with Gaussian noise. A hydrophone was used to take frequency response measurements at positions along the axis of the tube spaced by 5cm each..... 49

Figure 2.9: Coordinate system used to describe waves in a liquid contained in an elastic tube of inner radius b and outer radius d . Modes under consideration are θ -independent axisymmetric modes (from Lafleur and Shields [58]) 55

Figure 2.10: Phase velocity versus frequency for an aluminum water-filled waveguide with inner and outer radii of 25.4mm and 38.1mm, respectively. The

solid circles represent measured phase velocity values (from Lafleur and Shields [58])	61
Figure 3.1: Computed phase speed versus frequency for a water-filled waveguide with wall thickness ranging from 6.35mm to 101.6mm. Intrinsic sound speed of the fluid is 1497 m/s.....	71
Figure 3.2: Computed phase speed versus frequency for a mercury-filled waveguide with wall thickness ranging from 6.35mm to 101.6mm. Intrinsic sound speed of the fluid is 1450 m/s.....	72
Figure 3.3: Real and imaginary parts of the plane wave reflection coefficient versus frequency for a three-medium scenario of water, 1" of stainless steel, and air. The data points place on the x-axis indicate the resonance modes of a 40 cm tube for both perfectly rigid (asterisks) and pure pressure release (crosses) conditions.	75
Figure 3.4: Detailed schematic of the Boston University acoustic resonator assembly	87
Figure 3.5: Three-dimensional CAD model of the resonator assembly.....	88
Figure 3.6: The acoustic resonator assembly. In this particular photograph the shaker cover is not attached, and the reservoir outlet tubing is disconnected.....	89
Figure 3.7: Bubbler and gas metering system	94
Figure 3.8: Diagram of the Boston University acoustic resonator system in its entirety (not to scale).....	98
Figure 4.1: Measured hydrophone signal post-amplification and filtering versus time for the resonator filled with pure, degassed water and driven by a 200ms linear sweep from 0-5 kHz.....	109

Figure 4.2: Average frequency response level versus frequency for the resonator filled with pure, degassed water and driven by six 200ms linear sweeps from 0-5 kHz.....	111
Figure 4.3: Plot of mode number versus frequency for the modal peaks extracted from the spectrum in Figure 4.2	114
Figure 4.4: Sound speed distribution for a 100-measurement precision investigation over 16 hours	118
Figure 4.5: Frequency response level vs. frequency for the resonator flowing newly-introduced bubbly water at the approximate moment it has completely filled the tube, driven by 200 ms linear sweeps from 0-5 kHz	121
Figure 4.6: Frequency response level versus frequency for the resonator 20 seconds after the approximate moment the tube is first filled with bubbly fluid, driven by five 200 ms linear sweeps from 0-5 kHz.....	123
Figure 4.7: Frequency response level versus frequency for the resonator after five minutes of flowing bubbly water, driven by five 200 ms linear sweeps from 0-5 kHz	124
Figure 4.8: Frequency response level versus frequency for the resonator after flowing non-bubbly water for two minutes following a bubbly mixture experiment (bubbles remain on the tube wall), driven by five 200 ms linear frequency sweeps from 0-5 kHz.....	126
Figure 4.9: Sound speed versus injected void fraction for bubbly water resonator measurements of 26 different air flow rates. The independent variable is derived from measured liquid and gas flow rates via Equation (4.4)	130

Figure 4.10: Sound speed versus injected void fraction for bubbly water resonator measurements of 26 different air flow rates. The independent variable is based upon liquid and gas flow rates via Equation (4.4)132

Figure 4.11: Bubbly image captured for an air flow rate of 0.6 SCCM; this corresponds to a corrected injected void fraction of 1.92E-4. Blue circles indicate bubbles chosen via the image processing algorithm.136

Figure 4.12: Histogram of bubble diameters corresponding to Figure 4.11. Diameters were calculated using a calibration of 14.4 microns per pixel.137

Figure 4.13: Bubbly image captured for an air flow rate of 5.0 SCCM; this corresponds to a corrected injected void fraction of 1.37E-3. Blue circles indicate bubbles chosen via the image processing algorithm.138

Figure 4.14: Histogram of bubble diameters corresponding to Figure 4.13. Diameters were calculated using a calibration of 14.4 microns per pixel.139

Figure 4.15: Bubbly image captured for an air flow rate of 50 SCCM; this corresponds to a corrected injected void fraction of 1.40E-2. Blue circles indicate bubbles chosen via the image processing algorithm.140

Figure 4.16: Histogram of bubble diameters corresponding to Figure 4.15. Diameters were calculated using a calibration of 14.4 microns per pixel.141

Figure 4.17: Sound speed versus injected void fraction for bubbly water resonator measurements of 26 different air flow rates. The independent variable is based upon a rise velocity and tube volume.143

Figure 4.18: Sound speed versus injected void fraction for bubbly water resonator measurements of 26 different air flow rates. The independent variable is based upon a rise velocity and tube volume.145

Figure A.1: Engineering drawing of the main resonator tube.....	154
Figure A.2: Engineering drawing of the base support plate	155
Figure A.3: Engineering drawing of the inlet section	156
Figure A.4: Engineering drawing of the intermediate support plate	157
Figure A.5: Engineering drawing of the spillover reservoir	158
Figure A.6: Engineering drawing of the reservoir lid	159
Figure A.7: Engineering drawing of the shaker cover	160
Figure A.8: Engineering drawing of the piston driver	161
Figure A.9: Engineering drawing of the thin end plate	162

Chapter 1

1 Introduction and Background

This thesis details the design, construction, and validation of a flow-through acoustic resonator for determining the void fraction of a two-phase flow via sound speed measurement. This Section will detail the motivation behind the construction of such a device, a discussion of techniques previously employed by others to make similar measurements, and a formal posing of the task at hand.

1.1 Context and Motivation

This Section will detail the motivation behind the current work, and the context which makes it relevant and important.

1.1.1 SNS Facility Description and Function

When at full power (order 1MW) and maximum pulse repetition frequency (PRF=60Hz), the Spallation Neutron Source (SNS) at Oak Ridge National Laboratory

(ORNL) will be the most intense pulsed accelerator-based neutron source in the world. Neutrons of different energies can be used in a wide variety of experiments. Neutrons are ideal for the investigation of material properties in that they are able to penetrate materials very easily, and the manner in which they interact with a material yields vast amounts of insight into its properties. Neutron science has been at the forefront of materials science for decades, and the SNS puts the United States back in the lead for the most cutting-edge neutron science facility, as it will produce more neutrons than any other facility in the world. Below in Figure 1.1 is shown the Layout of the ORNL SNS facility, and the corresponding National Laboratories which collaborate on the specific portions of the facility.

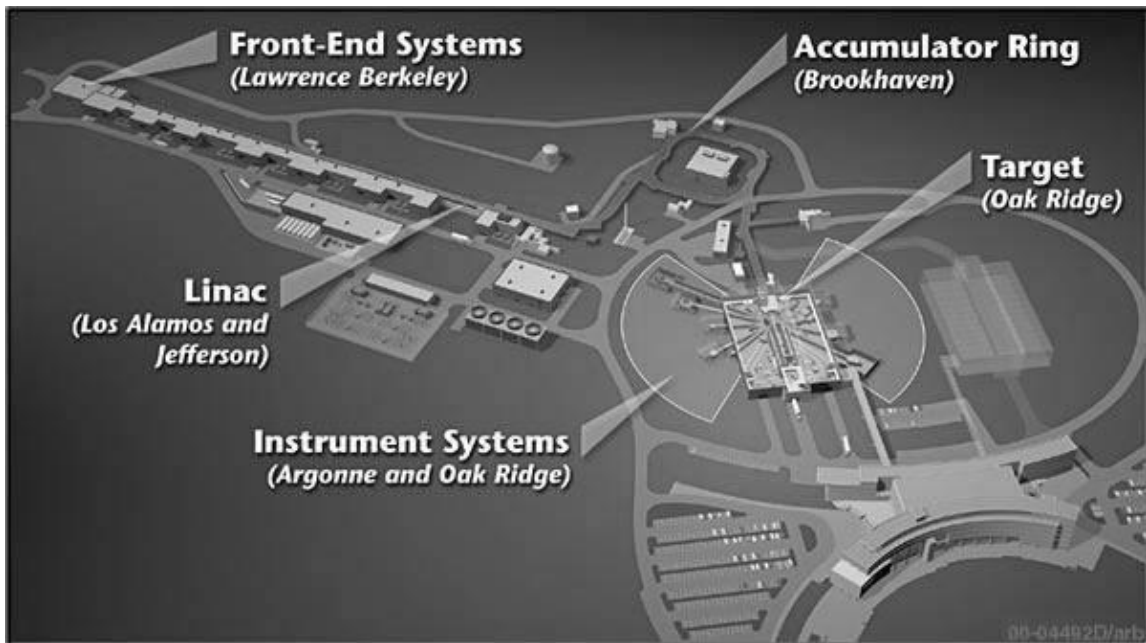


Figure 1.1: Layout of the ORNL SNS Complex (neutrons.ornl.gov)

The SNS functions as follows: Negatively charged hydrogen ions are produced by an ion source. Each ion consists of a proton orbited by two electrons. The ions are routed into a 1000-foot linear accelerator that accelerates them to about 90% of the speed of light. The ions are passed through a foil, which strips off each ion's two electrons, converting it to a single proton. The protons then enter into an accumulator ring, where they are collected into bunches as they circulate and are accelerated further very close to the speed of light. The pulsed beam of high-energy protons (order 1 GeV) is fired at a stainless steel liquid-mercury-filled target. When a very high energy proton collides with a mercury atom, neutrons are 'knocked off' the atom in a process called spallation. The corresponding pulse of neutrons is emitted isotropically, slowed down in a moderator and guided through beam lines (a waveguide of sorts) to dedicated experiments positioned at the end of each line. The SNS main target has 18 beam lines/instruments emanating from it. A second target is slated for construction and will house more beam lines.

The target, shown below in Figure 1.2, is a stainless steel container filled with continuously re-circulating liquid mercury. Because of the enormous amount of energy that the short, powerful pulses of the incoming 1-GeV proton beam will deposit in the spallation target, it was decided to use a liquid mercury target rather than a solid in order to facilitate cooling. A cutaway view of the target vessel is shown further below in Figure 1.3, along with a relative length scale. The section

under consideration, the closest to the incoming pulsed beam, is approximately two feet by four feet in footprint, and six inches thick.

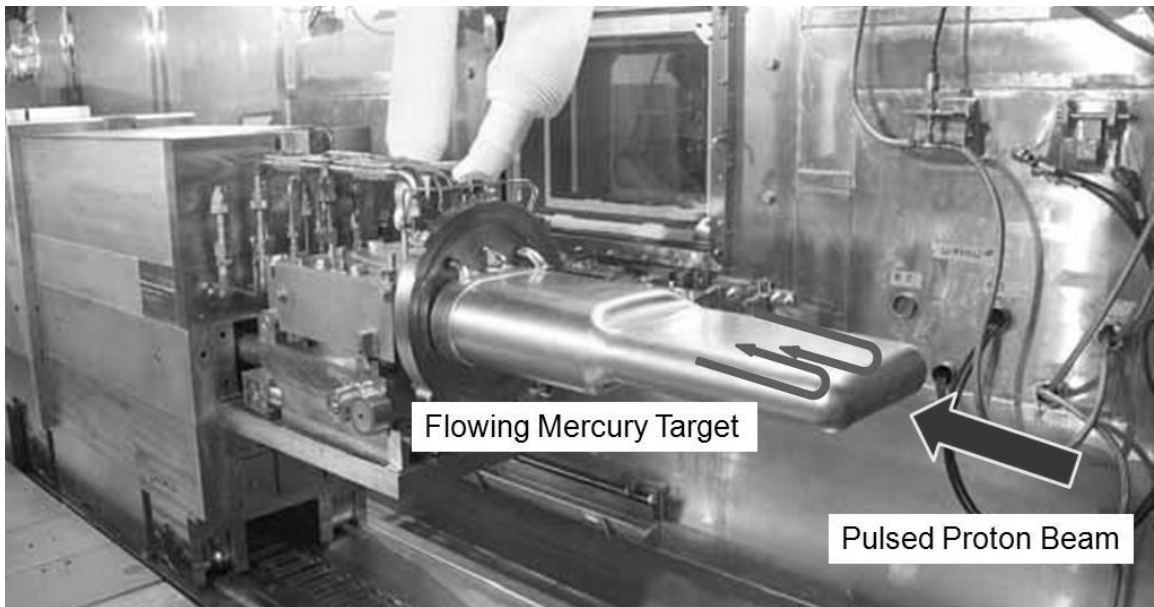


Figure 1.2: The SNS Liquid-mercury-filled Stainless Steel Target Chamber (Courtesy B. Riemer, ORNL SNS)

SNS Target Configuration

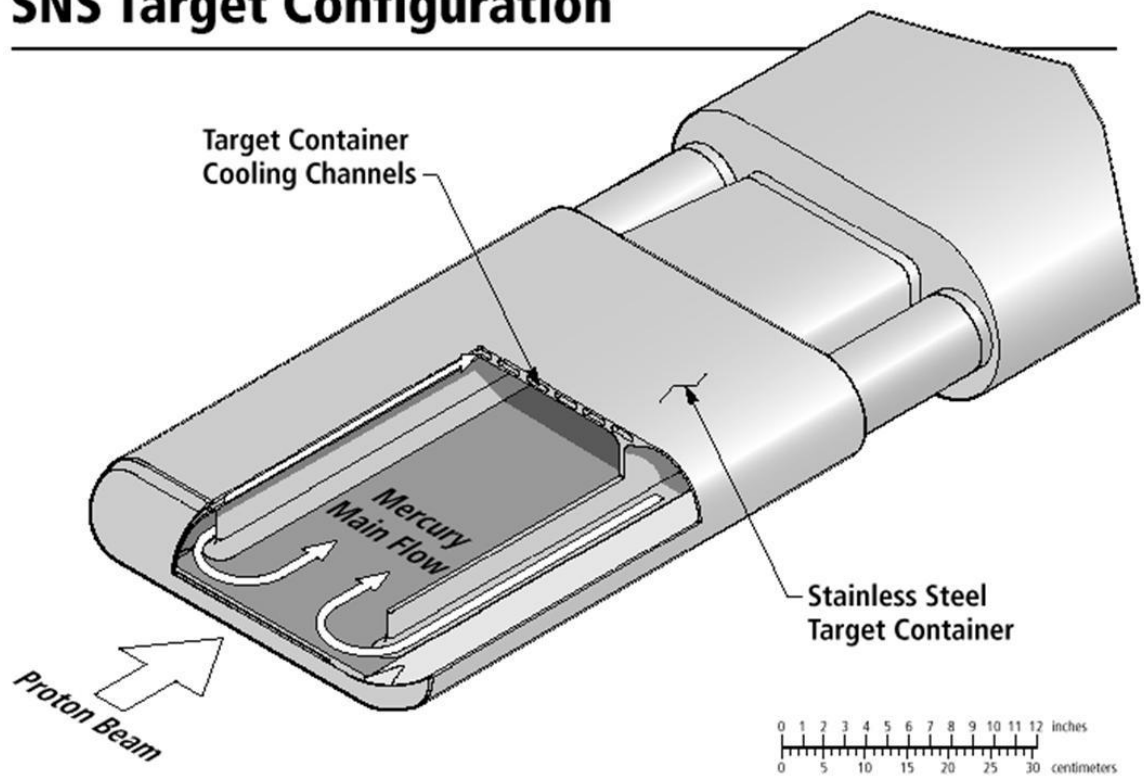


Figure 1.3: A cutaway view of the SNS mercury target, showing flow path, relative size scale, and cooling channels (courtesy B. Riemer, ORNL SNS)

Liquid mercury was chosen for the target for several reasons: (1) it is not damaged by radiation, as are solids; (2) it has a high atomic number, making it a source of numerous neutrons (the average mercury nucleus has 120 neutrons and 80 protons); and (3), because it is liquid at room temperature, it is better able than a solid target to dissipate the large, rapid rise in temperature, it can be flowed for cooling purposes, and it can withstand the shock effects arising from the rapid high-energy pulses.

1.1.2 Cavitation

As mentioned before, there are various benefits to using a flowing liquid metal target for neutron spallation. However, this also presents a hydrodynamic problem. The actual rise in temperature due to energy deposition is only several Kelvin, but the time scale of energy deposition results in rapid isochoric heating at a rate of approximately 14×10^6 K/s. The pressure due to this beam deposition is estimated by

$$\Delta p = \frac{\Delta T \alpha}{\kappa} \approx 40 \text{MPa} , \quad (1.1)$$

where α is the coefficient of volume expansion and κ is the isothermal compressibility. This creates a transient thermal expansion in the mercury and cavities are formed [1]. The large amplitude (~ 40 MPa) and long duration ($500\mu\text{s}$) of the tensile phase of the resultant pressure wave serve to grow vapor nuclei

generated by the proton and neutron collisions to macroscopic size (mm order) vapor cavities. These bubbles then undergo a violent inertial collapse; this mechanism is known as cavitation [2, 3]. The presence of boundaries in the neighborhood of the collapsing bubble can significantly alter the collapse dynamics. In the free field, the collapse is symmetric and will lead to an acoustic emission and possibly a few rebound grow-and-collapse events of decreasing magnitude.

1.1.3 Target Damage Effect

The dynamics of the inertial cavitation collapse discussed above change significantly in the presence of fluid-fluid or fluid-solid boundaries. If a rigid boundary is present (the rigid mercury target vessel walls, for example), the collapse is asymmetric, creating a high-speed liquid jet in the direction of the solid boundary [4, 5]. This can cause significant damage over time. Shown below in Figure 1.4 is an image of a cavitation bubble jetting towards a solid boundary at the instant the liquid jet is impinging on the other side of the bubble boundary.



Figure 1.4: A bubble implodes near a solid surface. The presence of the solid causes the collapse to be asymmetrical, forming a high-speed jet of liquid that impacts the surface. (from L. A. Crum, Ph.D., University of Washington, Applied Physics Laboratory). Bubble diameter approximately 1mm

Multiple-bubble or collective collapse is a phenomenon seen more commonly in real applications than single bubble inertial cavitation, including the case of the SNS. Bubble cloud collapse occurs collectively; as bubbles further from the boundary collapse, they add momentum to the collapsing cloud. Below in Figure 1.5 is a time series of high speed photos showing a bubble cloud collapsing on a rigid target due to a shock wave produced by an electromagnetic lithotripter. Shock waves were continually fired at this target (simulating a kidney stone) at a pulse repetition frequency of 2 Hz. In the first and last snapshot it is clear that fragments of the simulated kidney stone have fractured off from repeated bubble cloud collapses due to the shock waves.

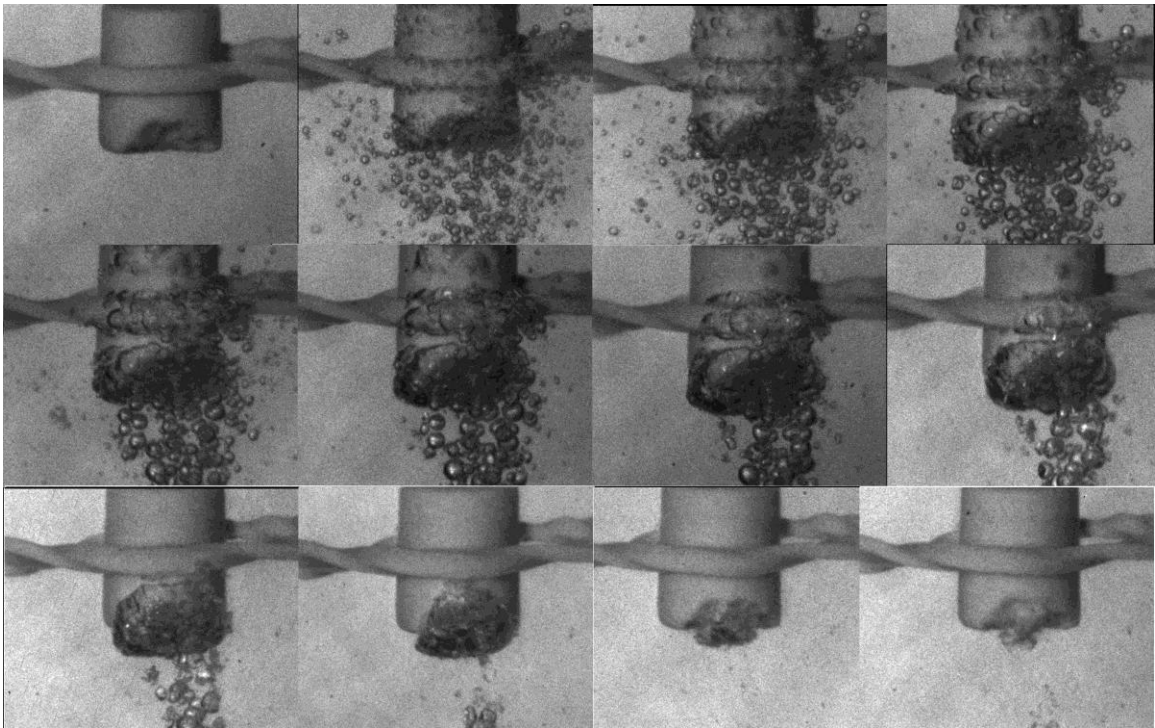


Figure 1.5: High-speed camera photo series of bubble cloud collapse mechanism on a rigid target due to a single shock wave. Shock waves were fired from an electromagnetic Storz SLX lithotripter with the target positioned at the focus. The first frame (top left) was taken 200 microseconds after the lithotripter was triggered, successive photos were taken every 50 microseconds following. Left to right, top to bottom indicate increasing time (Courtesy Jon Kracht and Robin Cleveland)

With regards to the SNS mercury target chamber, cavitation damage erosion is particularly disconcerting due to the disastrous effects one can imagine if the chamber were to rupture. Much work has been done to simulate the potential for cavitation damage in a flowing mercury spallation neutron target [6-10]. The effect of cavitation damage erosion of the mercury target chamber at full beam power has been estimated to yield an unacceptably short estimated target lifetime of about 30 hours or two work weeks [11], two orders of magnitude smaller than the 2500 hour target lifetime constraint from radiation embrittlement [12]. The chance of failure due to cavitation damage erosion within this 2500 hour projected lifetime is projected to be greater than 99.9% [13]. Therefore, there is a strong motivation to significantly extend the lifetime of the target vessel via cavitation damage mitigation.

1.1.4 Possible Cavitation Mitigation Solution

One proposed solution for mitigating the cavitation-induced damage to the SNS mercury target chamber, which may seem counterintuitive, is to introduce a population of small gas bubbles into the mercury flow. When a fluid contains bubbles, the compressibility (κ term in Equation (1.1)) increases significantly, reducing the amplitude of the pressure perturbation associated with the rapid absorption of the proton beam. Also, the shock wave launched due to beam energy deposition will be heavily attenuated as it propagates from the deposition point towards the chamber wall due to the attenuative nature of the bubbly mixture. Both

these established phenomena have been investigated thoroughly through numerical modeling and mock-up experiments in regards to the SNS mercury target chamber conditions specifically [14-23]. These numerical investigations have yielded varying results, depending both on bubble radius and void fraction as well as how the simulation was carried out and by whom. One result indicates that a void fraction of only 10^{-4} and bubble diameter of $100\mu\text{m}$ would decrease the beam deposition pressure by a factor of two [15]. Another result indicated that small bubbles ($100\mu\text{m}$ or less) would provide this same twofold decrease in deposited pressure, but that the void fraction required would be on the order of several tenths of a percent[14]. Another result indicated that a larger bubble radius (order $\sim 1\text{-}2\text{mm}$) would provide better cavitation mitigation because the expansion ratio of larger bubbles from the thermal shock would be decreased and thus jet damage potential of the injected bubbles themselves would decrease [17]. Some more recent numerical models have settled on bubble diameters of less than $100\mu\text{m}$ and void fractions on the order of a few tenths of a percent. Such conditions are predicted to decrease the peak pressure deposited in the mercury by a factor of as much as 100 and decrease the peak pressure seen at the chamber wall by the same amount or more [19]; further simulations also indicated that injected gas choice (helium, argon, etc) could help to decrease cavitation damage potential [23]. The end result of all these simulations has, in general, been that microbubble injection will be effective in

mitigating cavitation damage erosion; void fractions expected to be necessary to probe will be from 10^{-6} to $5 \cdot 10^{-3}$.

As an aside, efforts to create small bubbles in mercury in support of the microbubble injection studies using needles and ports are proceeding concurrent with cavitation mitigation investigations. Due to the poor wettability of mercury on steel and the high surface tension of mercury, creating small bubbles is nontrivial. However, studies have estimated that small bubbles (less than $100\mu\text{m}$) can be created with a narrow needle (inner diameter $100\mu\text{m}$, outer diameter $200\mu\text{m}$) if the linear flow rate of the liquid mercury is sufficiently high (5 m/s); normally the poor wettability causes the escaping gas to form back around the outer surface of the needle and grow until it is sheared off from the needle by the flow [24].

1.1.5 Statement of Posed Problem

Because of the aforementioned wide range of bubbly flow simulations, effective implementation of the microbubble injection approach requires a device/method for *in situ* monitoring of the introduced bubble population both for diagnostic purposes as well as to correlate the effect of different bubble populations to levels of cavitation damage for optimization purposes. Such a device could be implemented in a high-power target test facility, such as the Oak Ridge National Laboratory (ORNL) Target Test Facility (TTF), in order to determine the ideal injected population.

Since mercury is an opaque, corrosive, and toxic liquid metal, measuring the void fraction of a two-phase mercury flow is nontrivial. Certainly a simple optical technique will not be feasible. First we take into consideration various techniques for void fraction determination used in the past.

1.2 Previous Bubbly Flow Characterization Techniques

There are a plethora of previously published techniques for providing diagnostics on bubbly flows. Two-phase flow diagnostics are useful for a wide range of industrial and laboratory applications, from food processing to medical research, from the current interest to ocean science. Measurements of electrical, fluidic, irradiation, optical, acoustic, and other properties have all been investigated. This Section will graze the surface of some of the methods employed in published works in the past and briefly touch on why they are not ideal for the current effort (usually the void fraction range in which they are applicable), and culminate with the method of choice, which will be expanded upon and explained in detail later in this work.

1.2.1 Electrical methods

Several electrical methods can be employed to measure the void fraction of a bubbly mixture.

One method involves measuring the electrical impedance of the bubbly fluid via an electrode bridge; this impedance has a direct relation to the void fraction of the

medium [25]. This method can be employed effectively for high void fractions (>1%) and has been used in this regime very effectively [26-28]. However, the electrical noise threshold (equating to .3% void fraction) and the error dependence on impurities and temperature fluctuations in the liquid make employment of this method in our void fraction range of interest not plausible.

A similar method of measurement uses electrodes to measure the electrical capacitance of the two-phase fluid, this method has similar void fraction range limitations [29].

Another method intended for use with cryogenics uses a radio frequency electromagnetic method and oscillatory circuit whose resonance frequency depends on the void fraction; this method is again applicable for very high (10-100%) void fractions [30].

1.2.2 Fluidic Methods

Void fraction has been measured using the 'side-tube' method, where a main flow is diverted into a smaller side-tube. In this side tube the static pressure head separates the phases and a liquid column height, combined with a differential pressure measurement, yields the void fraction, assuming that the gravitational pressure loss dominates other pressure losses [31, 32]. Experiments showed that these other pressure losses were not necessarily negligible; the system became more accurate as the side tube diameter was increased due to the decrease in frictional loss, but

this also decreases the precision of the column height measurement. Thus again, the range of void fractions over which this technique is usable is higher than that of current interest.

Differential pressure measurements were also used as a concurrent measurement by Silberman [33] and others.

1.2.3 Irradiation Methods

Irradiation methods measuring X-ray absorption [34, 35], γ -ray absorption [36], and neutron scattering [35, 37], and relating those measurements to void fraction, have been employed in past research. The inherent error due to the random nature of radiation is significant and this method is also not effective in our void fraction range of interest.

1.2.4 Optical Methods

Direct optical methods for sizing bubbles, although tedious, have been used in the past. In order to correlate imagery to a volume ratio of gas to liquid, a flow section of known area (or volume) in the optical plane is used, with depth along the optical axis small enough to permit all bubbles to remain in focus (depth of field \geq depth of section) and to disallow 'stacking' of bubbles along the optical axis. Observed 2-dimensional bubble areas (or areas converted to volumes) are then used to calculate an area fraction (or volume fraction) which is equivalent to the void fraction. When void fractions are not so high as to make distinguishing neighboring bubbles

difficult, automated image processing techniques can be used with success. This technique has been experimentally used by the author, Wilson [38], Ruggles et al [39], and Silberman [33] in order to benchmark their acoustical measurements in water/air mixtures. However, using this technique in mercury is not possible.

1.2.5 Acoustic Methods

Lastly, void fraction measurements can be made using acoustic techniques. One characteristic of bubbly flows that is attractive for void fraction measurement is that even the addition of a very small void fraction (say, 10^{-6}) of sufficiently small bubbles will yield a large change in the acoustic properties of the mixture: which properties and how much will depend on the frequency regime of interest and the bubble radius, among others.

One method to exploit this strong dependence on bubble population is to measure acoustic phase velocity using an acoustic resonator. In a simple cylindrical waveguide (other geometries can also be used) driven below the cutoff frequency the resonance modes of the waveguide depend only on the end conditions, the tube length, and the sound speed of the enclosed medium. If a waveguide is driven acoustically in a broadband fashion, the speed of sound propagation in the medium can be easily calculated by fitting the resonance modes to a line. Assuming the frequency regime of interest is well below the resonance frequency of the largest

bubbles, there is a direct relationship between the sound speed of the mixture and the void fraction. Thus, the void fraction can be extracted.

This method has been used extensively in published research, notably in [33] and [39], and is the method of choice for this work.

1.3 Formal Problem Statement

In summary, a diagnostic tool for measuring the void fraction of a two phase flow is required for the investigation of cavitation damage mitigation by microbubble injection in the Oak Ridge National Laboratory (ORNL) Spallation Neutron Source (SNS).

Thus, the goal of this work is as follows: to design, construct, and test a 1-D acoustic waveguide that will allow extraction of void fractions from 10^{-6} to $5 \cdot 10^{-3}$ via standing wave resonance sound speed measurement in both water and mercury host fluids. In order to support this void fraction range, the waveguide must be dimensioned and designed accordingly, since the tube length and diameter will pose restrictions on bubble radius and other characteristics. The waveguide must allow *in situ* sampling of two-phase flow, suggesting a flow-through design. The waveguide apparatus must also be mercury compatible.

The rest of this work will discuss bubbly fluid acoustic theory, materials and methods, results and discussion, and conclusions and suggestions for future work.

Chapter 2

2 Theory

This Chapter is devoted to a theoretical description of the acoustics of bubbly fluids and waveguides as well as a brief presentation of the history of bubbly fluid literature. The combination of these two areas of study provides the theoretical basis for the current work. Various assumptions will be applied to the basic definition of the speed of sound to provide a model for sound propagation in bubbly fluids, which will then be restricted to the low frequency regime in order to further simplify the relationship. Waveguide theory including compensation for the elasticity of the waveguide walls will be presented. Lastly, these two theoretical descriptions will be combined to provide the cumulative theory for the current work.

2.1 Bubbly Fluid Acoustics

The acoustics of bubbly fluids has been a field of high interest to scholars, researchers, and industry for the past century. Initial investigations came about due to mere curiosity of everyday phenomena. In what is usually considered the first published research into the physics behind bubbly fluid acoustics, Arnulph Mallock wrote in 1910 about the curious feature of a glass of ‘frothy liquid’ to exhibit a dull thud when struck; attributing this to the damping effect of the gas bubbles, he went on to investigate the velocity of propagation and energy damping in such a fluid analytically [40]. In 1917, Lord Rayleigh was motivated by the collapse of steam bubbles in a boiling kettle and went on to write about the pressure developed in a cavitation bubble [2]. In 1930, A. B. Wood expanded on the work of Mallock and used a thermodynamic approach to discuss the acoustic properties of a bubbly mixture [41]. In 1933, Minnaert considered the sounds of running water and went on to define the concept of bubble resonance frequency. [42]. For the next 75 years the field of bubbly fluid acoustics became heavily researched both for scholarly interest as well as applications in industry and science.

2.1.1 Bubbly Fluid Sound Speed Derivation

This section will use a basis from Wood and Mallock (and Carey [43]) to present a brief discussion of sound propagation in bubbly fluids. The basic definition of the speed of sound in a compressible fluid medium can be expressed as

$$c^2 \equiv dP / d\rho, \quad (2.1)$$

where c is the speed of sound in the medium, P is the pressure, and ρ is the density of the medium. Since the compressibility of the medium can be expressed as the inverse of the density, and the medium of interest could be a uniform mixture of various media (in this case the interest is in a bubbly liquid mixture), the speed of sound can now be expressed as

$$c_m^2 \equiv dP_m / d\rho_m = (\rho_m \kappa_m)^{-1}, \quad (2.2)$$

where c_m is the speed of sound in the mixture, ρ_m is the mixture density, and κ_m is the compressibility of the medium (or the effective compressibility of the mixture). Since this result implies that a bubbly liquid mixture acts as a spring-mass-damper system, we can apply such theory to it. In [42], Minnaert defined the resonance frequency of a gas bubble entrained within a liquid, which, slightly modified, can be expressed as

$$f_0 = \frac{1}{2\pi R_0} \sqrt{\frac{3\nu P_0}{\rho_0}}, \quad (2.3)$$

where f_0 is the resonance frequency, R_0 is the bubble equilibrium radius, ν is the polytropic index of the gas¹, P_0 is the ambient pressure, and ρ_0 is the density of the

¹ The 'Minnaert' resonance frequency assumes lossless and adiabatic behavior, and as such the polytropic index he published was taken to be the ratio of specific heats of the gas (for example, 1.4

liquid. For example, an air bubble of radius 1mm in water has a resonance frequency of approximately 3.3 kHz. It should be noted that the Minnaert resonance frequency does not account for the surface tension of the bubble, which has the effect of increasing the ambient pressure P_0 by the Laplace pressure $2\sigma / R_0$, where σ is the surface tension specific to interaction between the fluid and gas of interest. In the case of water and air, this term is oft ignored unless the Laplace pressure is on the order of an atmosphere. Since this occurs for bubbles of about 1 micron radius and smaller, which are an order of magnitude smaller than the smallest bubbles expected to be made for this work, the surface tension will be neglected; the resonance frequency equals the Minnaert frequency. For mercury, the surface tension effect may need to be investigated.

Next we introduce a quantity representing the volume ratio of gas to that of the total gas and liquid mixture; this is called the void fraction and is denoted

$$\beta = V_g / V_m = V_g / (V_g + V_l), \quad (2.4)$$

where V_g , V_l , and V_m are the volumes of the gas, liquid, and total mixture, respectively. The effective density and compressibility of a mixture of gas bubbles in a liquid can thus be described as follows:

for air), denoted as γ . In Equation (2.3) the author has intentionally left the polytropic index symbolized as ν , since it is dependent on both frequency and bubble size. In the isothermal case (low frequency), the polytropic index can often be taken as 1.

$$\rho_m = (1 - \beta)\rho_l + \beta\rho_g \quad (2.5)$$

$$\kappa_m = (1 - \beta)\kappa_l + \beta\kappa_{bub} \quad (2.6)$$

where ρ_l and ρ_g are the respective densities of the liquid and gas, κ_l is the compressibility of the liquid, and κ_{bub} is the compressibility due to the bubbles. It is important to note that this is not the same as the compressibility of the gas phase, owing to the dynamic character of acoustically driven bubble pulsations. In particular, bubbles driven near their resonance frequency will appear more compressible due to the large volumetric excursions. Inserting Equations (2.5) and (2.6) into Equation (2.2) yields

$$\frac{1}{c_m^2} = [(1 - \beta)\rho_l + \beta\rho_g][(1 - \beta)\kappa_l + \beta\kappa_{bub}] \quad (2.7)$$

The compressibility due to the bubbles is a frequency dependent parameter that must be derived from a consideration of bubble dynamics.

2.1.2 Sound Propagation Including Bubble Dynamics

As mentioned previously, a bubbly mixture can be to an extent modeled as a spring-mass-damper system. Using this simple harmonic analysis and assuming that pressure perturbations are small and of the form $P(t) = P_0 + p(t)$, we can further expand Equation (2.7) to be applicable at all frequencies. Extensive work has been published in the literature on how to model propagation through bubbly liquids in

various frequency regimes when bubble dynamics are considered. This requires in-depth derivation of the conservation equations and equations of state as well as direct derivation of the bubble dynamics, both nontrivial endeavors. Some examples of how the former have been attempted can be seen in Caflisch *et al* [44] and van Wijngaarden [45], examples of the latter in Prosperetti *et al* [46] and Keller and Miksis [47]. Early works by Foldy [48] and Carstensen and Foldy [49] determined the frequency dependence of bubble damping by using a multiple scattering approach. Other methods provided similar results.

In 1989, Commander and Prosperetti [50] compiled these and other predecessors' works to derive a detailed model for sound propagation in a bubbly liquid that included a detailed energy dissipation analysis for an effective medium, resulting in a frequency dependent bubble damping term with multiple components. Their efforts are often used as the benchmark for studies on bubbly fluid acoustics, and will be used here for the discussion of wave propagation with bubble dynamics considered.

For a monodisperse bubbly medium², the frequency-dependent sound speed is given by

$$\frac{1}{c_m^2} = \frac{1}{c_l^2} + \frac{4\pi\bar{a}n}{\omega_0^2 - \omega^2 + 2jb\omega}, \quad (2.8)$$

² The details of this approximation and its application in real situations will be discussed in the next section detailing low frequency sound propagation.

where \bar{a} is the equilibrium bubble radius and n is the number of bubbles per unit volume (these can be related to the void fraction), j is the square root of negative one, ω_0 is the resonance frequency (which is not necessarily the Minnaert frequency), ω is the frequency of driving, and b is the bubble damping coefficient. The damping coefficient b is given by

$$b = \frac{2\mu}{\rho_l a^2} + \frac{P_e}{2\rho_l a^2 \omega} \text{Im}\Phi + \frac{\omega^2 a}{2c_l}, \quad (2.9)$$

where the three terms account for the viscous, thermal, and acoustic energy dissipation effects, respectively, and Φ is

$$\Phi = \frac{3\nu}{1 - 3(\nu - 1)jX[(j/X)^{1/2} \coth(j/X)^{1/2} - 1]}, \quad (2.10)$$

with the X term defined as

$$X = \frac{D_g}{\omega a^2}, \quad (2.11)$$

where D_g is the thermal diffusivity of the gas. P_e is the equilibrium pressure in the bubble and is given by

$$P_e = P_0 + \frac{2\sigma}{a}. \quad (2.12)$$

In this case, the resonance frequency will include the surface tension term and is give by the expression

$$\omega_0^2 = \frac{P_e}{\rho_l a^2} \left(\text{Re} \Phi - \frac{2\sigma}{aP_e} \right). \quad (2.13)$$

Finally, Equation (2.8) can be understood in a perhaps more useful manner if it is described in terms of phase speed and attenuation. If the term c_l/c_m is broken up into its real (phase speed) and imaginary (lossy, *i.e.* attenuative) components $u - jv$, then the phase speed V is given by

$$V = c_l / u, \quad (2.14)$$

and the attenuation coefficient in dB per unit length is expressed as

$$A = 20(\log_{10} e) \left(\frac{\omega v}{c_l} \right). \quad (2.15)$$

Below in Figure 2.1 and Figure 2.2 are shown the phase speed and attenuation plots versus frequency for a monodisperse bubbly mixture of water and air with 1mm radius bubbles and a void fraction of 1E-3.

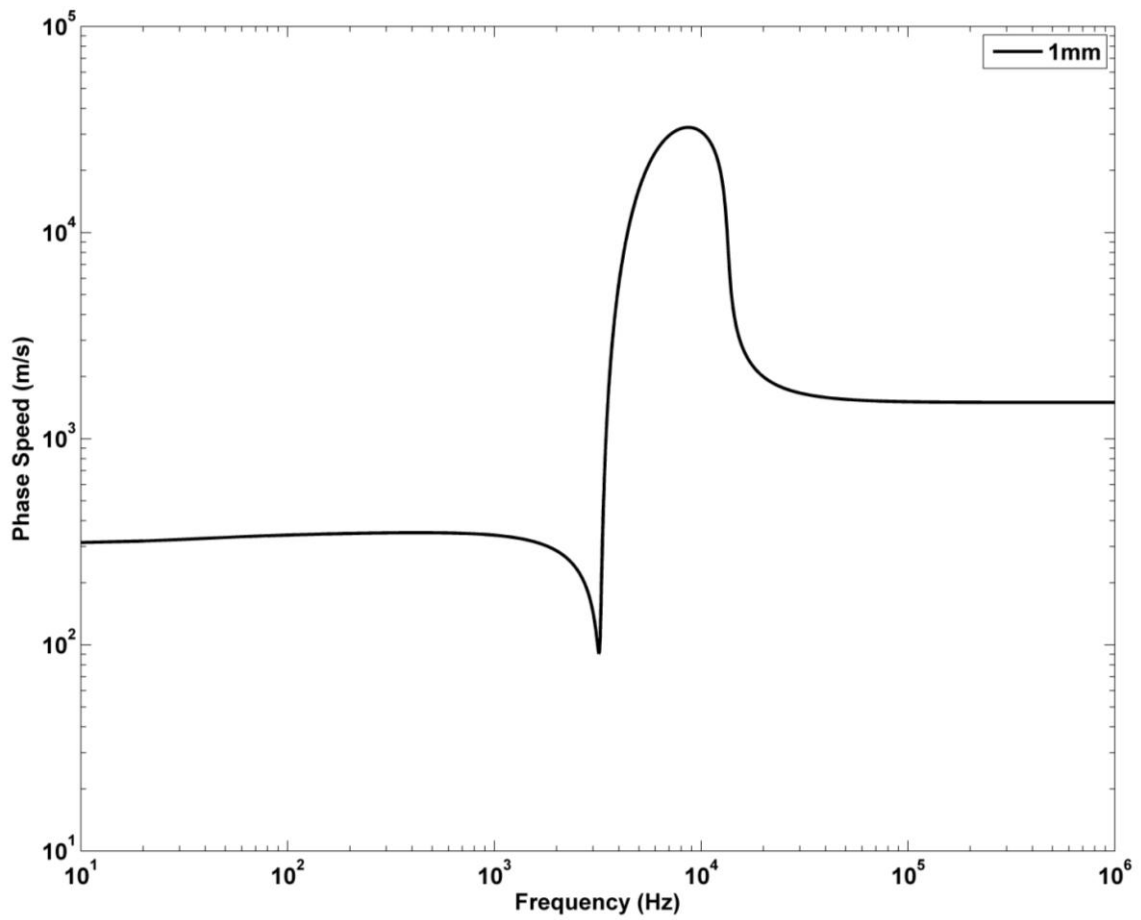


Figure 2.1: Phase speed versus frequency for a monodisperse bubbly mixture of water and air with bubble radius 1mm and void fraction $1E-3$ from Equation (2.14)

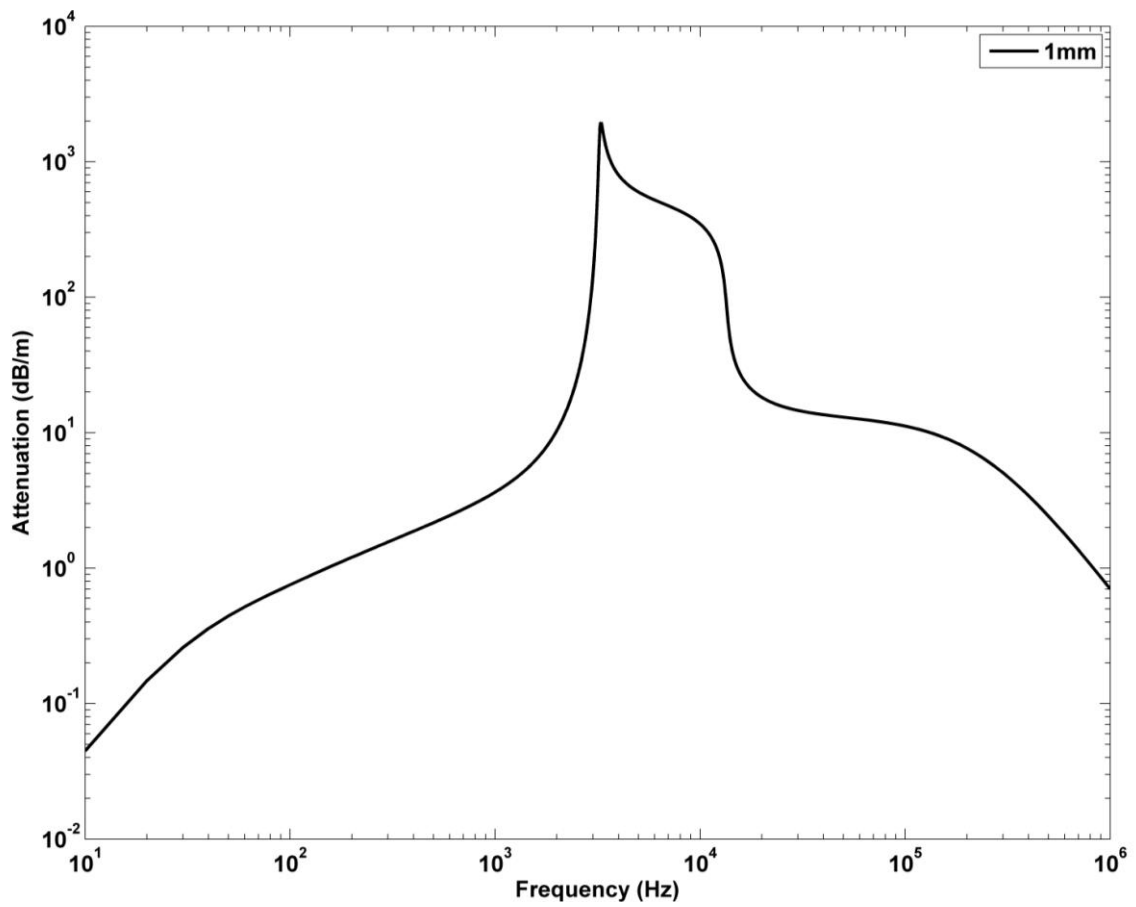


Figure 2.2: Attenuation versus frequency for a monodisperse bubbly mixture of water and air with bubble radius of 1mm and void fraction $1E-3$ from Equation (2.15)

At frequencies well below the resonance frequency, it is clear that the attenuation is low and the phase speed is non-dispersive. This flat region is referred to as the Wood limit, after A. B. Wood [41], and can be clearly seen in Equation (2.8) by setting ω equal to zero, and the resulting mixture sound speed becomes the liquid sound speed less a correction factor that is dependent on the void fraction. As the resonance frequency is approached, the phase speed begins to drop and the attenuation rises abruptly. This is approaching the region of the most dispersion. At the resonance frequency the attenuation is a maximum and the phase speed is a minimum. Through resonance the phase speed increases sharply in an asymptotic manner, such that just above resonance the phase speed is supersonic with respect to the pure liquid. The attenuation is reduced with respect to the resonance frequency, but is still far higher than throughout the sub-resonance regime. The supersonic region continues after resonance as attenuation lessens, and the phase speed peaks at some frequency larger than the resonance frequency. Throughout these small regions surrounding the resonance frequency, the dominant term is the second term of Equation (2.8), since the $\omega_0^2 - \omega^2$ denominator term is small and either positive or negative and thus the whole term is large. The phase speed now begins to fall asymptotically towards the sound speed of the pure liquid after the supersonic regime, while attenuation continues to decrease. This is evidenced in Equation (2.8) by inserting an ω of infinity, and the result is that c_m becomes c_l .

Figure 2.1 and Figure 2.2 show the general behavior of the phase speed and attenuation for a bubbly fluid; the extent and span of the features of these curves can vary with bubble radius and void fraction. The effects of changing void fraction or bubble radius can be examined by fixing one and varying the other. Below in Figure 2.3 and Figure 2.4 are shown the phase speed and attenuation versus frequency curves for void fractions of $1E-3$, $1E-4$, and $1E-5$, for air bubbles of radius 1mm in water. Further below in Figure 2.5 and Figure 2.6 are shown the phase speed and attenuation versus frequency curves for 0.1mm, 1mm, and 5mm air bubbles in water for a void fraction of $1E-3$.

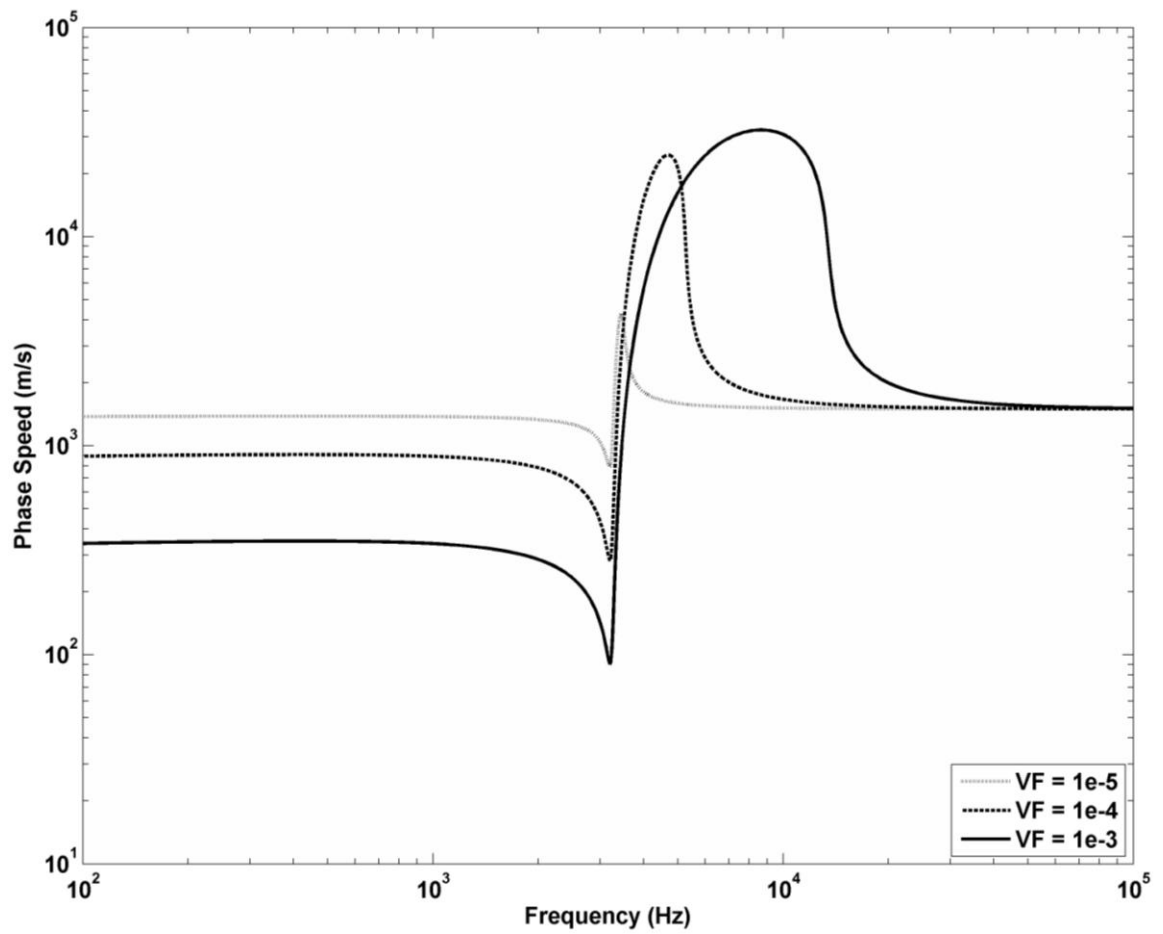


Figure 2.3: Phase speed versus frequency for three monodisperse bubbly mixtures of water and air with bubble radius 1mm and void fractions of 1E-5 (gray dotted line), 1E-4 (dashed line), and 1E-3 (solid line) from Equation (2.14)

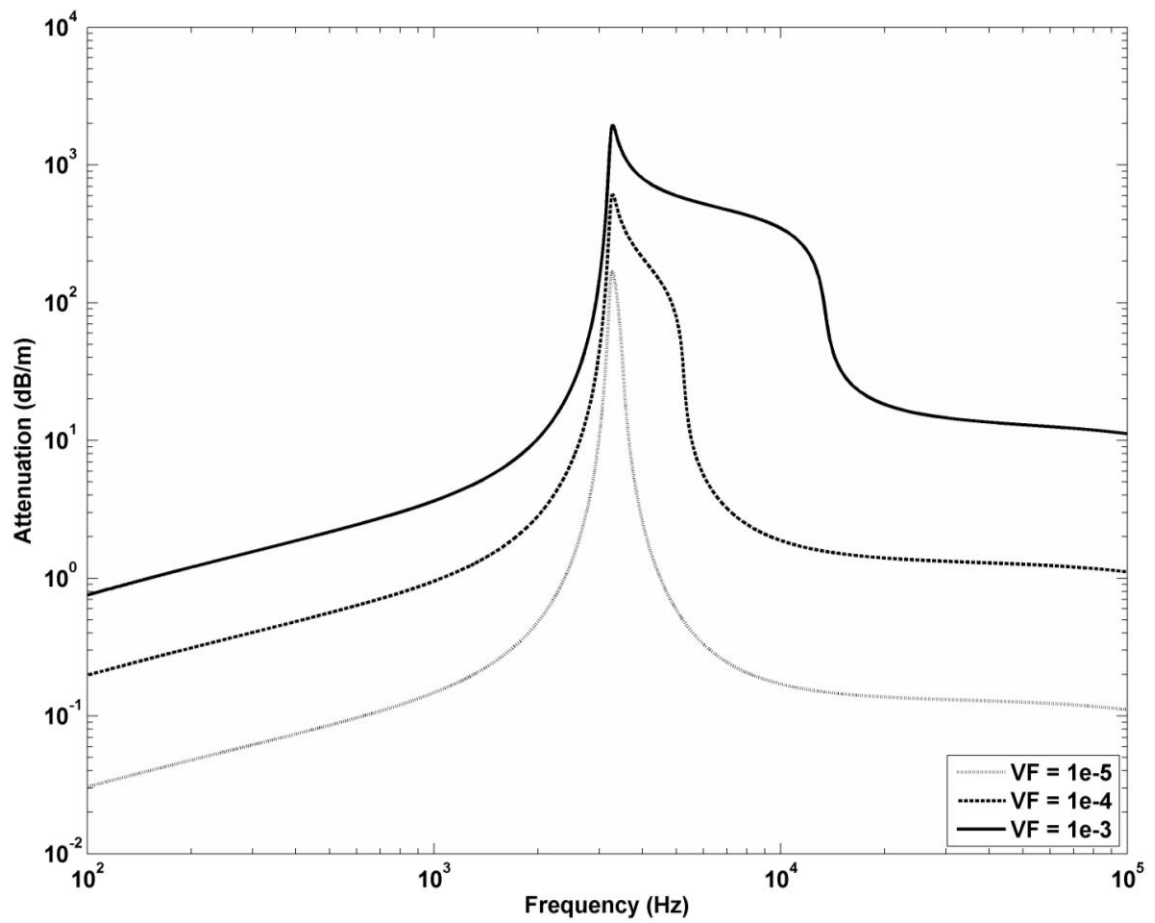


Figure 2.4: Attenuation versus frequency for three monodisperse bubbly mixtures of water and air with bubble radius 1mm and void fractions of $1E-5$ (gray dotted line), $1E-4$ (dashed line), and $1E-3$ (solid line) from Equation (2.15)

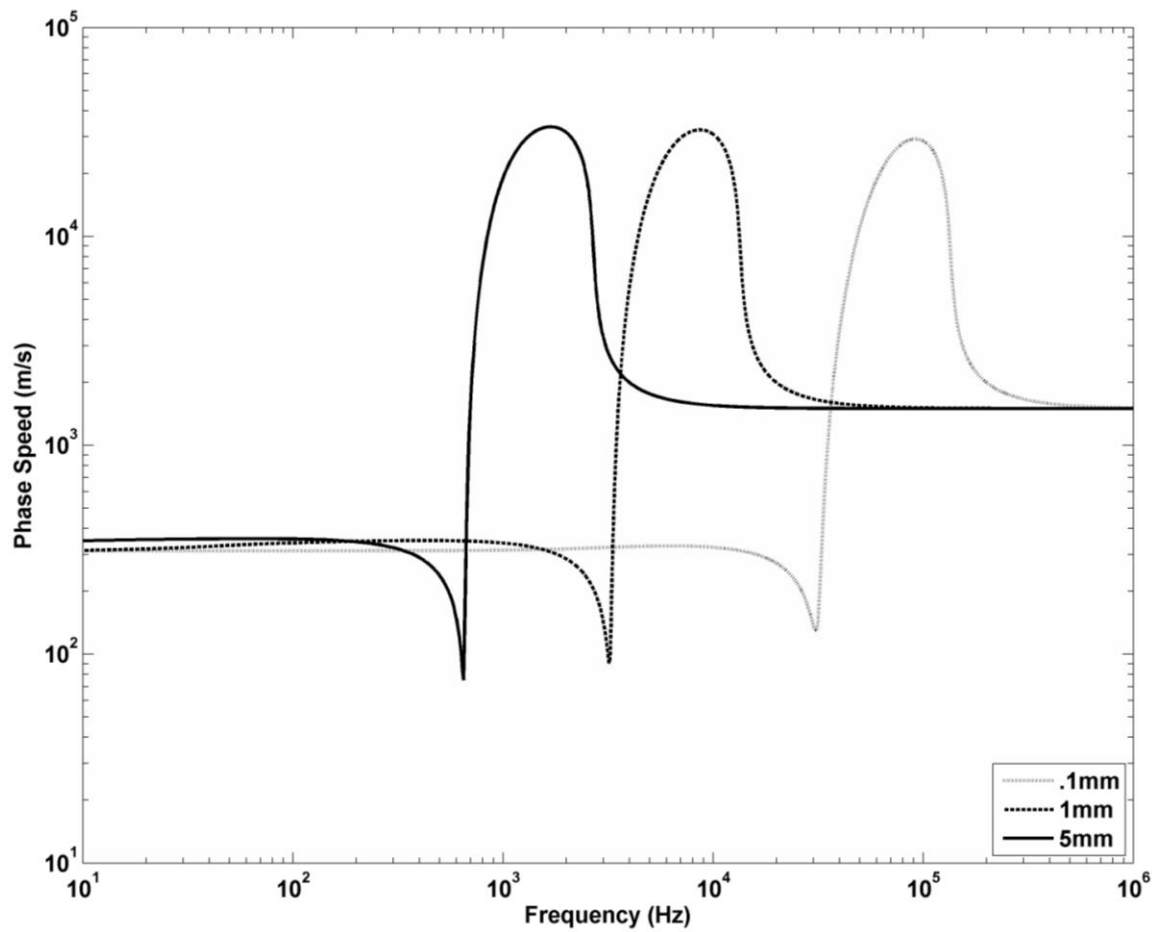


Figure 2.5: Phase speed versus frequency for three monodisperse bubbly mixtures of water and air with void fraction 10^{-3} and bubble radii of 0.1mm (gray dotted line), 1mm (dashed line), and 5mm (solid line) from Equation (2.14)

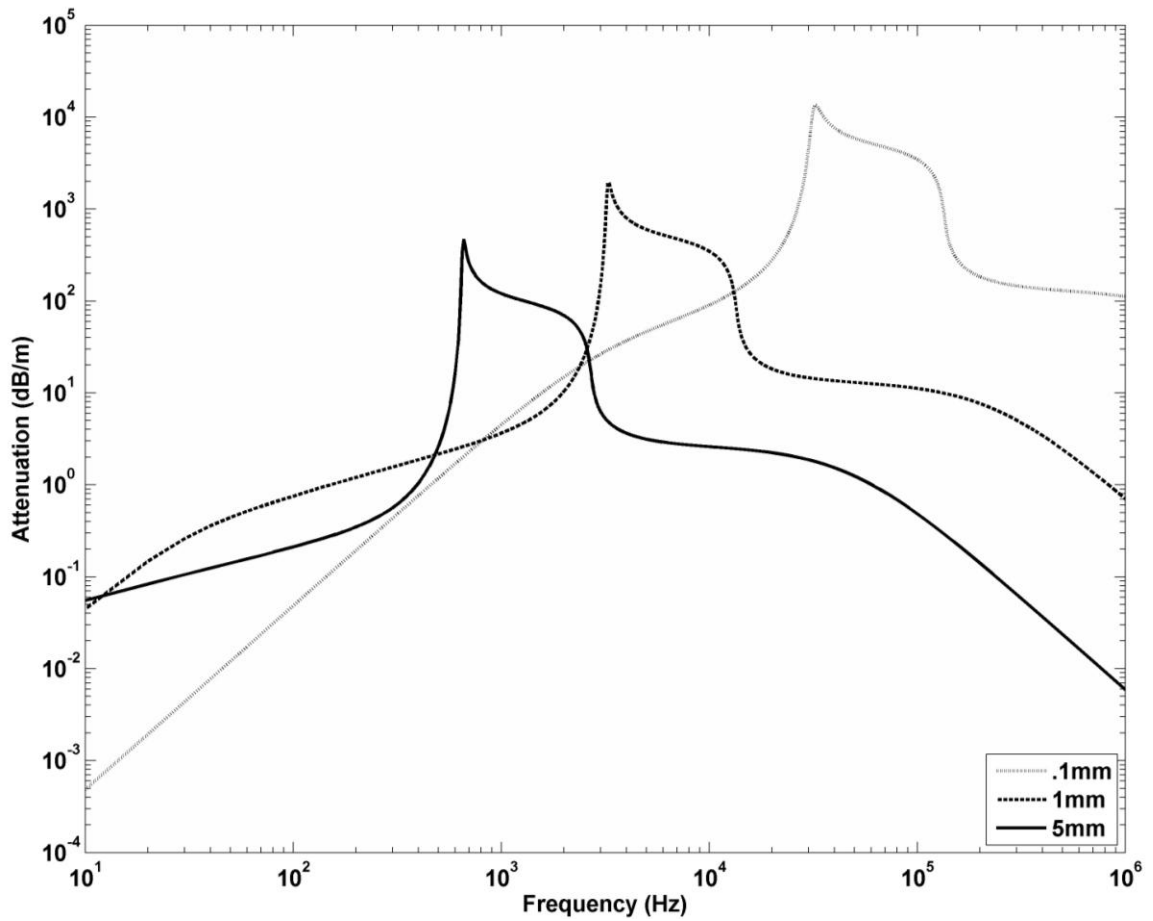


Figure 2.6: Attenuation versus frequency for three monodisperse bubbly mixtures of water and air with void fraction $1E-3$ and bubble radii of 0.1mm (gray dotted line), 1mm (dashed line), and 5mm (solid line) from Equation (2.15)

In Figure 2.3 and Figure 2.4, the effect of changing the void fraction is demonstrated. It can be seen that for a given bubble radius, in short, everything becomes more pronounced as void fraction increases. The Wood limit shortens, as can be seen in the phase speed graph, where the frequency at which the flat region begins to curve downwards is lower. The Wood limit sound speed is lower as void fraction increases, as is expected. The minimum phase speed is lower as void fraction increases, and thus the peak attenuation is larger. The maximum phase speed is greater, and the width of this supersonic region also increases with void fraction on the phase speed plot, while on the attenuation plot the bandwidth of the attenuation peak is also larger. All of these effects are clearly indicated in Equation (2.8), where the void fraction is a scaling factor on the second term, and as void fraction increases the $\omega_0^2 - \omega^2$ portion of the denominator can also cause the this term to change rapidly. Thus, one can qualitatively view the void fraction as a scaling factor of the second term that determines the Q and bandwidth of the region across which resonance effects dominate. Mixtures of all void fractions will asymptote to the sound speed of the bubble-free host liquid as the frequency goes to infinity.

In Figure 2.5 and Figure 2.6, the effect of changing the bubble radius is shown. Again the second term of Equation (2.8) and its relation to the first term is what determines the shape of the phase speed and attenuation plots. However, in this case the bubbles radius is being changed, so there is a decrease in the resonance frequency. Furthermore, the entire second term is scaled by bubble radius, and the

damping term is dependent on the radius. The resonance frequency shifts the resonance region left or right on the frequency axis. As bubble radius increases, the region approaching resonance exhibits a sharper attenuation increase and phase speed decrease. The minimum phase speed is lower for larger bubbles. Just past resonance, the maximum attenuation is smaller and the maximum phase speed is larger for larger bubbles. As bubble radius increases, the region following resonance exhibits a sharper attenuation decrease, and the supersonic region has an increased Q and decreased bandwidth in both the phase speed and attenuation plots.

2.1.3 Low Frequency Sound Propagation

For frequencies well below bubble resonance (refer to the flat regions of no dispersion in the phase speed vs. frequency plots in Figure 2.1, Figure 2.3, and Figure 2.5), bubbles are able to dissipate heat rapidly to the surrounding fluid and thus bubble pulsations are approximately isothermal, as shown by Hsieh and Plesset [51]. Therefore the compressibility due to the bubbles, κ_{bub} , simply becomes the isothermal compressibility of the gas, κ_g . Thus, Equation (2.7) becomes

$$\frac{1}{c_m^2} = [(1 - \beta)\rho_l + \beta\rho_g][(1 - \beta)\kappa_l + \beta\kappa_g], \quad (2.16)$$

which is a form of Wood's well-known equation for low frequency sound propagation in a bubbly mixture [41]. This can be expanded as

$$\frac{1}{c_{m\ell}^2} = \frac{(1-\beta)^2}{c_l^2} + \frac{\beta^2}{c_g^2} + \beta(1-\beta) \frac{\rho_g^2 c_g^2 + \rho_l^2 c_l^2}{\rho_l \rho_g c_l^2 c_g^2}, \quad (2.17)$$

where $c_{m\ell}$ is the mixture sound speed at low frequencies, c_l is the speed of sound in the liquid, and c_g is the isothermal sound speed in the gas. Equation (2.17) is also equivalent to the expression

$$\frac{1}{c_m^2} = \frac{(1-\beta^2)}{c_l^2} + \frac{\beta^2}{c_g^2} + \frac{\beta(1-\beta)\rho_l}{\nu P_0}. \quad (2.18)$$

Notice that this expression is independent of bubble radius; the only restriction is that the frequency range of interest is significantly below the bubble resonance frequency. Experimental investigations have shown that working at half the resonance frequency and below provides excellent results [33]. It is typically stated that Equation (2.18) describes low frequency sound propagation in a monodisperse bubbly medium. However, true monodispersity is often not present in real applications; narrow distributions centered around a mean bubble radius are common. The practical restriction of the Wood limit is that the resonance frequency of the largest bubbles be greater than the highest frequencies of interest. Since the largest bubbles satisfy this criterion and the resonance frequency increases with decreasing bubble radius, then the population as a whole satisfies the low frequency criterion. Although measurement of frequency-dependent sound speed and attenuation can be extremely difficult for bubble distributions, in the low-frequency

Wood limit the phase speed is dependent solely on the void fraction and independent of the details of the bubble size distribution.

If the Wood limit (sufficiently sub-resonance limit) is applied to Equation (2.18), assuming the polytropic index can be taken as unity, and assuming that the void fraction is very low, such that $\beta \ll 1$, $(1 - \beta)^2 \approx 1$, and $\beta^2 \approx 0$, one will notice that this is identical to the approximation given by Equation (2.8) when the effect of bubble dynamics is removed. Equation (2.18) is plotted below in a sound speed versus void fraction semi-log plot for water-air and mercury-helium mixtures in Figure 2.7. The material values used in all theory calculations are shown in the next chapter in Table 3.1.

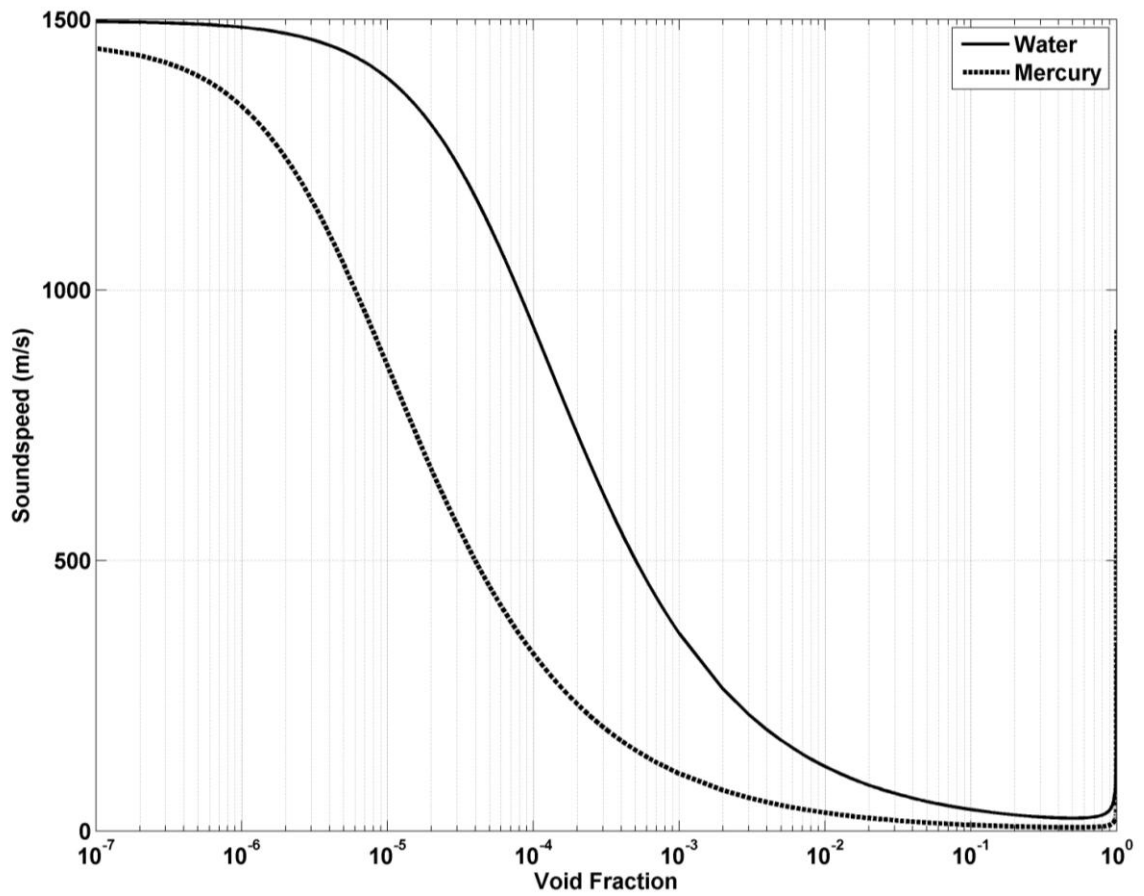


Figure 2.7: Relationship between sound speed and void fraction for air bubbles in water at STP (solid line) and helium bubbles in mercury (dashed line) from Equation (2.18)

The validity of Wood's low frequency approximation has been evaluated experimentally in the literature, notably by E. Silberman in 1957 [33]. Silberman used a standing wave technique in a stainless steel tube driven by a loudspeaker and injected bubbles via an array of needles. As the tube was driven, a hydrophone was scanned vertically to pinpoint the location of two adjacent pressure nodes; the distance between the two nodes gives half the wavelength, from which can be calculated the phase speed. Also, the difference in acoustic pressure provided values for the attenuation. Acceptable agreement with Wood's equation was found. Similar experiments investigating sound propagation in the Wood limit have been published by many, including Ruggles *et al.* [39], van Wijngaarden [52], and Gibson [53]. In what is likely the best published data in this regime, Cheyne, Stebbings, and Roy were able to find excellent agreement with theory in making phase speed measurements via a fiber optic laser interferometry method [54].

2.2 Waveguide Acoustics

The other portion of theory pertinent to this work is that of waveguide acoustics. Using an enclosure to guide the propagation of sound is a fundamentally efficient way to reduce losses; furthermore, creating standing wave resonances can help to increase signal to noise ratio in experiments. Herein will be discussed general ideal waveguide theory, limitations of the assumptions made in idealizing a waveguide model, including a plane wave assumption, and how to account for real effects such

as the elasticity of wall materials, arbitrary impedance end conditions, and non-negligible acoustic impedance of the host medium.

2.2.1 Standing Plane Wave Propagation in a Rigid-wall Tube

Standing wave modes in several configurations of a rigid tube will be considered here. There are benefits to using different tube, driving, boundary, and end conditions, depending on the intended application, media, and other factors. The theory pertaining to a few common configurations will be presented in this Section. This is a well-trodden ground in both the acoustics and electromagnetics literature. The discussion below is based on the treatment given in [55].

Let us consider the waveguide to be a 1-dimensional region for the propagation of plane wave acoustics. In the previous Section we applied various assumptions to our model for the propagation of sound in a bubbly fluid; one of these assumptions was a low frequency approximation. Because of this, we can also apply that approximation to our discussion of waveguides, and in fact even force waveguide design to apply only in the low frequency regime. To this end, if we consider 3-dimensional cylindrical coordinates, the cutoff frequency of a given mode of a tube is given by

$$f_{mn}^c = \frac{\alpha'_{mn} c_0}{2\pi b}, \quad (2.19)$$

where m and n are the axial and radial indices, respectively, b is the radius of the waveguide, and α'_{mn} is the zero of the first derivative of the Bessel function of the first kind ($J'_m(x)$). If we only consider the lowest value of α'_{mn} that is non-zero (the zero value is for the axisymmetric pure plane wave mode), this yields the frequency below which no non-plane wave acoustics can physically exist,

$$f_{11}^c = \frac{\alpha'_{11}c_0}{2\pi b} = \frac{1.841c_0}{2\pi b}. \quad (2.20)$$

Therefore, as long as the frequency of interest is below the cutoff frequency for non-plane wave modes in the waveguide under consideration, we need only consider the linear 1-dimensional plane wave case.

If one linearizes the continuity equation, momentum equation, and isentropic equation of state via the small signal approximation, the three resulting equations can be combined to provide the one-dimensional wave equation for acoustic pressure in a medium of sound speed c ,

$$\frac{\partial^2 p}{\partial x^2} - \frac{1}{c^2} \frac{\partial^2 p}{\partial t^2} = 0. \quad (2.21)$$

If instead the pressure is eliminated when combining the constitutive equations, the form is the same but p is replaced with u . For a tube of length l , the solution to Equation (2.21) is

$$p(x,t) = [A \cos[k(l-x)] + B \sin[k(l-x)]] e^{j\omega t}, \quad (2.22)$$

where the parenthetical term represents the spatial dependence and the complex exponential represents the harmonic time dependence; k is the wave number ω/c . The coefficients A and B will be dependent on the boundary conditions. Note that complex exponentials and trigonometric functions are essentially interchangeable in acoustics via Euler's formula; the choice of which to use is dependent on the application. In general, trigonometric functions are more useful for cases of standing waves, initial value problems, or interior domains like a cylindrical cavity; complex exponentials are more useful for cases of progressive waves, forcing function problems, or exterior domains like a radiation problem. The particle velocity is related to the pressure by the linearized momentum equation,

$$\rho_0 \frac{\partial u}{\partial t} + \frac{\partial p}{\partial x} = 0. \quad (2.23)$$

Thus, the particle velocity is given by

$$u(x,t) = -\frac{1}{\rho} \int \frac{\partial p}{\partial x} dt. \quad (2.24)$$

Combining Equation (2.22) and Equation (2.24) yields the particle velocity,

$$u(x,t) = -\frac{1}{j\rho c} [A \sin[k(l-x)] - B \cos[k(l-x)]] e^{j\omega t}. \quad (2.25)$$

Further meaningful simplification requires knowledge of boundary conditions. Several scenarios will be considered.

2.2.2 Resonances of a Driven Tube

A common configuration uses a source at one end of a waveguide to provide the driving acoustics. We will assume that these sources provide time-harmonic excitation; this is a reasonable assumption for linear acoustics. The treatment presented below derives from Chapter 4 of the textbook by Blackstock [55].

Let us first assume that at $x = 0$ we have a vibrating piston (thus it is a pure velocity source) which prescribes a particle velocity to the waveguide of the form

$$u(0, t) = u_0 e^{j\omega t}, \quad (2.26)$$

where u_0 is some fixed peak value of the particle velocity. Let the other end of the waveguide be open to the air, such that the acoustic impedance mismatch between the enclosed fluid and the air is very high. Thus the reflection coefficient,

$$R = \frac{Z_{air} - Z_{fluid}}{Z_{air} + Z_{fluid}}, \quad (2.27)$$

is approximately -1. Thus the pressure must go to zero at the tube end. Applying $p(l, t) = 0$ to Equation (2.22) results in the coefficient A being zero. Therefore,

$$u(x, t) = \frac{1}{j\rho c} B \cos[k(l - x)] e^{j\omega t} \quad (2.28)$$

and we can now apply the prescribed source condition of Equation (2.26) to Equation (2.28) and solve for the coefficient B , which is

$$B = \frac{ju_0\rho c}{\cos(kl)}. \quad (2.29)$$

Finally, the pressure and particle velocity are now described by the following two expressions:

$$p(x,t) = ju_0\rho c \frac{\sin[k(l-x)]}{\cos(kl)} e^{j\omega t} \quad (2.30)$$

$$u(x,t) = u_0 \frac{\cos[k(l-x)]}{\cos(kl)} e^{j\omega t} \quad (2.31)$$

The impedance as a function of position is given by $Z = p / u$, or

$$Z(x) = j\rho c \tan[k(l-x)]. \quad (2.32)$$

The resonance frequencies of a waveguide occur when the acoustic pressure becomes unbounded. Examining Equation (2.30) reveals that the pressure becomes unbounded when the denominator, $\cos(kl)$, is zero. Thus the modal frequencies are given by odd integer multiples of quarter-wavelengths,

$$f_n = \frac{c}{2l} \left(n + \frac{1}{2}\right), n = 0, 1, 2, 3, \dots, \quad (2.33)$$

for a tube driven by a vibrating piston at one end and with a pressure release condition at the other end. Below in Figure 2.8 is shown an experimental result that depicts the modes given by Equation (2.33). The result is from a 69cm-long long stainless steel tube with a 2.5cm radius and 2.5cm wall thickness. It was driven by a piston source at the bottom and open to the air at the top; the tube was driven with Gaussian noise (broadband excitation) and a hydrophone was used to obtain the frequency response at points along the tube length in 5cm increments. The waterfall plot maps out the acoustic pressure distribution in the tube as a function of both frequency and position; the mode shapes of $\lambda/4, 3\lambda/4, 5\lambda/4, \dots$ are clearly visible in the figure.

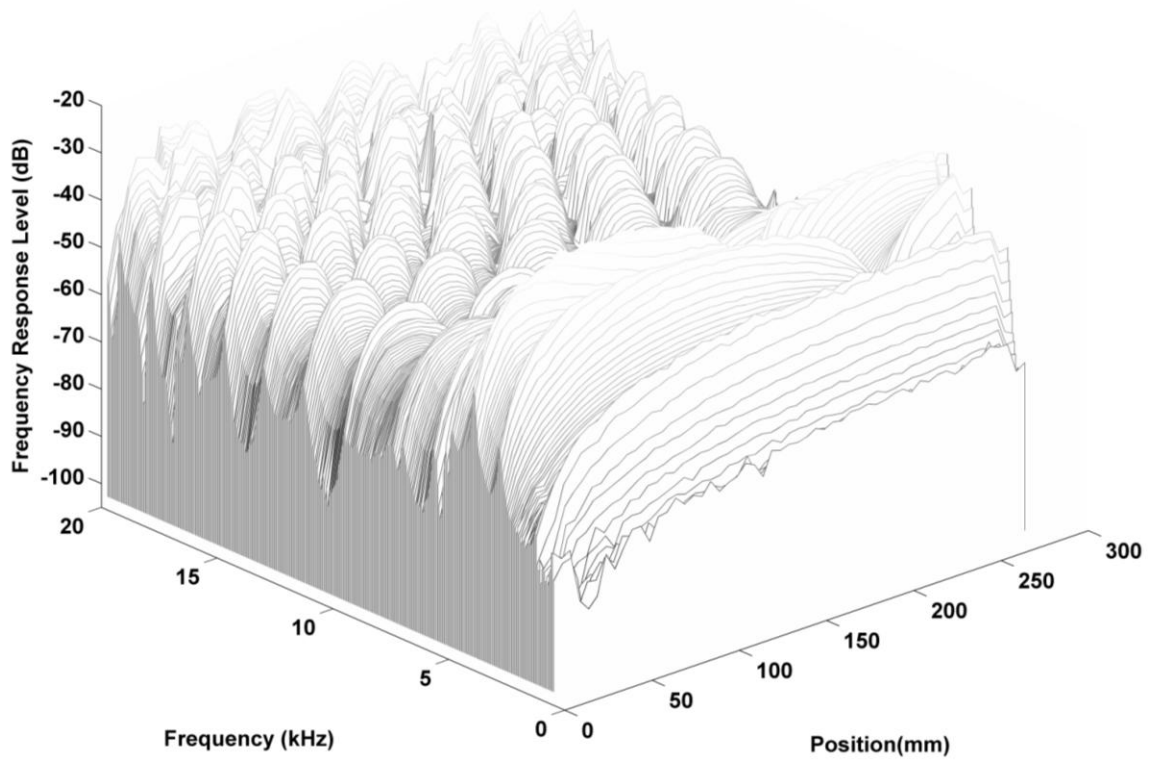


Figure 2.8: Waterfall plot of frequency responses (response level versus frequency) versus position for a stainless steel waveguide of length 69cm, radius 2.5cm, and wall thickness 2.5cm, filled with degassed water and driven with Gaussian noise. A hydrophone was used to take frequency response measurements at positions along the axis of the tube spaced by 5cm each.

What if the waveguide with one pressure release boundary were to be driven by a pure pressure source at the other end? In this case, the source condition at $x=0$ is given by

$$p(0,t) = P_0 e^{j\omega t}. \quad (2.34)$$

Setting Equation (2.22) equal to zero at $x=l$ reveals that $A=0$. Then, inserting Equation (2.34) into Equation (2.22) yields the coefficient,

$$B = \frac{P_0}{\sin(kl)}. \quad (2.35)$$

Thus, the acoustic pressure and particle velocity are described by the following two expressions:

$$p(x,t) = P_0 \frac{\sin[k(l-x)]}{\sin(kl)} e^{j\omega t} \quad (2.36)$$

$$u(x,t) = \frac{P_0}{j\rho c} \frac{\cos[k(l-x)]}{\sin(kl)} e^{j\omega t} \quad (2.37)$$

In this case, the acoustic pressure becomes unbounded when the denominator, $\sin(kl) = 0$, is zero. This yields modal frequencies that are integer multiples of half-wavelengths,

$$f_n = \frac{nc}{2l}, n = 1, 2, 3, \dots, \quad (2.38)$$

for the waveguide driven at one end by a pressure source and with a pressure release condition at the other.

Let us now consider a case where one end of the tube is driven by a pure pressure source and the other end of the tube has a rigid end condition. In this case the derivative of the pressure goes to zero at the rigid boundary. The derivation is left to the reader; the resonances are identical to the case of a waveguide with one velocity source and one pressure release boundary; odd integer multiples of quarter-wavelength modes.

Lastly, if one end of the waveguide is driven by a velocity source and the other end is rigid, the resulting resonances are identical to the case of one pressure source and one pressure release boundary, integer multiples of half-wavelength modes.

2.2.3 Plane Wave Resonance Modes

The response of a waveguide does not have to be extracted via a forced boundary or source. A waveguide can be driven or excited in a broadband fashion in a number of ways, and the resonance modes will depend only on the end conditions, not unlike the simple model of a string with ends that can be fixed or free. Intuition reveals that a waveguide with pressure release conditions at both ends or rigid conditions at both ends will resonate at frequencies described by Equation (2.38), and a waveguide having one pressure release and one rigid condition at its ends will resonate at frequencies described by Equation (2.33).

2.2.4 Non-ideal End Conditions

Not all end conditions are as ideal as that between, say, water and air, which can be modeled very well by a pressure release condition. Often realistic constraints will prevent the most easily achieved and ideal waveguide arrangements to be employed, and the finite acoustic impedance of the terminations may be significant. Let us consider an end piece of some material whose acoustic impedance is only twice that of the enclosed fluid. In this case the particle velocity and acoustic pressure will not be everywhere out of phase as in the case of a rigid end piece, and the reflection and transmission coefficients can be complex and frequency dependent. Also, the thickness of the end section can be important. In this case the tube end is modeled as a three-medium problem. The peak to peak pressure between pressure peaks and pressure nodes can be significantly decreased when compared to a pure rigid or pressure release boundary. Depending on the application, it is often desirable to design the waveguide such that this effect need not be accounted for. Furthermore, it is possible to use a known fluid and experimental conditions to characterize an end condition. This will be discussed in Chapter 3 and detailed in the results in Chapter 4.

2.2.5 Elastic Waveguide Effect

The preceding subsections have dealt with plane wave acoustics in a rigid-wall tube. It is important to understand what simplifications are being made when assuming

that the boundaries of a waveguide are rigid and how they can affect experiments; in the case of this work the effect can be quite important indeed.

It is well known that an ideal rigid-walled waveguide filled with a host fluid has a frequency-independent phase velocity of longitudinally propagating plane-wave modes that is equal to the intrinsic (*i.e.* unbounded) sound speed of the host fluid[56]. This is approximately the case for, say, a gas contained in a metal pipe; the specific acoustic impedance, ρc , of the wall is essentially infinitely higher than that of the host medium. For example, for air in a steel pipe, the impedance of the wall is higher than that of the gas by a factor of over 100,000. Thus, a pressure perturbation traveling through the gas cylinder creates no wall motion.

However, in the case of a liquid-filled waveguide, the impedance of the host medium can be non-negligible with respect to the wall. For the case of water in a steel pipe, the impedances are now mismatched by only a factor of about 32. In this situation, the motion of the wall due to a pressure perturbation in the fluid cannot be neglected.

The effect of waveguide elasticity has been of interest to scholars and experimentalists alike for over a century, and is well-published in the literature. In the same tome in which he considered the propagation of sound in a bubbly fluid, A. B. Wood also considered the effect of waveguide elasticity on low-frequency sound propagation through thick- and thin-walled waveguides, in what is perhaps the first

published investigation of such[41]. A few decades later, Del Grosso [57] derived an expression for the frequency-dependent phase speed through an elastic waveguide. In 1995, Lafleur and Shields [58] expanded upon Del Grosso's method, providing experimental verification as well as simplifications to the model itself. The analytical dispersion relation for axisymmetric wave propagation in an elastic waveguide developed by Del Grosso and Lafleur and Shields will be presented here with significant brevity, the reader is referred to [58] for more detail.

The geometry and coordinate system of the waveguide under consideration is shown below in Figure 2.9; the inner and outer radii of the tube are b and d , respectively, and the driving angular frequency shall be ω . In the case of the derivation the waveguide is considered to be of infinite length.

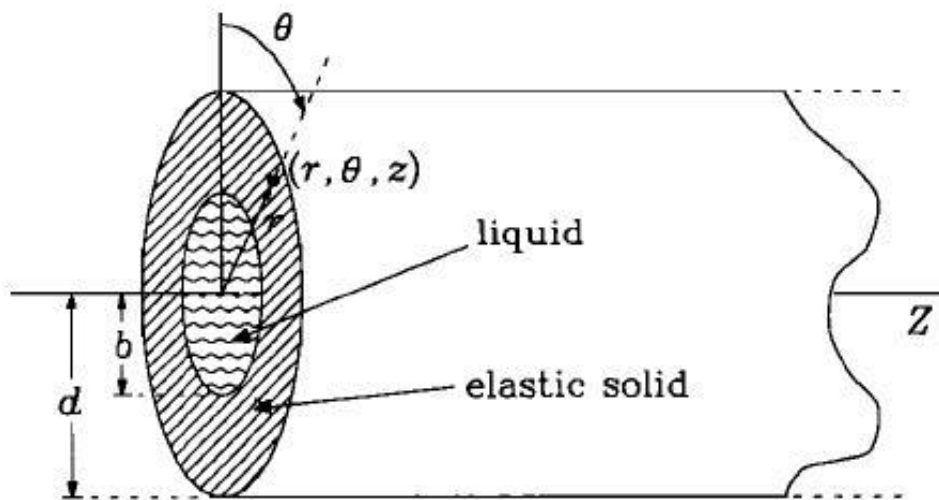


Figure 2.9: Coordinate system used to describe waves in a liquid contained in an elastic tube of inner radius b and outer radius d . Modes under consideration are θ -independent axisymmetric modes (from Lafleur and Shields [58])

As mentioned before, wall motion is non-negligible in an elastic waveguide. The particle displacement must thus be calculated in the radial and axial direction for both the fluid and the solid; the stress components will also be needed to apply boundary conditions. Following Del Grosso's presentation of the particle displacements in the radial and axial directions (in the tangential direction it is zero in this case), respectively, in the waveguide wall, we have

$$S_r = \frac{\partial \Phi}{\partial r} - \frac{\partial \Psi_\theta}{\partial z} \quad \text{and} \quad S_z = \frac{\partial \Phi}{\partial z} + \frac{1}{r} \frac{\partial (r \Psi_\theta)}{\partial r} \quad (2.39)$$

where Φ is a scalar displacement potential and Ψ is a vector displacement potential; together these comprise the displacement vector $S = \nabla \Phi + \nabla \times \Psi$. The radial and longitudinal stress components are thus

$$\sigma_{rr} = \lambda \left[\frac{1}{r} \frac{\partial (r S_r)}{\partial r} + \frac{\partial S_z}{\partial z} \right] + 2\mu \frac{\partial S_r}{\partial r} \quad \text{and} \quad \sigma_{rz} = \mu \left[\frac{\partial S_r}{\partial z} + \frac{\partial S_z}{\partial r} \right] \quad (2.40)$$

respectively, where λ and μ are in this case the Lamé constants, given by

$$\lambda = \rho_w c_t^2 \quad \text{and} \quad \mu = \frac{2\nu}{1-2\nu} \rho_w c_t^2, \quad (2.41)$$

where ρ_w is the density of the wall, c_t is the shear wave speed in the wall, and ν is the Poisson's ratio of the wall material.

The applicable boundary conditions across both the interface between the fluid and the wall and the interface between the wall and the outside space will be that no tangential stress exists, that the particle displacement remains continuous, and that the radial stress is equal to the acoustic pressure. These conditions can be expressed as

$$\begin{aligned}
\sigma_{rz} &= 0 & \text{at } r = b, \\
\sigma_{rz} &= 0 & \text{at } r = d, \\
\frac{-\sigma_{rr}}{S_r} &= \frac{P}{S_r} & \text{at } r = b, \\
\frac{-\sigma_{rr}}{S_r} &= \frac{P}{S_r} & \text{at } r = d.
\end{aligned} \tag{2.42}$$

Next we follow the notation of Lafleur and Shields. Applying these boundary conditions results in the expressions for the particle displacement in the fluid in the axial and radial direction, respectively,

$$S_z^L(r, z, t) = j\phi_0 q_{0m} J_0(rX_{0m}/b) e^{j(q_{0m}z - \omega t)} \tag{2.43}$$

and

$$S_r^L(r, z, t) = -(\phi_0 X_{0m}/b) J_1(rX_{0m}/b) e^{j(q_{0m}z - \omega t)}, \tag{2.44}$$

and the particle displacement in the waveguide wall in the axial and radial direction, respectively,

$$S_z^W(r, z, t) = \{jq_{0m} [AJ_0(rP_m) + BY_0(rP_m)] + T_m [CJ_0(rT_m) + DY_0(rT_m)]\} e^{j(q_{0m}z - \omega t)} \tag{2.45}$$

and

$$S_r^W(r, z, t) = \left\{ -P_m [AJ_1(rP_m) + BY_1(rP_m)] - jq_{0m} [CJ_1(rT_m) + DY_1(rT_m)] \right\} e^{j(q_{0m}z - \omega t)}. \quad (2.46)$$

In Equation (2.43) through Equation (2.46), variables are defined as

$$\begin{aligned} X_{0m} &= b\sqrt{k_1^2 - q_{0m}^2}, & P_m &= \sqrt{k_c^2 - q_{0m}^2}, & T_m &= \sqrt{k_s^2 - q_{0m}^2}, \\ q_{0m} &= \omega / C_{0m}, & k_c &= \omega / C_c, & k_s &= \omega / C_s, & k_1 &= \omega / C_1, \end{aligned} \quad (2.47)$$

where C_1 is the intrinsic velocity of sound in the liquid, C_c and C_s are the velocities of longitudinal (compressional) and transverse (shear) waves in the solid, C_{0m} is the phase velocity in the waveguide, and J_n and Y_n are the n th order Bessel functions of the first and second kind, respectively. The constants A , B , C , D are shown by Del Grosso to satisfy

$$\begin{aligned} &A \left(E_m J_0(dP_m) + \frac{P_m}{d} J_1(dP_m) \right) + B \left(E_m Y_0(dP_m) + \frac{P_m}{d} Y_1(dP_m) \right) \\ &+ C \left(-jq_{0m} T_m J_0(dT_m) + j \frac{q_{0m}}{d} J_1(dT_m) \right) \\ &+ D \left(-jq_{0m} T_m Y_0(dT_m) + j \frac{q_{0m}}{d} Y_1(dT_m) \right) = 0, \end{aligned} \quad (2.48)$$

$$\begin{aligned} &A [jq_{0m} P_m J_1(dP_m)] + B [jq_{0m} P_m Y_1(dP_m)] \\ &+ C [-E_m J_1(dT_m)] + D [-E_m Y_1(dT_m)] = 0, \end{aligned} \quad (2.49)$$

$$\begin{aligned} &A [jq_{0m} P_m J_1(bP_m)] + B [jq_{0m} P_m Y_1(bP_m)] \\ &+ C [-E_m J_1(bT_m)] + D [-E_m Y_1(bT_m)] = 0, \end{aligned} \quad (2.50)$$

$$\begin{aligned}
& A \left(E_m J_0(bP_m) + \frac{1+Q_m b}{b} Y_1(bP_m) \right) + B \left(E_m Y_0(bP_m) + \frac{1+Q_m b}{b} P_m Y_1(bP_m) \right) \\
& + C \left(-jq_{0m} T_m J_0(bT_m) + \frac{jq_{0m}}{b} (1+Q_m b) J_1(bT_m) \right) \\
& + D \left(-jq_{0m} T_m Y_0(bT_m) + \frac{jq_{0m}}{b} (1+Q_m b) Y_1(bT_m) \right) = 0,
\end{aligned} \tag{2.51}$$

where E_m and Q_m are defined

$$E_m = q_{0m}^2 - k_s^2 / 2, \quad Q_m = \frac{\rho_l \omega^2 b J_0(X_{0m})}{2\rho_w C_s^2 X_{0m} J_1(X_{0m})}, \tag{2.52}$$

where ρ_w and ρ_l are the densities of the tube wall and liquid, respectively.

In order to solve for the constants A , B , C , and D , their coefficients from the system of equations in Equation (2.48) through Equation (2.51) can be arranged in a 4 by 4 matrix; setting the determinant of this matrix equal to zero produces the constants and results in a characteristic dispersion relation between q_{0m} and ω ,

$$\begin{aligned}
& 1 + [L_{11}(P_m)L_{00}(T_m)] \left(\frac{\pi^2 q_{0m}^2 b d P_m^2 T_m^2}{8E_m^2} \right) + [L_{11}(T_m)L_{00}(P_m)] \left(\frac{\pi^2 b d E_m^2}{8q_{0m}^2} \right) \\
& + [L_{10}(P_m)L_{01}(T_m) + L_{01}(P_m)L_{10}(T_m)] \left(\frac{\pi^2 b d P_m T_m}{8} \right) \\
& + [bL_{11}(P_m)L_{10}(T_m) + d(1+Q_m b)L_{11}(P_m)L_{01}(T_m)] \left(\frac{\pi^2 P_m^2 T_m}{8E_m} - \frac{\pi^2 P_m^2 q_{0m}^2 T_m}{8E_m^2} \right) \\
& + [bL_{11}(T_m)L_{10}(P_m) + d(1+Q_m b)L_{11}(T_m)L_{01}(P_m)] \left(\frac{\pi^2 P_m E_m}{8q_{0m}^2} - \frac{\pi^2 P_m}{8} \right) \\
& + [(1+Q_m b)L_{11}(T_m)L_{11}(P_m)] \left(\frac{\pi^2 P_m^2}{8q_{0m}^2} + \frac{\pi^2 P_m^2 q_{0m}^2}{8E_m^2} - \frac{\pi^2 P_m^2}{4E_m} \right) = 0,
\end{aligned} \tag{2.53}$$

where $L_{mn}(\xi) = J_m(d\xi)Y_n(b\xi) - J_n(b\xi)Y_m(d\xi)$. Finding the zeros of Equation (2.53) will yield the phase speeds of each mode at a particular frequency. Below in Figure 2.10 is plotted Lafleur and Shields' theoretical model along with experimental data (circles) for an aluminum waveguide of inner radius 25.4mm and wall thickness 12.7mm, containing water. Note the flat dispersion-free region in the ET0 mode (using the notation in [58]; this is the plane wave mode) at low frequencies.

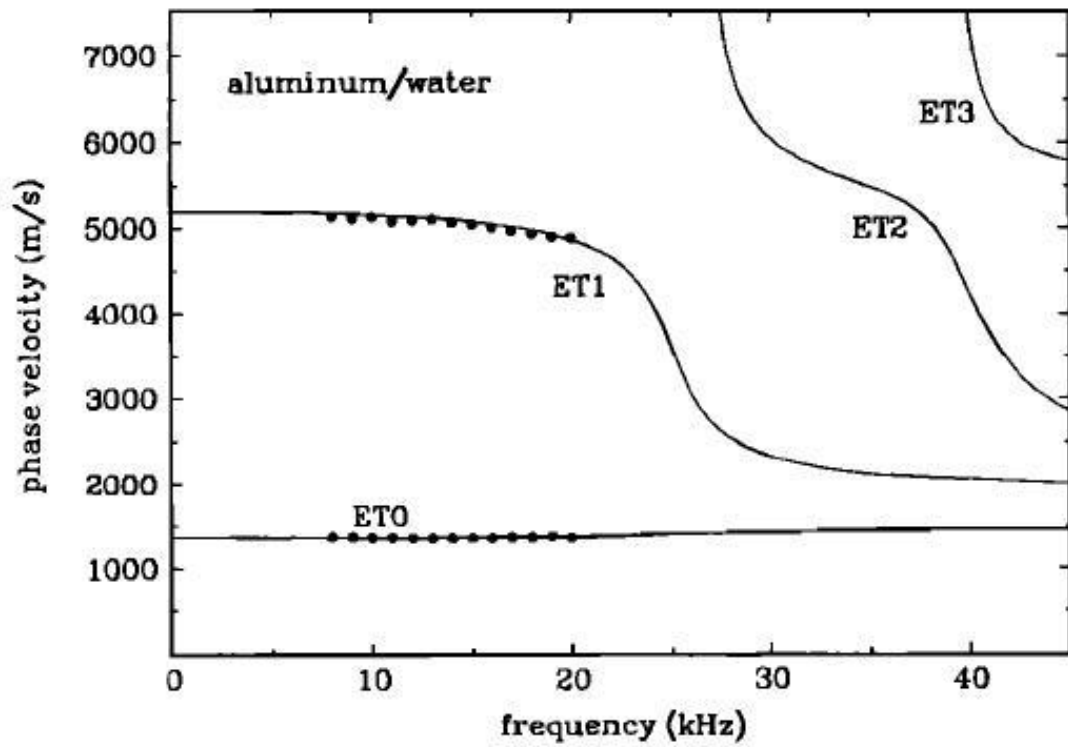


Figure 2.10: Phase velocity versus frequency for an aluminum water-filled waveguide with inner and outer radii of 25.4mm and 38.1mm, respectively. The solid circles represent measured phase velocity values (from Lafleur and Shields [58])

Note that the elastic waveguide effects will decrease with the addition of bubbles, since this increases the acoustic impedance mismatch between the wall and the fluid.

2.3 Combination

Combining the results of Sections 2.1 and 2.2 provides the theoretical physical foundation for this work, and paves the way for an experimental method that allows direct *in situ* measurement of bubbly flow void fraction measurement as long as several experimental constraints are met and several assumptions can be safely made.

Section 2.2 indicates that a waveguide device may be easily employed for the purpose of standing wave phase speed measurement via resonance frequency extraction, and that this phase speed can be related to an intrinsic fluid sound speed via an elastic waveguide effect model. Then, Section 2.1 indicates that this intrinsic fluid sound speed can be converted to a mixture void fraction via Wood's relationship.

Chapter 3

3 Materials and Methods

This Chapter will present the progression from the theory of Chapter 2 to an actual device and experimental method. The constraints and design considerations required for success of the resonator (waveguide), and how they were applied in the design stage, will be discussed. The device itself will be presented and all salient details provided along with the flow loop design and description of other auxiliary equipment. Lastly, the experimental method followed for use of the device will be presented in detail.

3.1 Acoustic Resonator Development

In order to construct a waveguide that will meet all the necessary design performance criteria, several areas of influence must act in concert: the application of acoustical theory to a realistic design, the practicality and ease of use of that

design, and satisfying the 'hard' number constraints put forth in the project proposal. This Section will delineate relevant design considerations.

3.1.1 Basic Proposed Design

Firstly, we must consider the best material from which to fashion the waveguide. The resonator tube will be constructed out of 316 stainless steel, which is chemically compatible (resistant to corrosion) with mercury. The tube will support the weight of the reservoir, mercury, transducer, and other elements; stainless steel is an ideal choice for constructing a structurally sound setup. Furthermore, the method of using the resonance modes of a cylindrical waveguide to determine the sound speed of the fluid mixture is most suitable for a waveguide that appears acoustically rigid to the fluid within the tube, as discussed in Section 2.2. Although stainless steel is not perfectly rigid, it has a very large acoustic impedance (roughly twice that of mercury).

In order to measure the *in situ* void fraction of the two-phase mercury-helium flow via the waveguide sound speed extraction technique, reason indicates that the design must allow for a fairly significant volume of bubbly mixture to be sampled in one measurement. This suggests a flow-through design in order to prevent the bubbly flow characteristics from changing. For example, if a fixed mixture sample were to be inserted into the resonator, the spatial distribution of bubbles and bubble radii could change, and also bubbles could rise out of the mixture.

Furthermore, a flow-through design will discourage bubbles from becoming trapped anywhere in the system. As such, a flow-through design will be employed.

To prevent bubble entrapment, the flow-through design should minimize stagnation points while retaining the characteristics of an ideal waveguide. To this end, the waveguide will use a spill-over design. Allowing the bubbly mixture to spill over the top of the waveguide and into a reservoir will provide several benefits for experiments. First, it will not allow bubbles to collect in any region at the top of the tube, which could modify the acoustic boundary condition. Second, the reservoir can allow any large 'rogue' bubbles that may have been created or coalesced to rise out of the mixture before they are re-circulated. Third, and perhaps most importantly, the liquid-air interface at the top of the tube created via a spill-over arrangement will provide a nearly ideal and non-dispersive acoustic pressure release boundary condition.

In keeping with the flow-through and spill-over design, a vertical orientation of the waveguide will further assist in a well-defined top boundary condition; it will also prevent bubble entrapment since buoyancy effects will act parallel to the flow direction, discouraging bubbles from exiting the flow.

In order to excite the fluid column, a transducer of some sort must be used. A typical acoustic transducer using a stack of PZT (lead zirconate titanate) disks or a piezoelectric element would need to be extremely large and massive in order to

work in the low frequency regime pertinent to this work. Instead of a transducer that works in this manner, relying on the volume expansion of a piezoelectric element due to an applied voltage to generate the long wavelengths required, a transducer that drives the fluid mechanically will be more efficient and less cumbersome. An electromechanical shaker is the specified driver for this effort.

Transducers that are inserted in the wall of a waveguide can cause significant changes in the response of a tube [38]. Therefore, it is desirable to drive the fluid column at one of its ends, or to insert a driving surface into the column through one of its ends. In a vertical flow-through spill-over arrangement, this provides two sensible options: drive the column from the bottom with a transducer that supports the fluid, or insert a driving surface through the top that fills only a portion of the tube. The latter is the chosen method in this case. A transducer that provides mechanical driving of the column from the bottom at low frequencies, is free to move while sealing against leakage, and also can support the weight of the fluid would likely be cumbersome and expensive. A shaker can be supported upside-down above the waveguide; attached to the shaker is a rod, on the end of which is a piston/disc, and this is inserted down into the fluid. Previous experiments [59] have shown that a piston that is half the radius of the waveguide provides enough driving surface area to effectively generate plane waves, but also does not affect the standing wave field along the whole waveguide, and allows fluid to easily flow past. Also shown was that if the piston is placed a few centimeters from the free surface,

it will be able to efficiently couple sound into the fluid and will not be at the null of any of the low frequency modes, thus all modes of interest can be resolved.

In order to record the frequency response of the resonator, a hydrophone is the instrument of choice. A hydrophone contains a calibrated piezoelectric element that will respond to pressure perturbations by outputting a voltage, which is the reciprocal process of how an acoustic transducer of a similar construction functions. The hydrophone signal can be converted to the frequency domain easily, and the frequency response of the waveguide obtained.

The location and mounting method of the hydrophone is also important. A true plane wave is impossible to generate in reality, due to diffraction, spreading, and other factors. The maximum plane wave signal will be present along the axis of the waveguide, though, so the hydrophone should be mounted in the center of the tube. Since the driver is inserted through the top surface, hydrophone insertion through this boundary would prove difficult. The bottom of the tube is the chosen mounting location for the hydrophone in this work. An end piece will be attached to the bottom of the waveguide to provide an acoustic boundary condition, support the enclosed fluid, and provide a mounting point for the hydrophone.

It is desirable for the unit to be somewhat modular, if possible without decreasing the effectiveness. The ability to try different end conditions, sources, and

configurations may be useful in testing the performance of the resonator and prevent the need for a 2nd generation resonator during the testing stages.

Lastly, it is desirable for the resonator to be suitable for use with both mercury and water. The unit will be designed for ultimate use and effectiveness in mercury; however, all initial tests and validations will be performed with water in order to evaluate its performance. Water is safe and expected experimental results with water are well established. Thus, the resonator will be essentially designed for both fluids with minimal changes required to use either effectively.

3.1.2 Parameter Choices and Justifications

The void fraction and bubble size distribution needed to most effectively mitigate cavitation damage erosion in the mercury target chamber remain unknown. However, various numerical modeling, simulations, and analytical and experimental work have been performed as described in Section 1.1.4. These published works provide a range of parameters that are desirable to probe with the waveguide. Based on this range and the resonator research project proposal, besides being functional with a pure fluid, the device should be able to probe void fractions from 10^{-6} to $5 \cdot 10^{-3}$. The resonator should also allow bubbles up to 500 microns in radius [60]. A safety factor in the ability to probe these parameters or modularity in the device to accommodate possible further investigations is also desirable. The material properties used in subsequent calculations are listed below in Table 3.1.

	Water	Mercury
Longitudinal (Compressional) Sound Speed (m/s)	1,497	1,450
Density (kg/m ³)	997.7	13,546

	Air	Helium
Longitudinal (Compressional) Sound Speed (m/s)	343	927
Density (kg/m ³)	1.21	0.1786
Polytropic Index	1.4	1.66

	Stainless Steel
Density (kg/m ³)	7,990
Longitudinal (Compressional) Sound Speed (m/s)	5,790
Transverse (Shear) Sound Speed (m/s)	3,225
Poisson's Ratio	0.275

Table 3.1: Tables of material parameters used for simulations and calculations

The wall thickness of the waveguide is an important parameter. The analytical models [57, 58] can account for the elastic waveguide effects when post-processing data for both preliminary water experiments and mercury experiments. However, there are various benefits to biasing the design towards an ideal rigid condition; similarly, there are disadvantages to a very thick-walled tube. Using Equation (2.53), the phase speed versus frequency for pure water and pure mercury were both calculated for a range of wall thicknesses. Pure liquids were used since the addition of bubbles will only serve to improve the apparent rigidity of the waveguide, so the pure liquid is the worst case scenario. Below in Figure 3.1 and Figure 3.2 are shown the phase speeds for stainless steel wall thicknesses of 6.35mm, 12.7mm, 25.4mm, 38.1mm, 50.8mm, and 101.6mm for water and helium, respectively. It is clear in the figures that as the wall thickness increases, each subsequent increase in phase speed towards the intrinsic sound speed is smaller. Since the mass is going up exponentially with a linear increase in wall thickness, a compromise between a thick wall and a practical resonator weight is needed. Following this rationale, a 12.7mm wall thickness is the dimension of choice for the resonator.

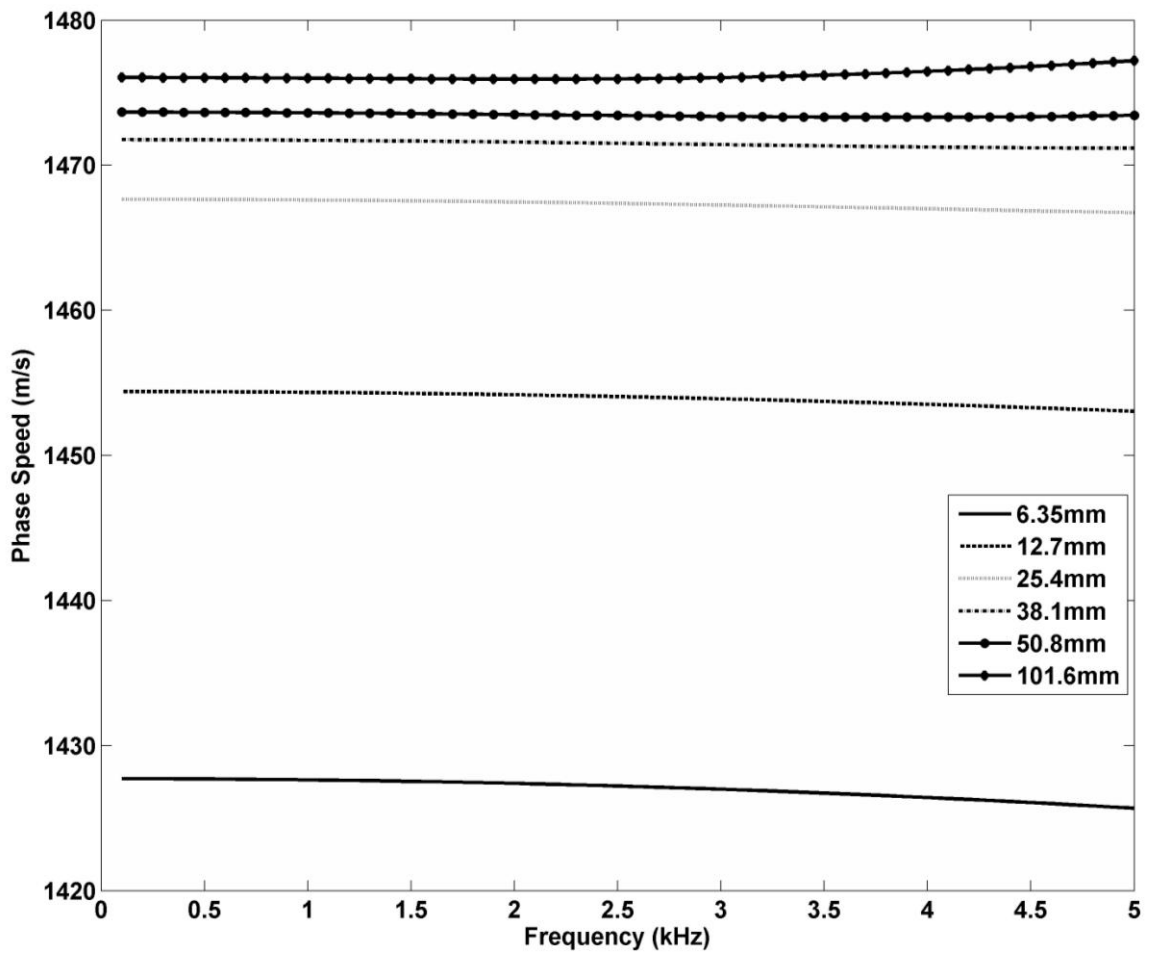


Figure 3.1: Computed phase speed versus frequency for a water-filled waveguide with wall thickness ranging from 6.35mm to 101.6mm. Intrinsic sound speed of the fluid is 1497 m/s.

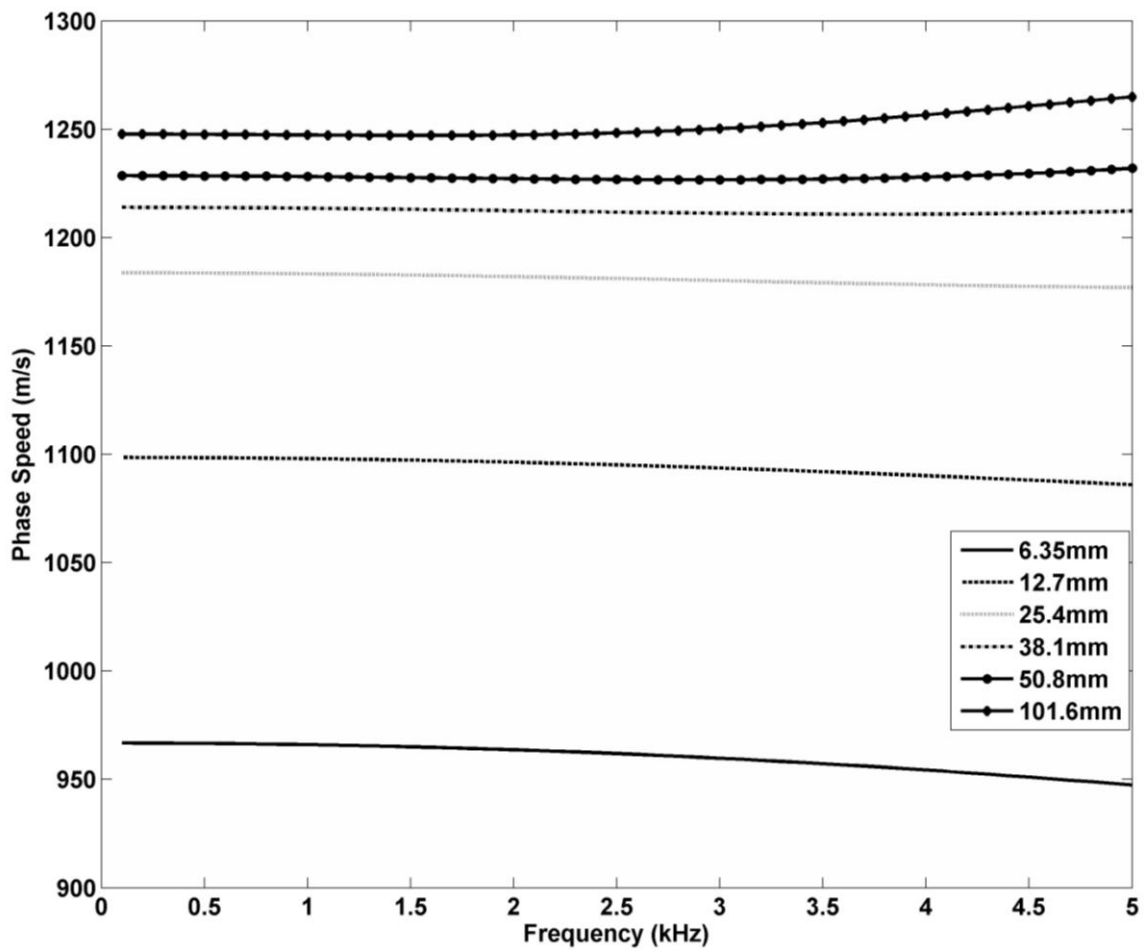


Figure 3.2: Computed phase speed versus frequency for a mercury-filled waveguide with wall thickness ranging from 6.35mm to 101.6mm. Intrinsic sound speed of the fluid is 1450 m/s.

The end boundary conditions of the resonator can have very prominent effects on the tube's acoustic response, as discussed in Section 2.2. The bottom boundary must also support the fluid and provide a secure mounting location for the hydrophone. If the bottom end piece provides a rigid boundary, the resonances are described by Equation (2.33); if it provides a 'soft' boundary, the resonances are described by Equation (2.38). For water experiments, using a 25.4 mm (1") thick stainless steel end piece provides a rigid boundary condition. When modeling the 1" plate and tube as a three-medium problem, the reflection coefficient can be described by

$$R = \frac{(1 - Z_1 / Z_3) \cos k_2 l + j(Z_2 / Z_3 - Z_1 / Z_2) \sin k_2 l}{(1 + Z_1 / Z_3) \cos k_2 l + j(Z_2 / Z_3 + Z_1 / Z_2) \sin k_2 l}, \quad (3.1)$$

where Z_1 , Z_2 , and Z_3 are the acoustic impedances of the fluid enclosed in the tube, the termination material, and air, respectively, l is the thickness of the middle medium (in this case the steel end piece), and k_2 is the wave number in the termination. The reflection coefficient given by this expression for the 1" plate and water does not indicate complete rigidity for the frequency range of interest. Shown below in Figure 3.3 are plotted the real and imaginary parts of the plane wave reflection coefficient versus frequency from 0-6 kHz for a three-medium problem of pure water, 1" of stainless steel, and air. The added data points on the x-axis indicate the expected locations of quarter-wavelength (indicating pure plane wave rigidity of the plate) and half-wavelength (indicating a pressure release characteristic)

resonance modes; these modes were calculated using the sound speed in pure water and a tube length of 40 cm (see pages 76 through 81 for choice and justification of tube length). A reflection coefficient of -1 indicates pressure release, a reflection coefficient of zero indicates perfect transmission, and a reflection coefficient of 1 indicates a rigid condition.

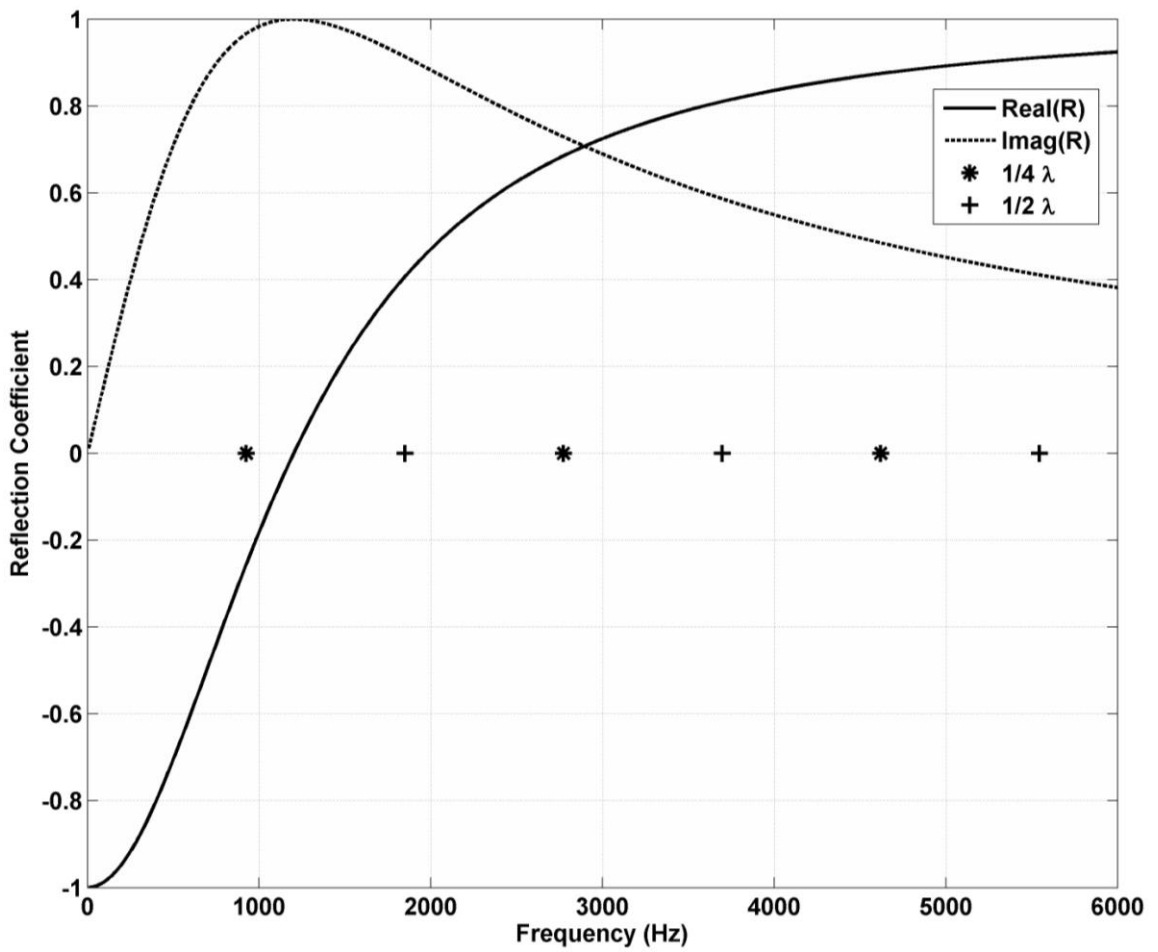


Figure 3.3: Real and imaginary parts of the plane wave reflection coefficient versus frequency for a three-medium scenario of water, 1" of stainless steel, and air. The data points place on the x-axis indicate the resonance modes of a 40 cm tube for both perfectly rigid (asterisks) and pure pressure release (crosses) conditions.

However, this expression only applies to cases with pure plane waves and a purely planar boundary condition. That will not be the case for our physical apparatus, since the plate is clamped around the edge. Indeed, water-filled tube acoustic behavior observed by previous investigators (Wilson [38], and others) suggest that the end condition will appear approximately acoustically rigid despite the results of Equation (3.1) due to the inability of the boundary to respond in a planar fashion. In the final analysis, the assessment of the bottom boundary condition will be made empirically through experiments with pure liquids with known acoustic properties, as described in the next Chapter.

For mercury, due to the increased impedance, it is more sensible to attempt a pressure release boundary condition; a 3.175 mm (1/8") thick stainless steel plate provides this boundary condition, can still support the mercury column, and still provides a mounting location for the hydrophone. In the future, an arrangement using a piston that drives the entire fluid column from the bottom surface may be used in an effort to further idealize both end conditions in the tube; this arrangement requires potentially costly transducers and non-trivial sealing solutions for the driving surface.

The length and diameter of the tube are two parameters that directly affect the usable frequency range of the resonator, based on the modal frequency equations

(Equation (2.33) and Equation (2.38), depending on the boundary condition) and the cutoff frequency equation (Equation (2.20)), respectively.

The radii of the BU acoustic resonator tube (denoted as b in Figure 2.9) and that of the piston face were chosen to be 25.4 mm and 12.7 mm, respectively. As discussed in Section 3.1.1, Wilson et al. [59] determined a 2:1 ratio of tube and piston dimension to be ideal for acoustic resonator experiments performed for determining the mixture sound speed. The tube radius along with the range of void fraction-dependent phase speed will determine the cut-off frequency of the cylindrical waveguide. The cut-off frequency shown in Equation (2.20) defines a limit for the driving frequency below which only the plane wave modes are excited in a rigid cylindrical waveguide. The cut-off frequency further imposes constraints on other parameters such as the tube length and range of bubble radius since the tube length and bubble population define the operational frequency range.

The bubbly mixture sound speed, the bubbly mixture phase speed in the waveguide, cut-off frequency associated with a 50.8 mm diameter tube, the fundamental modal frequency for a cylinder 40 cm in length (note for water $\frac{1}{4}$ wavelength modes are used and for mercury $\frac{1}{2}$ wavelength modes are used), the resonant bubble radius associated with this modal frequency (Minnaert's relation), and maximum permissible bubble radius (based on the driving frequency being half or less than the resonant frequency of the bubble to operate in the Wood's limit) are shown in

Table 3.2 for water and Table 3.3 for mercury over a range of void fractions. The mixture sound speed decreases with an increase in void fraction, as expected. Consequently, the cut-off frequency also decreases with increase in void fraction since it is dependent on the sound speed. The implications of these parameters on other design aspects will be discussed below.

Void Fraction	0	1E-6	1E-5	1E-4	1E-3	5E-3
Mixture Sound Speed (m/s)	1497	1485	1392	934	366	168
Mixture Phase Speed (m/s)	1454	1443	1357	923	365	168
Cutoff Frequency (kHz)	16.77	16.65	15.65	10.65	4.21	1.94
Modal (n=2) Frequency (kHz)	4.49	4.54	4.19	2.85	1.13	0.512
Resonance Bubble Radius (mm)	0.732	0.738	0.785	1.15	2.92	6.34
½ Resonance Bubble Radius (mm)	0.366	0.369	0.392	0.577	1.46	3.17

Table 3.2: Relevant values that determine the dimensions of the cylindrical resonator for water

Void Fraction	0	1E-6	1E-5	1E-4	1E-3	5E-3
Mixture Sound Speed (m/s)	1450	1432	858	328	106	48
Mixture Phase Speed (m/s)	1089	1037	762	323	106	48
Cutoff Frequency (kHz)	12.56	11.96	8.79	3.73	1.22	0.55
Modal (n=1) Frequency (Hz)	1344	1280	941	399	131	59
Resonance Bubble Radius (mm)	0.723	0.759	1.03	2.44	7.42	16.4
½ Resonance Bubble Radius (mm)	0.361	0.379	0.516	1.22	3.71	8.20

Table 3.3: Relevant values that determine the dimensions of the cylindrical resonator for Mercury

Mercury-filled resonator experiments will be performed in a ventilation hood, which has a vertical clearance of 122 cm (48"). Therefore the total apparatus height cannot exceed 122 cm. A small tube is preferable since a large setup would be heavy and unstable. Some acoustic considerations that impose a lower limit for the tube length are now discussed.

The relationship between the modal frequency and sound speed can provide the sound speed in the mixture if any one modal frequency is known accurately. However, the proposed technique can be made more robust by incorporating several modal frequencies in the determination of the mixture sound speed; this was expected to be very beneficial for water experiments that would be used to validate the performance, accuracy, and precision of the instrument. Thus, we chose to utilize the first three modal frequencies for determining the sound speed in water validation experiments. Since the modal frequencies depend on the length of the tube, the desired number of modes and the plane wave cut-off frequency impose a constraint on the length of the cylindrical resonator. The parameters in Table 3.2 show that the first three modes for a tube 5.08 cm in diameter and 40 cm in length are lower than the cut-off frequency of the tube for the range of void fractions of our interest (this remains true for mercury as well). This indicates that the resonator could be made with a larger inner radius if required. However, this would require a larger piston and likely a larger source to generate plane waves; for this reason, the

chosen diameter was not changed. Therefore, the Boston University resonator tube is 40 cm in length.

The relationship between the mixture sound speed and void fraction is independent of the bubble size distribution for driving frequencies that satisfy the Wood limit. Since void fraction is an unknown parameter, it is desirable for the resonator to accept bubble radii at or below the design parameter across the entire range of void fractions. For water, it is clear that bubbles of 366-micron radius and under will allow measurement of three modal peaks ($\lambda/4$, $3\lambda/4$, $5\lambda/4$) across the entire void fraction range. For mercury, bubbles of 361-micron radius and below will allow measurement of the fundamental modal peak ($\lambda/2$) across the entire void fraction range. Furthermore, as void fraction increases, the acceptable maximum bubble radius increases since modal frequencies decrease with the decrease in sound speed, allowing bubbles that resonate at lower frequencies to remain in the Wood limit. This added effect may seem inconsequential; however, restricting the bubble radius to the maximum acceptable radius for all void fractions is quite a conservative constraint. Also, recall that three modal peaks are being used; if only the first modal peak were to be used, the allowable bubble radius would increase by about a factor of six. For bubbly water validation experiments, only the first modal peak ended up being used. Details of this decision will follow in the results Section. Therefore, the as-designed acoustic resonator should provide reliable mixture sound speed measurements, and consequently void fraction extraction, as long as

the bubble radii remain within the expected project values. Furthermore, as void fractions increase, the resonator will be able to accept larger and larger 'rogue' bubbles (in addition to a larger mean bubble radius) without undesired effects, which is of tremendous built-in benefit.

3.2 Acoustic Resonator Description

The decisions developed in Section 3.1 provide an outline for the basic features of the resonator. From this point, the author designed an apparatus to be built, attempting to make sensible considerations for handling, ease of use, modularity, and other realistic aspects. The details of the resonator system will be presented in the sections below.

3.2.1 Main Resonator Assembly

A description of the resonator as constructed will be presented in this Section. Detailed engineering drawings can be found in APPENDIX A.

The resonator tube is 5.08 cm (2") in diameter and 40 cm (15.75") in length. The bottom 7.62 cm (3") of the tube is a separate section containing a 3/8" Swagelok inlet port; the inlet section is flanged on both ends and houses o-ring grooves to provide attachment and sealing capability, respectively. The main tube section is flanged on its bottom. The wall thickness for the entire tube is 1.27 cm (0.5") since it was shown in the previous sections that a thicker wall did not provide an appreciable acoustical benefit to offset the increase in weight and handling

difficulty. Choosing the wall thickness of 1.27 cm (0.5") over 2.54 cm (1") reduces the mass of the tube by 11.3 kg (25 lb). The inside surface of the tube was honed to a 16 finish (roughness features are no greater than 16 millionths of an inch in depth) to reduce surface imperfections in hopes of minimizing the attachment of bubbles to the tube wall.

In mercury, the bottom of the tube is closed using a 0.32 cm (1/8") thick plate 6.35 cm (2.5") in diameter to provide a pressure release condition (in water a 2.54 cm (1") plate is used to provide a rigid boundary condition). The plate has a borehole for inserting the hydrophone and a 0.64 cm (0.25") long cylindrical protrusion around the hydrophone casing to ensure a tight seal with the hydrophone's o-ring. The plate is held against the inlet section by compressing it between a flange at the inlet section bottom and an end piece. Proper seal is achieved using an o-ring between the flange and the plate. The end piece is rigidly mounted onto a base plate using 3/8" screws. The bottom face of the end-piece has a partial hollow cylinder that is inserted into the hole in a base plate to provide additional stability and alignment during assembly and disassembly while providing easy access to the hydrophone cable.

A base plate is necessary since the vertical tube design with the reservoir mounted near the top of the tube makes the construction top-heavy, even if the tube is filled with mercury. Therefore, a sturdy and stable support system is necessary to prevent

the setup from tipping over. To facilitate easy access for the hydrophone cable and to allow leveling of the apparatus, the base plate was mounted on three pre-fabricated adjustable feet (McMaster-Carr 83685T12). Stress distribution in the base plate in this configuration was modeled for the case of point-load equivalent to the tube/reservoir setup and maximum deflection was estimated to be 0.1 mm. Therefore, a base plate thickness of 1.27 cm (0.5") was deemed sufficient for supporting the apparatus.

To facilitate the spillover fluid flow and re-circulate the fluid back into the tube, a stainless steel reservoir is mounted near the top of the tube. The base of the cylindrical reservoir is welded 7.30 cm (2.875") below the top edge of the tube. The height of the reservoir was chosen to allow two NorCal weld stub viewports with a 6.35 cm (2.5") view-through diameter to be mounted on the reservoir for monitoring the mercury level and spillover behavior. The bottom of the reservoir contains a 3/8" Swagelok outlet port for the mercury to exit, and an auxiliary NPT threaded port intended for the use of a thermocouple to monitor fluid temperature. The reservoir is covered with a lid 1.27 cm (0.5") thick, which also serves as the platform for the shaker system. A flange is attached to the top of the reservoir to facilitate the use of an o-ring and bolts to obtain a proper seal with the lid. The cover also has four NPT threaded auxiliary ports for the attachment of any diagnostics (pressure gauges, etc). There is a hole in the center of the lid to allow insertion of the piston and movement of the piston shaft. The shaker assembly is mounted onto

the reservoir cover with rubber pads between the shaker and cover. This attachment is via a circular pinch collar around the main shaker body that is supported by four columnar spacers through which the mounting bolts attach to the lid.

Although the lid seals the reservoir along the edge, mercury fumes are free to escape from the entryway for the piston shaft. To prevent these fumes from escaping, another cylindrical enclosure is mounted over the shaker system. Into the top of this cover is welded a hermetically sealed connector allowing electrical through-connections to provide the driving signal to the shaker. An NPT threaded port also on the top of the shaker cover is used to attach a carbon filter for trapping mercury fumes. Two handles are welded to the reservoir to facilitate handling the apparatus.

The shaker of choice for the BU acoustic resonator is a Ling Dynamic Systems (LDS) V203 permanent magnet vibrator. The LDS V203 is a small, but relatively powerful for its size, electromechanical shaker. The unit is cylindrical with a radius of about 35mm and is approximately 90 mm tall. The V203 can provide armature displacements of +/-5 mm and maximum accelerations of 136 g's, and weighs about 3 kilograms. The unit has a usable frequency range from 5-13,000 Hz, and the armature resonance frequency is 13,000 Hz.

The hydrophone chosen for the BU acoustic resonator is a Reson TC4013 miniature reference hydrophone. This hydrophone has a usable frequency range from 1 Hz to

170 kHz over which its response is virtually flat (within +/- 3 dB). The TC4013 has a high receiving sensitivity and is very compact, weighing only 75 grams; the acoustic portion of the unit has a length of only 25 mm and a diameter of 9.5 mm. Below the acoustic sensing portion of the hydrophone, the body diameter is decreased and houses an o-ring; this allows the hydrophone to be pressed into a properly-sized hole to provide both mounting and sealing solutions. Lastly, the unit is constructed of stainless steel and butyl rubbers, making it both robust and mercury compatible. This makes the TC4013 ideal for use in the resonator.

A diagram of the overall resonator assembly is shown below in Figure 3.4. Note that a linear ball bearing alignment assembly for the shaker piston shown in the diagram was deemed unnecessary and cumbersome in practice. In Figure 3.5 is shown a 3D assembly drawing of the resonator as provided by the machining contractor. In Figure 3.6 is shown a photograph of the resonator assembly (*sans* shaker cover).

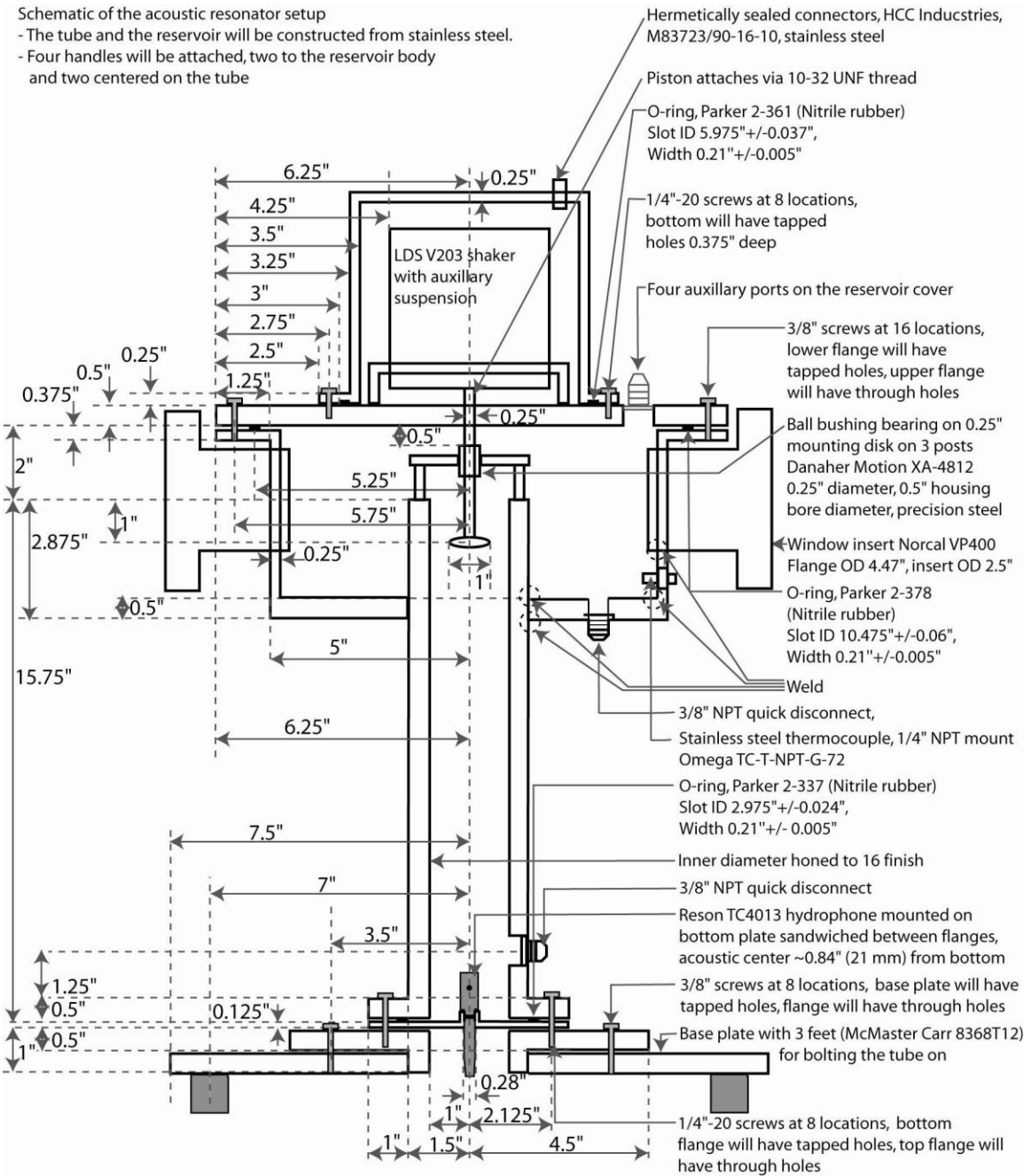


Figure 3.4: Detailed schematic of the Boston University acoustic resonator assembly

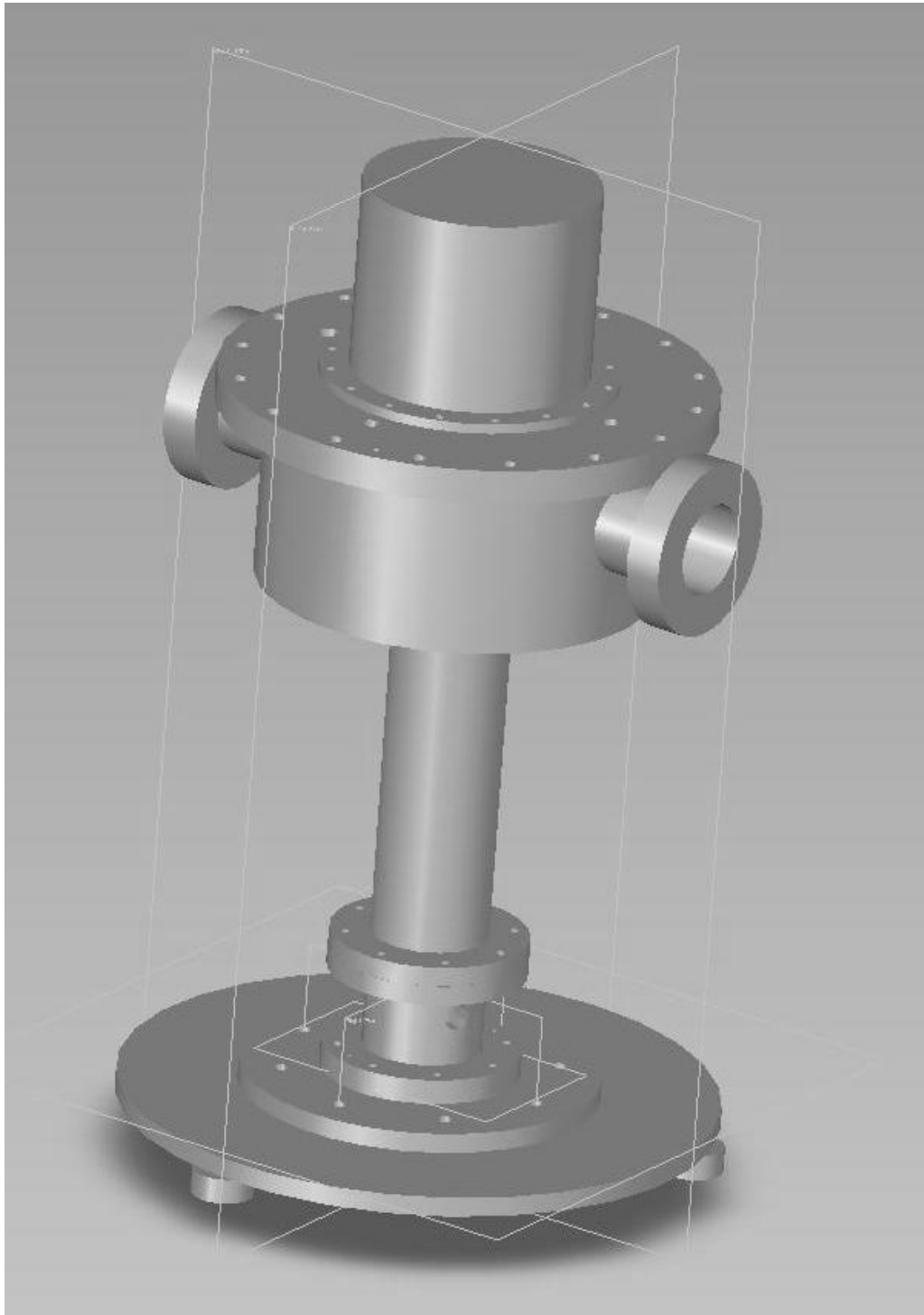


Figure 3.5: Three-dimensional CAD model of the resonator assembly



Figure 3.6: The acoustic resonator assembly. In this particular photograph the shaker cover is not attached, and the reservoir outlet tubing is disconnected.

3.2.2 Flow Loop

Components constituting the fluidics of the BU acoustic resonator system were carefully chosen to be compatible with mercury and to provide a modular design for added convenience.

A Cole Parmer 7552-02 peristaltic pump is used to drive the fluid flow loop and is controlled by a Cole Parmer 7552-71 controller. Pre-calibrated peristaltic pumps offer precise control over flow rates and can run dry without causing damage to the pump. Furthermore, they allow the fluid to be handled while the only equipment physically in contact with the fluid is the tubing itself; this is beneficial for handling bubbly fluids since pump cavitation is not a concern. It is also beneficial for handling mercury since it is toxic and corrosive. This particular pump has a stainless steel rotor in a polyphenylene sulfide housing and provides a flow rate ranging up to 2300 ml/min and a discharge pressure of 15 psi (which is twice the hydrostatic pressure due to the 40 cm mercury column in the resonator) when used with Masterflex L/S 36 Norprene tubing, the tubing of choice. This tubing is also mercury compatible. The configuration of the loop for both water and mercury experiments is detailed below.

For water experiments, the pump was placed on a cart next to the table supporting the resonator in order to reduce the effect of pump vibrations on measurements.

Since water experiments are intended to validate the performance of the device, it is desirable to inject known void fractions and not re-circulate the fluid, since small bubbles would remain entrained in the flow. A fish tank was filled with clean water for the pump to draw from. The outlet tubing of the pump connects to the bubbler, which then connects to the resonator inlet. The outlet of the resonator is routed to a 35 gallon Nalgene bottle on the floor, allowing the spillover reservoir to drain via gravity. Thus no fluid re-circulates, and the maximum experiment time is determined by the available water volume in the fish tank.

For mercury experiments the loop is closed and a fixed depth of mercury is maintained in the spillover reservoir. The pump and all tubing must be placed in the fume hood with the resonator for safety purposes. The pump is placed on foam pads in a secondary containment tub and the tubing is run through a trough of sand to reduce vibrations. The lid and shaker cover are all installed and o-ring seals achieved. A pressure gauge in one of the auxiliary ports serves as a precautionary diagnostic since the system is sealed.

3.2.3 Bubbler and Gas Metering System

In order to inject gas into the flow, a custom-made sintered porous stainless steel sparger unit from the Mott Corporation is used. This bubbler is constructed entirely of stainless steel tubing. There are two concentric tubes; the outer is solid and the inner has a short porous section. The outer section acts as a 'jacket' allowing for

pressurization. Fluid flows through the porous section of tubing which is subject to pressure from the outside; the fluid flow shears off small bubbles as gas is forced through the pores. For bubbly water experiments, a squirt of Rain-X (SOPUS Products, Houston TX) was added to discourage bubble coalescence and keep the individual bubble radii small. Besides ensuring that the Wood limit is satisfied, additional efforts to keep individual bubble radii small also decrease the relative rise velocity of the bubbles with respect to the fluid rise velocity; this is an effect that must also be accounted for.

A laboratory air line is stepped down to 15 psig by a stainless steel 500 psi regulator. This pressure is then provided to an Omega model FMA-A2402-(**) electronic mass flowmeter/controller. This unit allows air flow metering and control from 0-50 SCCM with +/- 0.05 SCCM precision and +/- 1% of full scale accuracy. Between the flowmeter/controller and the Mott sparger, a small Luer-lock valve can either allow air coming from the flowmeter to go to the Mott unit, or vent it to the atmosphere.

For water experiments, directly following the Mott unit and directly preceding the resonator inlet was placed a section of square acrylic tubing with inner diameters of 5.17 mm for optical investigation of bubbly flow. A fiber optic panel light placed below the flow cell to provide back lighting. A QImaging Retiga CCD with Navitar lens was positioned above the flow cell and focused near the top surface of the

inside volume. After a bubbly resonator measurement was taken, the pump was shut off, allowing all the bubbles to rise up to the top of the flow cell. An image was captured for later processing in order to glean the bubble size distribution of the flow.

A photograph of the bubbler and gas metering system, along with the resonator and some flow loop components, is shown below in Figure 3.7.

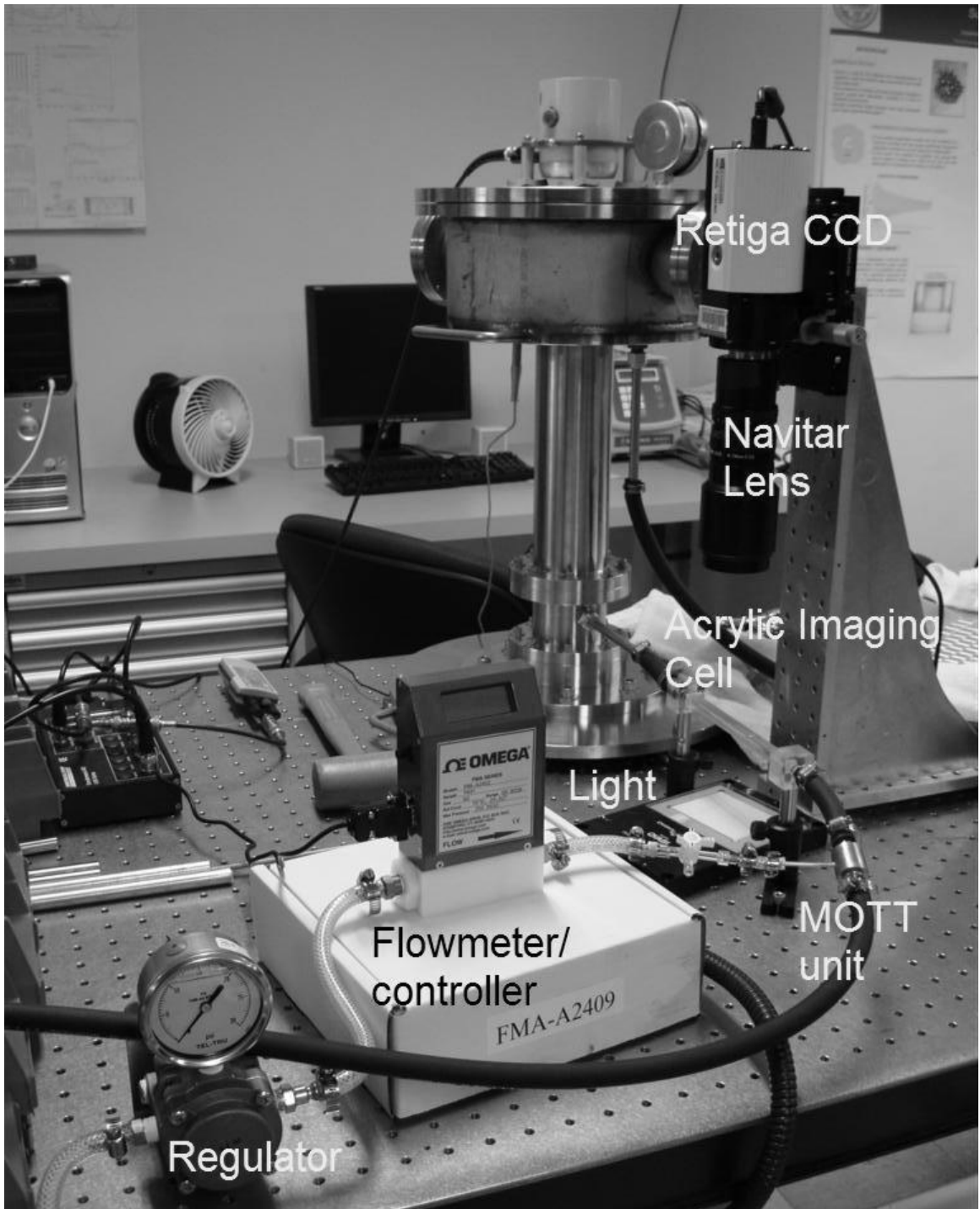


Figure 3.7: Bubbler and gas metering system

3.2.4 Auxiliary Equipment

Auxiliary instruments incorporated into the resonator system for signal processing and conditioning are detailed below.

A Dell Inspiron 9400 laptop with MATLAB performed processing and control for all experiments. The laptop is a high-end unit with the processing power of a desktop, but its portability aids in conducting experiments in different laboratories (including ORNL, ultimately). The BU Physical Acoustics Laboratory (PacLab) has extensive experience using MATLAB for signal generation, instrument control, data acquisition, numerical modeling, and post-processing, making it the software of choice.

A Data Translation DT9836-06-02-BNC simultaneous USB data acquisition board is the electronic core of the resonator system. The DT9836-06-02-BNC has 6 analog inputs and 2 analog outputs; it allows simultaneous operation and internal or external triggering of analog input and output, digital input and output, and counter/timer subsystems. Both analog input and output are 16-bits and throughput speeds are 225 kHz and 500 kHz, respectively. The simultaneous capability of the board is of tremendous benefit for this work; the DT9836 allows determination of the response across a device under test to stimuli at the exact same instant. One of the 32-bit internal counter/timers can be used to trigger

simultaneous and synchronous input and output. The unit is standalone, with its own power supply, a convenient metal enclosure, BNC connections for all inputs and outputs, and a USB 2.0 connector for control by the laptop. Lastly, the DT9836 supports the DAQ adapter for MATLAB, a plug-in for MATLAB's Instrument Control Toolbox allowing direct control of the DT board from MATLAB.

A Crown CE1000 audio amplifier is used to amplify the waveform being sent to the shaker. This is a high quality audio amplifier with a working frequency range of 20-20,000 Hz. The maximum power output is 1100 Watts.

A Krohn-Hite Corporation model 3944 4-channel filter/amplifier is used to enhance the measured hydrophone signal. This unit offers Butterworth and Bessel filters of the high pass, low pass, bandpass, and bandreject varieties; all filters provide a 24 dB per octave attenuation slope. Each channel can provide gains of 0 dB or 20 dB on both the input and the output.

Threaded into the underside of the bottom of the spillover reservoir is an Omega TC-T-NPT-G-72 pipe plug thermocouple probe for monitoring the temperature of the fluid. This is useful for water experiments since the variation of sound speed in water with temperature is a well-known and published trend that we can account for. The thermocouple plugs into an Omega SMCJ-T thermocouple to analog converter/connector. This unit converts a thermocouple input signal to a cold junction compensated, linear, amplified analog output signal that varies 1mV per

degree Celsius; this signal is collected at one of the DT9836 board's analog input terminals during the period of data acquisition for an experiment and the time-averaged value is used to calculate the intrinsic sound speed of the water at that temperature.

3.3 Overall System

Thus, the combination of the resonator apparatus, flow loop, bubbler and gas metering/injection system, and auxiliary equipment constitutes the entire acoustic resonator system; a standalone system for measuring the free gas void fraction of bubbly fluid flows. Below in Figure 3.8 is shown a simplified diagram of the entire system.

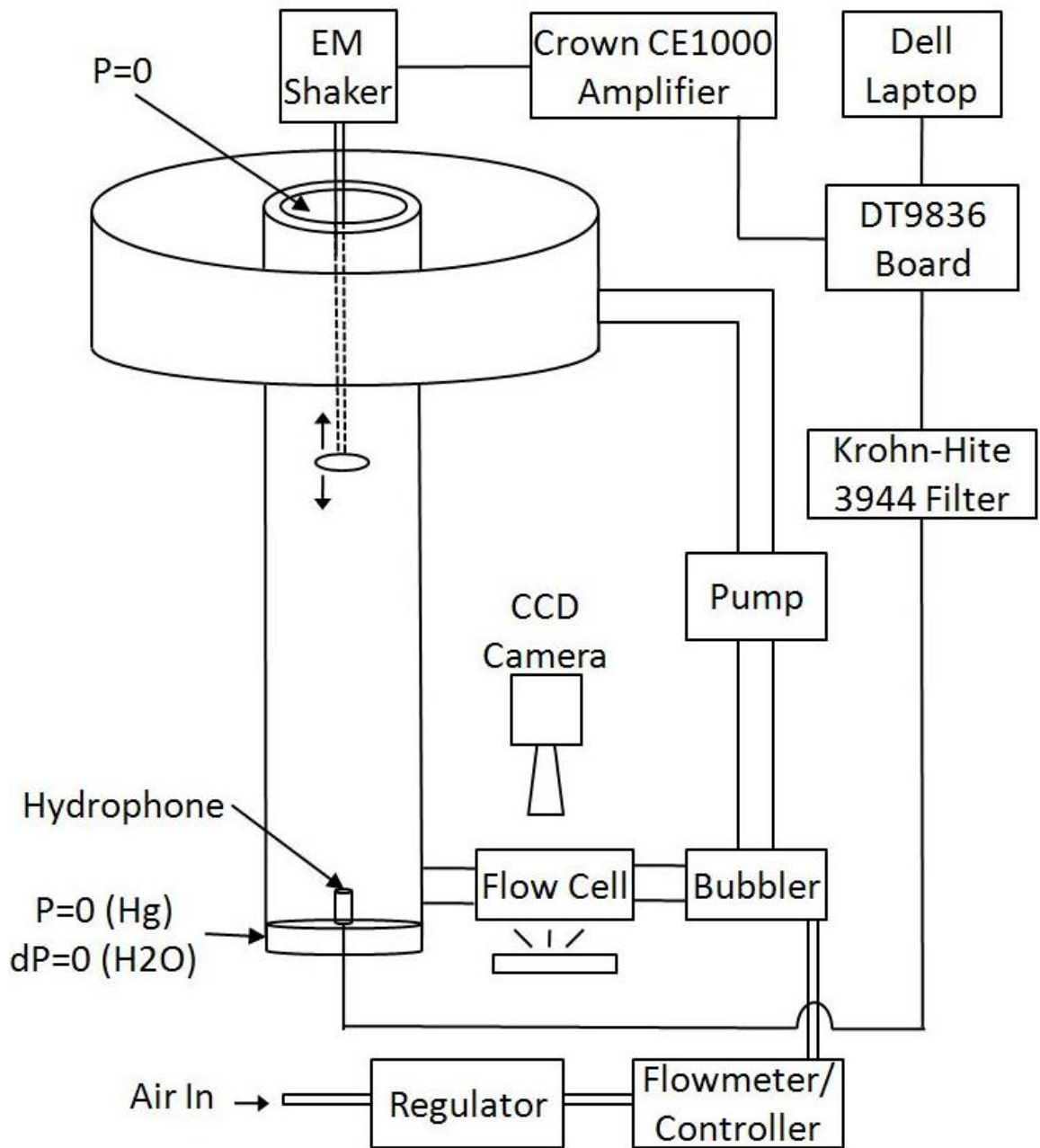


Figure 3.8: Diagram of the Boston University acoustic resonator system in its entirety (not to scale)

3.4 Experimental Method

This Section will describe the process of setting up various types of experiments, driving the resonator, extracting and recording data, and processing data. The details of the MATLAB scripts developed to run experiments will also be discussed.

3.4.1 Experimental Setup - Pure Water

For pure water experiments, the chief focus is ensuring that the experiment is carefully set up and the water and tube are prepared vigilantly. The tube must be free of bubbles and the water free of gas. This experiment is essentially making a measurement of something for which we already know the answer in order to verify that the unit is functioning properly, so setup is critical.

First, a few liters of clean spring water are put into a large flask and degassed with a vacuum pump for approximately 30 minutes. The inner wall of the resonator is cleaned and a small inline valve is attached to the inlet port. The clean, degassed water is carefully poured into the resonator and the valve is used to let a small amount of water flow out; this ensures that the inlet port section is full of clean water and contains no gas cavities. Enough water is also poured into the spillover reservoir to cover the element tip of the thermocouple for temperature measurement. The tube is then allowed to sit for a few hours to ensure that any

small cavities which may have formed are taken back into solution by the gas-starved liquid.

3.4.2 Experimental Setup – Bubbly Water

For bubbly water experiments, as discussed in Section 3.2.2, the fluid is not recirculated. A 5 gallon jug of spring water is poured into the fish tank, a squirt of Rain-X is added, and the tank is stirred with a rod. The fluid is pulled from this tank by the pump, pushed through the resonator, spills over into the reservoir, and drains out into a holding tank. The valve to the Mott unit is closed and the flowmeter/controller is set to the desired air flow rate. The pump is turned on and the air valve is opened. It takes several moments for the pores of the Mott unit to be cleared of fluid and for the flow to become bubbly. The bubbly fluid is allowed to flow for at least twice the time it takes the pump to fill the tube. Experiments can now commence as desired. After the desired experiments are complete, the flow is stopped and all the bubbles in the flow rise to the top surface of the flow cell, and an image is captured. Between individual flowing bubbly mixture experiments, striking the tube 15 or so times with a deadblow hammer and using a curved piece of rubber sheet on a rod to squeegee the tube walls both remove any bubbles that may have attached in the resonator. When the fish tank runs dry, the experiment must be reset.

3.4.3 MATLAB Code – Initialization and Signal Generation

The next few Sections discuss the MATLAB script and subscripts that control experiments. In all cases, “input” refers to measurements and “output” refers to the driving signal.

First in the main experiment script is the initialization of variables. These are user-chosen parameters that depend on the type of experiment desired to be run. For example, the starting and ending frequency of the driving sweep, the output voltage to the shaker, input and output board sampling rates, number of desired averages, and the desired time length of each individual driving frequency sweep are all parameters that are initialized at this point in the script, among others.

An auxiliary script is called that creates the waveform that will eventually drive the shaker. This waveform is a sweep that is linear in time, which sweeps from a starting frequency to an end frequency in a fixed time (all user-defined). The sweep is desired to be output multiple times in order to do averaging on the tube’s response, so multiple identical sweeps are concatenated together into one large waveform³. However, doing this creates a very sharp transition from the highest frequency to the lowest frequency at the junction of each individual sweep. This is

³ The author has investigated experimentally the effect of using multiple frequency sweeps. At the beginning of all sweeps but the first, the low frequency response can be seen in the form of a modulation/envelope of higher frequency ‘ringing’. This ringing is believed to be beneficial for SNR as well as to ensure that the entire response is captured. In the first sweep, there is no high frequency ringing carried over from the previous sweep, since there is no previous sweep. As such, the first sweep is ignored.

undesirable because sharp transitions in the signal could cause instruments to respond dynamically, providing odd effects or damaging equipment. Thus, a Tukey window with a 0.1 ratio, which is a combination of a square window with a cosine-squared window applied to 10% of the window width at the beginning and end of each sweep, is applied to the waveform. This creates a smooth transition between sequential sweeps. The entire waveform and its corresponding time vector are thus created as MATLAB variables. Once the waveform has been created, windowed, appended to itself as many times as averages desired, it is time to begin the input and output preparation process.

The entire input and output process is synchronous. The DT9836 has an internal clock; the output of this clock is connected to the trigger input of the board so that it can be used to simultaneously trigger the input and output subsystems. The DT9836 board is then initialized. The analog input system for incoming hydrophone data is configured and its triggering is setup. A second input channel is also set up for the thermocouple. The same occurs for the analog output subsystem which will provide the driving signal to the Crown amplifier and ultimately the resonator. The configuration of both systems consists of specifying the sampling rate, buffer mode and size, trigger type and condition, and other parameters.

3.4.4 MATLAB Code – Data Output and Acquisition

Next, the actual input and output of data are performed. The output waveform data is queued into the output buffer, and the output and input are started or ‘armed’. Upon receipt of a trigger command, the first signal from the internal clock causes the long waveform to be output while simultaneously data is acquired using the ‘getdata’ function. ‘Getdata’ is a blocking function, so no further commands are entered until it has completed its acquisition. The data is brought in as a raw vector of voltages with length dependent on sampling rate, number of averages, and sweep time. The thermocouple voltage is also being simultaneously recorded. The input and output are then stopped. At the end of the synchronous input/output time window, the measured signals are brought from the board’s input buffer to the computer for handling in MATLAB.

3.4.5 MATLAB Code – Post-processing and modeling

With the raw data imported into MATLAB, it can now be processed and manipulated to provide meaningful results. The temperature voltage data is converted to a temperature value by time-averaging the voltage and using the calibration curve provided with the unit. This temperature value is used to calculate the intrinsic sound speed of the fluid at that temperature; this intrinsic sound speed value is then used in the Lafleur and Shields model later. The long vector of hydrophone data is segmented into an array with each column corresponding to the individual output

sweeps. Each of these can be considered a frequency response of the resonator. A 20,000 point FFT with 2.5 Hz resolution is performed on each response and converted to a dB scale referenced to the driving waveform output voltage of the board; these FFT are then averaged.

An automated process picks out the modal frequency peaks based on a set of criteria. First, a smoothing algorithm eliminates small perturbations in the frequency response. Then, all possible combinations of three peaks are picked out and put into a vector. Combinations that yield a non-physical sound speed (supersonic) or have any peaks with widths below a threshold (outliers/noise) are removed. Lastly, since the three modes must represent the $\lambda/4$, $3\lambda/4$, and $5\lambda/4$ modes, as implied by Equation (2.33), this constraint is applied to each set of three peaks and a total error is calculated. The set of three peaks with the minimum error is chosen as the true modal peaks. A linear fit is performed on the three modal peaks, and the slope of the line is equated to the slope in Equation (2.33). The effective sound speed of the bubbly mixture enclosed in the resonator is thus extracted.

Since the phase speed is the parameter measured by the resonator, obtaining a sound speed using the Lafleur and Shields dispersion relation (Equation (2.53)) is an inverse problem, and an optimization routine must be utilized. A MATLAB function performs a single-variable bounded nonlinear function minimization to

extract the sound speed and then uses the low-frequency propagation expression (Equation (2.18)) to calculate the void fraction. The produced result is the void fraction correlating to a mixture with the phase speed measured in the resonator; a chosen tolerance determines how precisely the optimization routine matches the sound speed before outputting a final value for the void fraction.

3.4.6 Image Processing – Bubbly Water

After all bubbly measurements for a given airflow rate (*i.e.* void fraction) have been made, the flow is stopped, all bubbles rise in the flow cell, and an image is captured. This image is then used to extract the bubble size distribution of the flow by identifying all of the bubble radii in the frame.

First, the image is binarized and thresholded to separate the background from the bubble boundaries. A MATLAB function is then used to ‘fill the holes’ in the image, leaving a binary image with black background and many white circles corresponding to the bubbles. Since bubbles can exist very close to one another, especially at higher void fractions, simply calculating the area of each white entity would provide a large error. Instead, a circular mask is created, starting with a radius larger than any of the bubbles, and it is scanned over the image. If it crosses a place where the space beneath it is entirely white, that is chosen to be a bubble; that space is colored in black and the bubble radius is stored in a vector. The mask is then redefined with a one pixel smaller radius and the process is repeated. After the

process is complete, a vector of bubble radii (in pixels) remains; this vector is then converted to radii via a calibration based on the width of the acrylic flow cell chamber.

Chapter 4

4 Results and Discussion

This Section will present and discuss experimental results and conclusions that can be drawn from them when making comparisons to the theory. Experiments with clean bubble-free water for initial instrument validation will be described. Experiments with bubbly water of varying void fraction will also be detailed. Preliminary mercury tests at Boston University and a description of planned future tests at Oak Ridge National Laboratory are presented.

4.1 Pure Water Results

In scientific experiments, it is always desirable to make a measurement of something for which we already know the answer, especially in the early stages of a new experiment or device. Since the sound speed of water for a given temperature is well known, and the elastic waveguide effects can be accounted for via a model,

initial resonator validation measurements were attempted with pure, degassed water (void fraction of 0).

The tube was filled with clean, degassed water as discussed in Section 3.4.1 and driven with six 200ms linear frequency sweeps from 0-5 kHz; the source level output from the board was 1 Volt, which is then sent to the Crown amp. The voltage given to the shaker was roughly 12V peak. Below in Figure 4.1 is shown the measured hydrophone signal, after two 60 Hz high pass filters and a 20 dB amplification, versus time. Due to the synchronous driving and measured signals (both sampled at 100 kHz), this plot thus represents the real-time response of the resonator to such a sweep. Based purely on qualitative observation, one can see that the envelope of the hydrophone signal traces out three clear maxima. If 'ringing' is neglected and the tube is assumed to respond virtually instantaneously, this envelope should roughly trace out the shape of the frequency response spectrum.

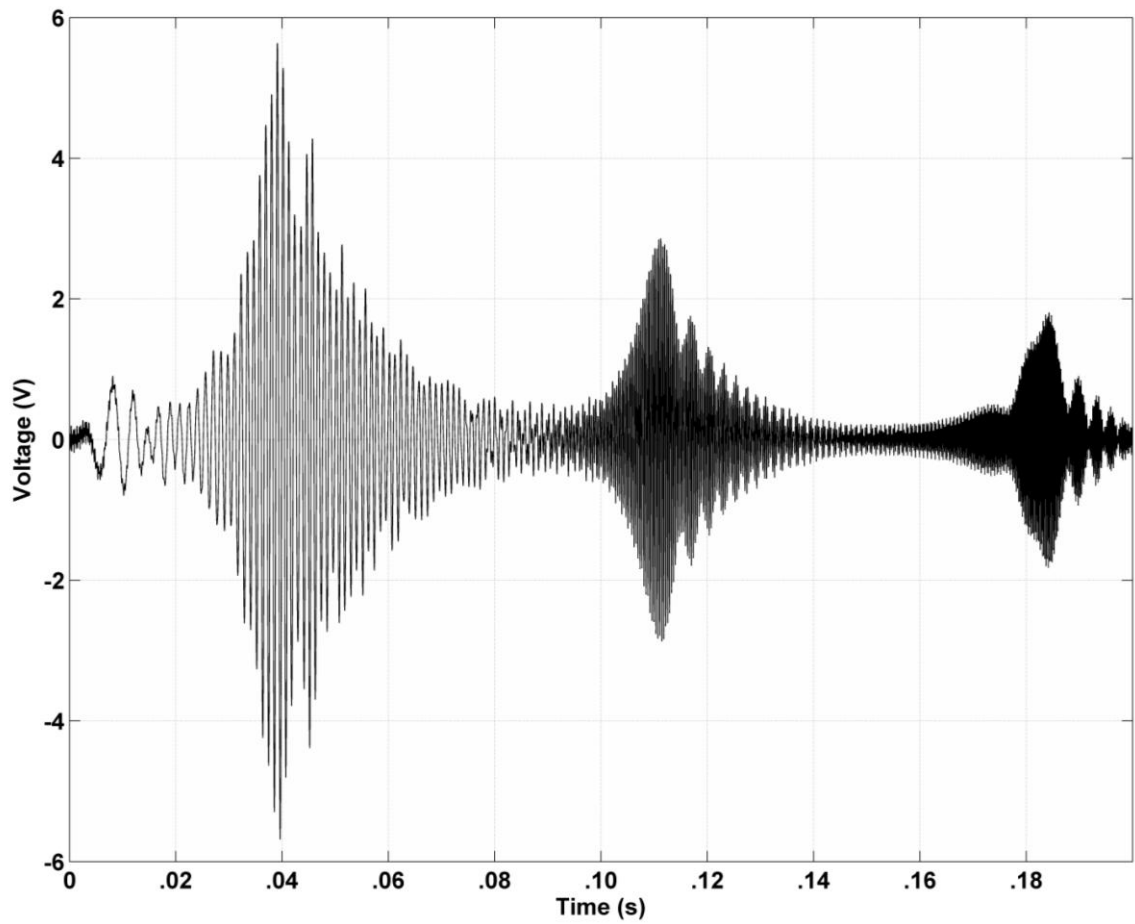


Figure 4.1: Measured hydrophone signal post-amplification and filtering versus time for the resonator filled with pure, degassed water and driven by a 200ms linear sweep from 0-5 kHz

The time signal shown in Figure 4.1 was then processed as discussed in Section 3.4. The frequency response spectrum is shown below in Figure 4.2. The circles on the three large peaks denote the modal resonances chosen by the peak-choosing algorithm. The vertical line at 900 Hz was placed manually at this first peak, the other two vertical lines are multiples of the first frequency based on the odd-integer quarter wavelength modes expected to be present in the tube. Thus, the fact that the second and third lines correspond with the measured peaks indicates that the expected linearity of plane wave modes is present.

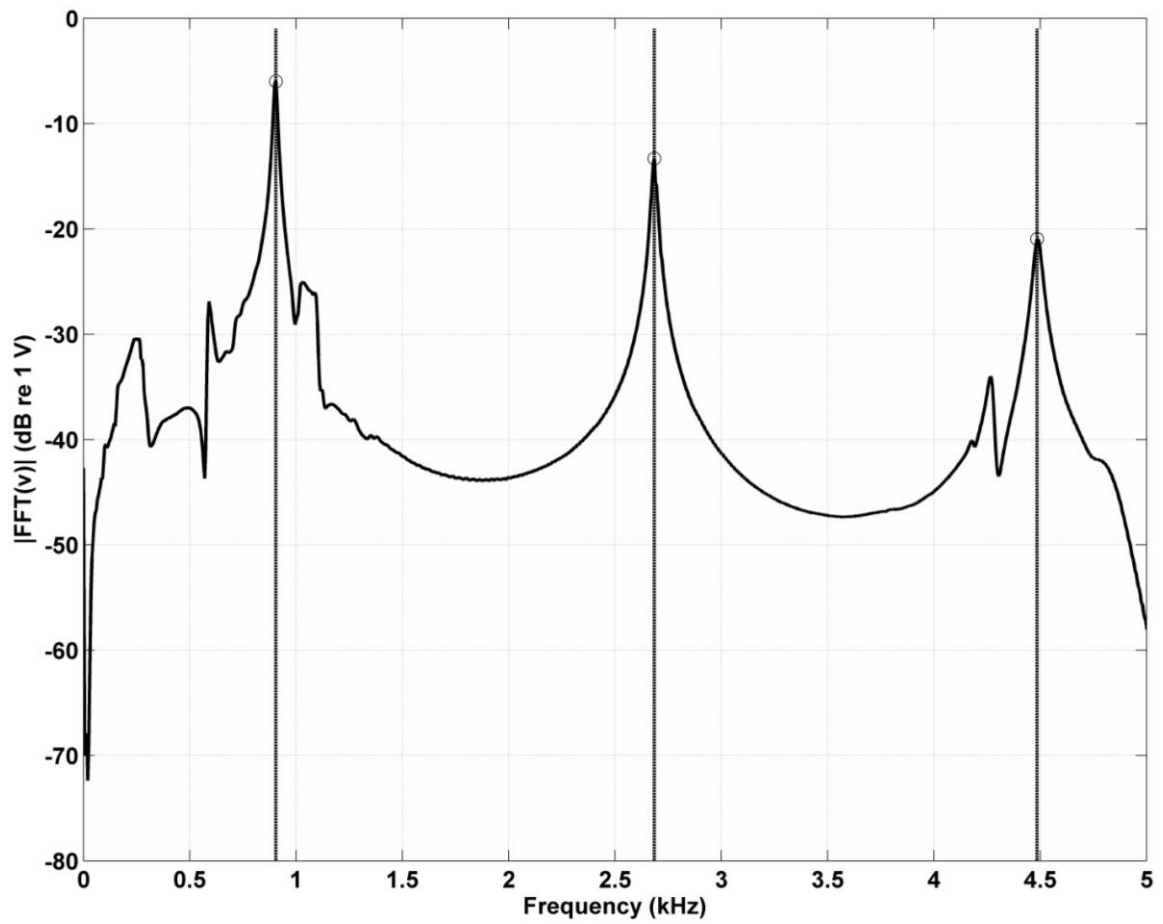


Figure 4.2: Average frequency response level versus frequency for the resonator filled with pure, degassed water and driven by six 200ms linear sweeps from 0-5 kHz

A linear fit was performed on the three modal frequencies extracted from the frequency response spectrum in Figure 4.2 and is shown in Figure 4.3. The correlation coefficient is approximately unity, indicating a linear relationship. The slope is then used with Equation (2.33) to calculate the measured mixture sound speed. This mixture sound speed is then used to plot what the expected modes would be if, assuming the liquid air interface provides a perfect pressure release condition, the bottom plate were to provide a perfect pressure release condition ($\lambda/2$, λ , and $3\lambda/2$ modes) or a perfect pressure doubling condition ($\lambda/4$, $3\lambda/4$, and $5\lambda/4$ modes). This provides an estimate of how ideally the boundary condition is acting; the excellent correlation with the $\lambda/4$, $3\lambda/4$, and $5\lambda/4$ modes indicates the boundary is acting rigidly, despite Equation (3.1), which indicates a dispersive boundary condition over this frequency range. We attribute this to the fact that the plate is clamped along its edge and thus constrained in motion. A more detailed treatment of this complex problem would require extensive FEM (Finite Element Model) work and is beyond the scope of this thesis. Since pure water is the ‘worst case scenario’ in terms of the impedance mismatch between the fluid and the termination material, characterizing the boundary condition in this manner for pure water indicates that for all bubbly water mixtures, the end condition will be rigid as well (although the modal frequencies will be decreased and wavelengths will be longer, the impedance of the mixture drops more significantly (see Figure 2.7), maintaining the rigid characteristic of the termination). The Lafleur and Shields

model script is updated with the temperature garnered from the thermocouple data and the intrinsic sound speed of the water is modified accordingly. Lastly, the optimization routine described in Section 3.4.5 is used to calculate the void fraction. The extremely small resulting void fraction of $5.55\text{E-}18$ can be considered to be zero.

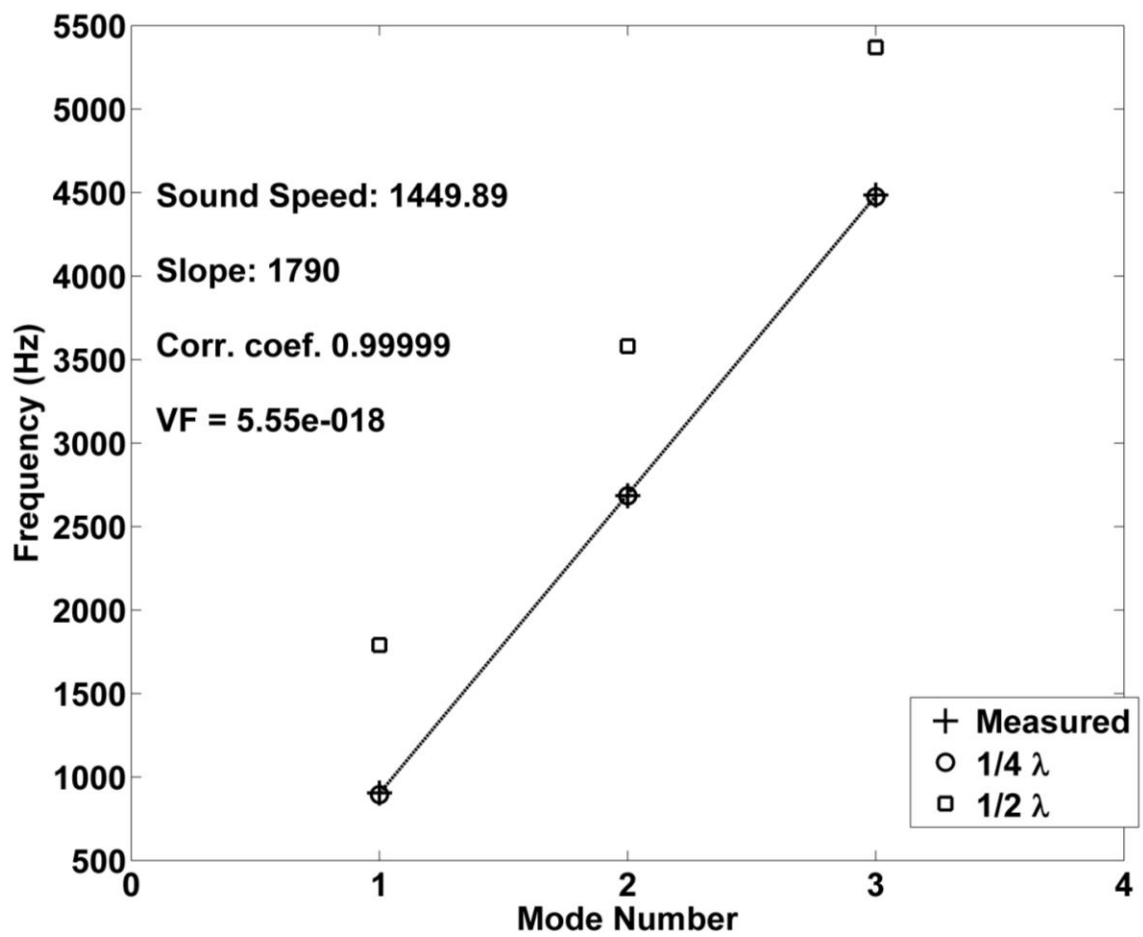


Figure 4.3: Plot of mode number versus frequency for the modal peaks extracted from the spectrum in Figure 4.2

The phase speed predicted by the model for a void fraction of zero differs from the value of 1449.9 m/s measured in this case by 4.4 m/s; this error is made insignificant by the resolution uncertainty in the FFT (+/- 2.5 Hz) and the uncertainty in the fluid column height (+/- 0.5 mm, this uncertainty in the column height exists due to the fluid meniscus at the top of the tube during experiments that serves to lengthen the tube by 5 mm with this uncertainty) and their resulting effect on the uncertainty in the phase speed, which is also 4.4 m/s. The propagated uncertainty in a dependent variable due to the uncertainty in an independent variable can be expressed as

$$u_{f(x)} = \frac{df(x)}{dx} u_x, \quad (4.1)$$

where $u_{f(x)}$ and u_x are the uncertainties in the dependent and independent variables, respectively. If the dependent variable is a function of multiple variables, the uncertainty is expressed as

$$u_{f(x_1, \dots, x_n)} = \sqrt{\sum_{i=1}^n \left(\left(\frac{\partial f(x_i)}{\partial x_i} u_{x_i} \right)^2 \right)}. \quad (4.2)$$

Therefore, since the sound speed is dependent on the tube length and frequency as $c_0 = 4lf$, the propagated uncertainty in the phase speed given by the fundamental resonance peak can be expressed as

$$u_{c_0} = \sqrt{(4lu_f)^2 + (4fu_l)^2}, \quad (4.3)$$

where u_f and u_l are the uncertainties in the frequency and the length, respectively.

In this case, the length is 0.405 m and the frequency is 900 Hz.

Furthermore, using the slope of the linear fit and Equation (2.33) yields that the expected first mode should be 895 Hz; the 5 Hz difference is encompassed by the resolution of the FFT, indicating that not only is the linearity of the modes upheld, but also that the boundary is acting rigidly to the enclosed fluid. Combining these two observations proves that the resonator is truly measuring the standing plane wave quarter wavelength modes as predicted by the theory outlined in Chapter 2.

The trial discussed above clearly demonstrates the accuracy of the instrument. Additionally, further investigations were performed to ensure the precision of the instrument and explore the sensitivity to parameter and experimental changes as well as the effect of some non-idealities of the resonator assembly. These will not be discussed in thorough detail, but one prominent result will be presented.

An experiment was performed using clean, degassed water that would validate the precision of the resonator. In order to do this, the water was flowed in a closed loop to ensure no evaporation would affect the column length. A measurement akin to the one discussed directly above was taken every 10 minutes until 100 measurements had been taken. The histogram of sound speeds is shown below in Figure 4.4. The time variance of these sound speeds showed no trend. The distribution of sound speeds is over four times smaller than the 4.4 m/s uncertainty

in the phase speed due to the uncertainty in the fluid column length and FFT at the frequency of the first modal peak. This phase speed uncertainty will decrease with decreasing frequency, since the uncertainty in the phase speed due to the column height uncertainty is frequency dependent. Thus, the precision of the instrument is limited by the two aforementioned uncertainties even though performance has indicated the precision is smaller.

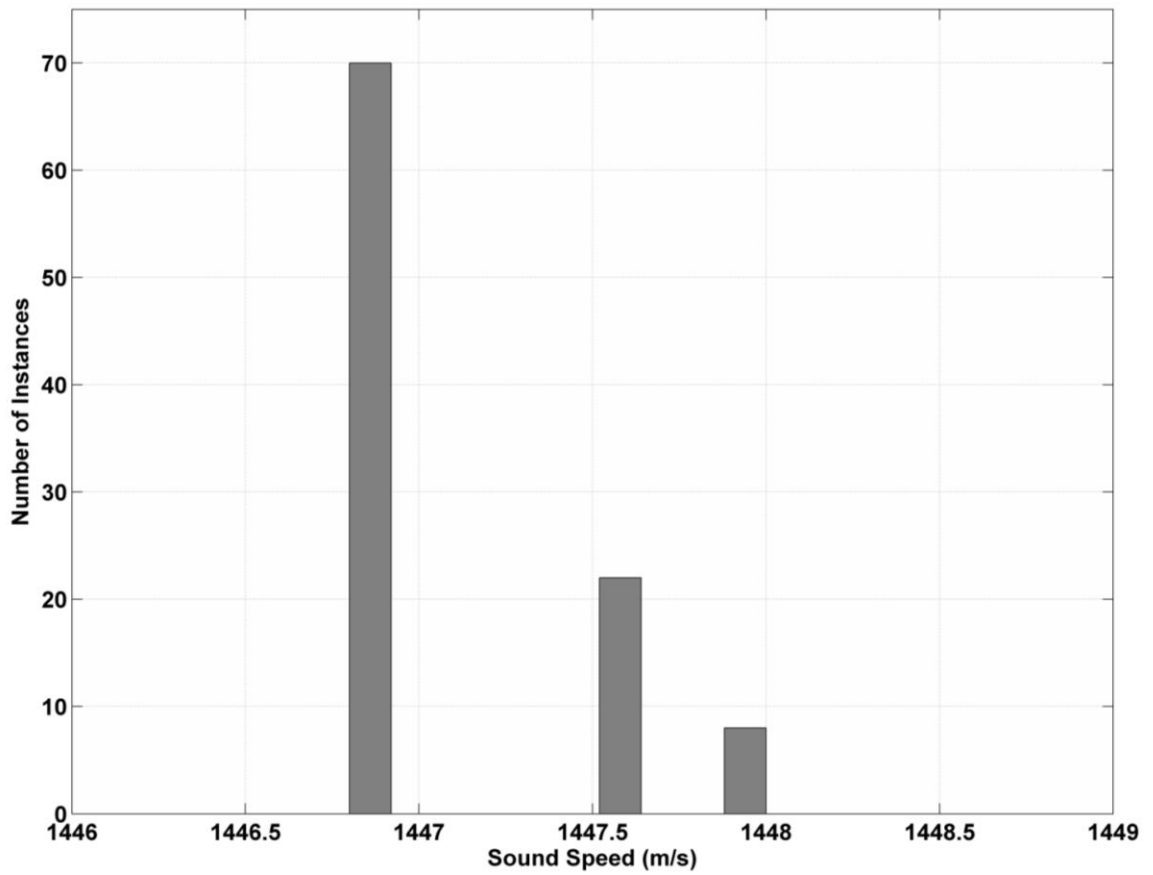


Figure 4.4: Sound speed distribution for a 100-measurement precision investigation over 16 hours

4.2 Bubbly Water Results

This Section will discuss results obtained from resonator experiments performed with bubbly water of varying void fractions. These experiments were intended to, and ultimately did, provide results that would validate the instrument and its ability to measure the void fraction of bubbly fluid flows. The inherent difficulty in doing this is that the resonator was designed to truly be the “gold standard” in measuring bubbly fluid void fraction, so validating its performance is nontrivial and intrinsically problematic. However, after devising a method for doing this, validation of the instrument was satisfactorily achieved. It is the opinion of the author that the resonator itself still does provide a measurement with unmatched accuracy and precision as long as the constraints delineated in the theory remain true.

4.2.1 Wall Attachment Phenomenon

When running initial bubbly water experiments with the setup and method described in Chapter 3, the author discovered an interesting phenomenon. As air was introduced to the fluid and flow continued, bubbles would become attached to the waveguide wall, primarily in the upper third of the resonator tube. A non-linear spacing of modal frequency peaks appeared in the response spectra as the bubbles became attached.

In order to investigate this phenomenon, tests were performed that would monitor the response of the waveguide before, during, and after the introduction of air via the bubbler. Resonator measurements were taken approximately every four seconds; these were 'standard' measurements consisting of five 200 ms sweeps from 0-5 kHz. Since both clean and bubbly water would be investigated, the frequency range needed to be large enough to accept the first three modal peaks of pure water, thus the 5 kHz upper bound. Tests began flowing clean bubble-free water; the flowmeter/controller was set to the desired air flow rate with the flow diverted to the atmosphere. During this time, spectra were identical to the results discussed in Section 4.1.

After about one minute, the air valve is directed to the Mott bubbler unit. The spectra do not immediately change since the air must force fluid out of the pores in the sparger. Then, as bubbly fluid begins to fill the tube, the modal peaks begin to shift to lower frequency as expected. Shown below in Figure 4.5 is the resonator frequency response at the approximate time the tube is completely filled with the bubbly mixture (the time for a fluid particle to travel through the entire tube is about 20 seconds). The dotted lines again indicate the expected second and third modal peaks based on the fundamental resonance mode. In this case the linearity is as expected.

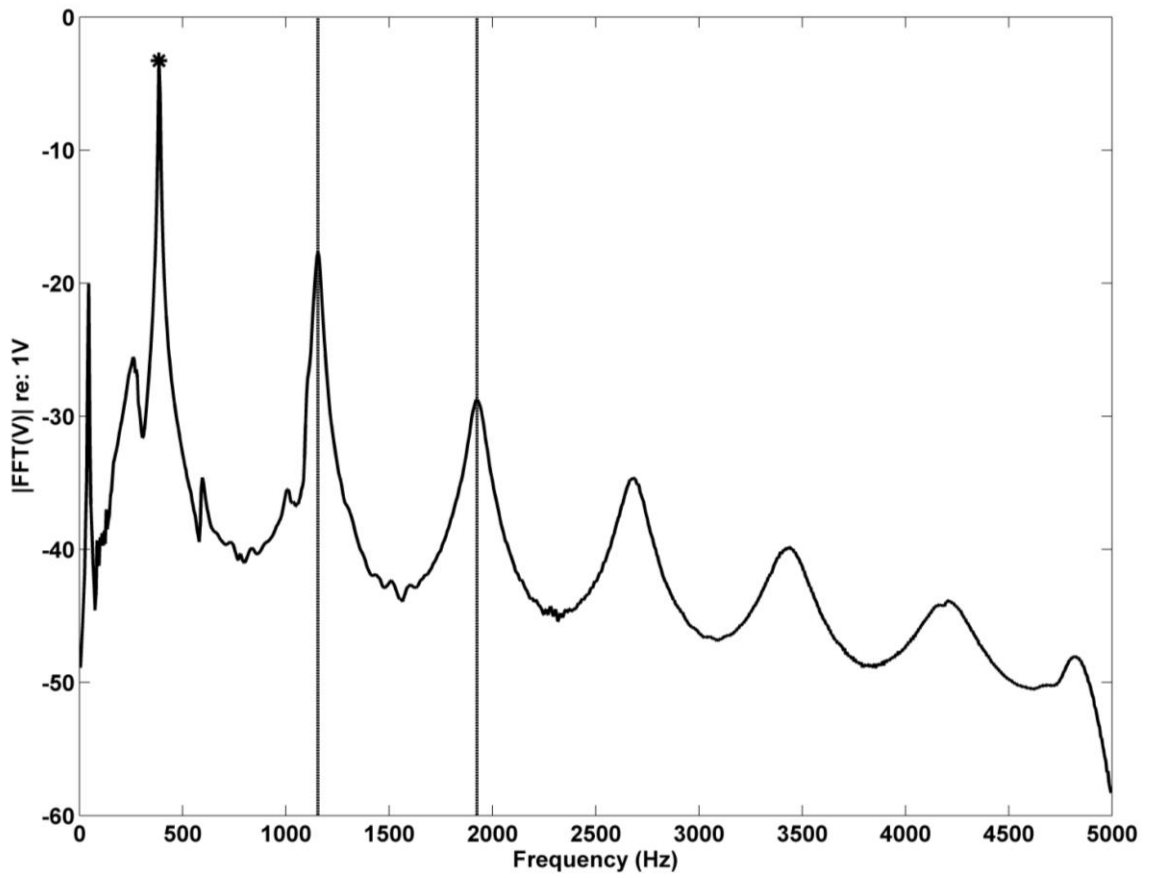


Figure 4.5: Frequency response level vs. frequency for the resonator flowing newly-introduced bubbly water at the approximate moment it has completely filled the tube, driven by 200 ms linear sweeps from 0-5 kHz

As bubbly fluid continued to flow, peak shifts continued to occur. However, the first modal peak remained at exactly the same modal frequency; the higher-order modes continued to shift to the left. This non-linear peak spacing is believed to be caused by a dispersive wall boundary condition due to the presence of bubbles, leading to a complex higher-order effect. Furthermore, since the dynamic effect of realistically sized bubbles is more likely to affect higher frequencies, this lends credence to the observed robustness of the first modal peak. Below in Figure 4.6 is shown the frequency response of the resonator after flowing bubbly mixture for about 20 seconds (not including the time taken to initially fill the tube with bubbly mixture, *i.e.* this response is 20 seconds after Figure 4.5). The dotted lines based on linear extrapolation of the first peak have begun to stray from the measurement. Further below in Figure 4.7 is shown the frequency response of the resonator after flowing bubbly mixture for about 5 minutes. The dotted lines based on linear extrapolation of the first peak are further uncorrelated to the measured peaks.

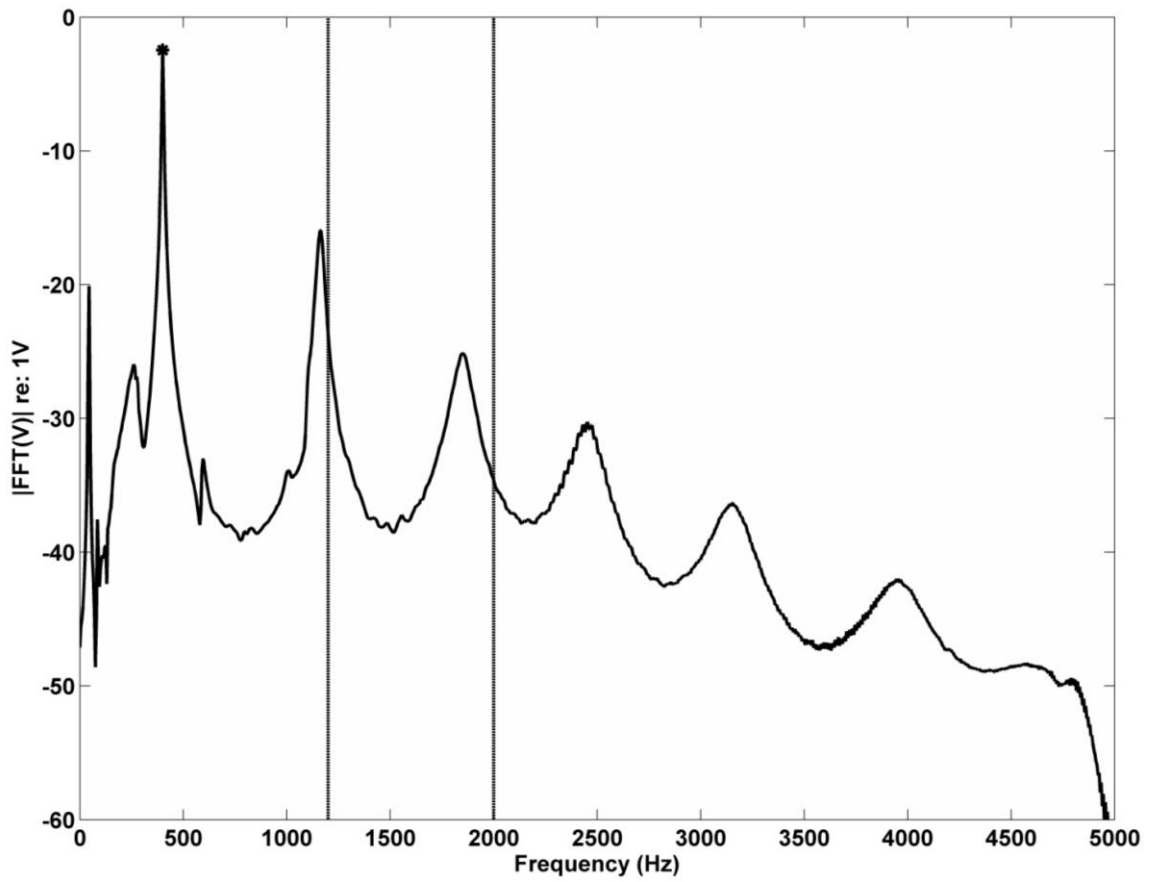


Figure 4.6: Frequency response level versus frequency for the resonator 20 seconds after the approximate moment the tube is first filled with bubbly fluid, driven by five 200 ms linear sweeps from 0-5 kHz

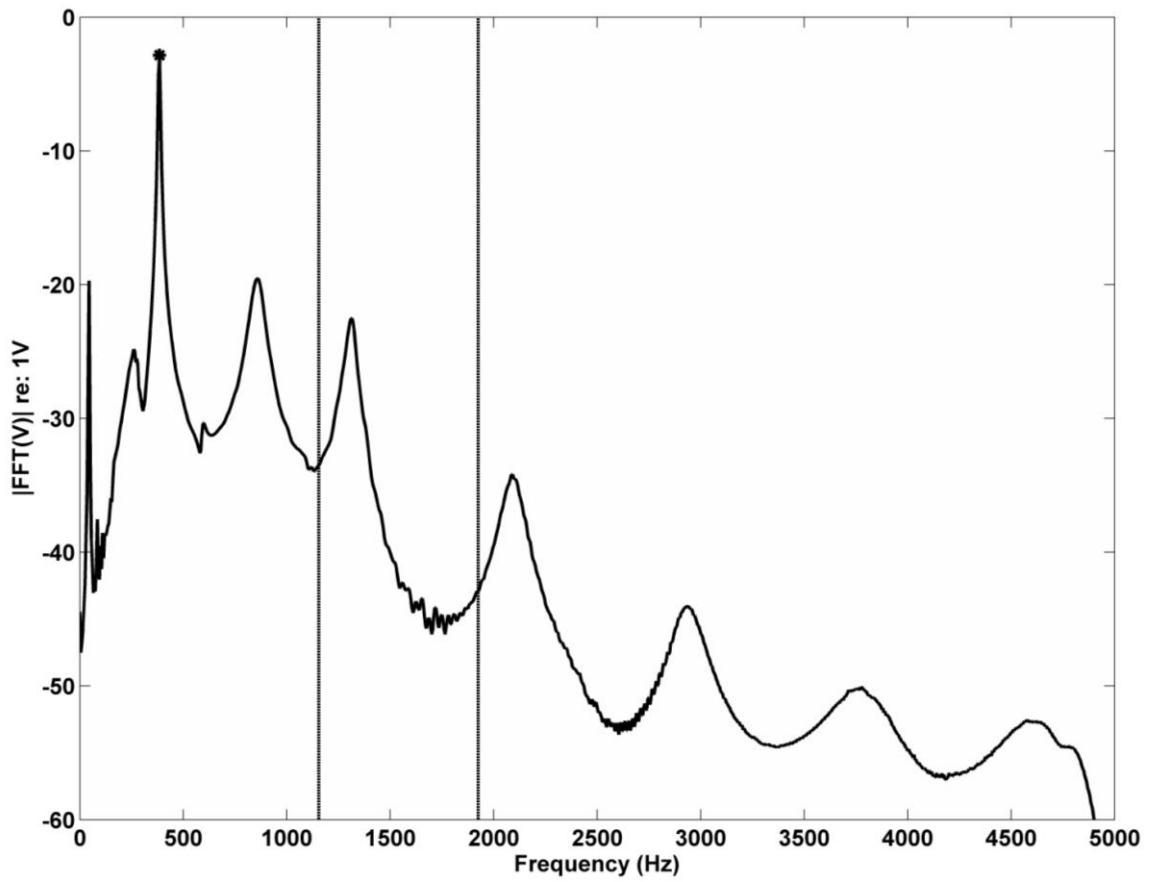


Figure 4.7: Frequency response level versus frequency for the resonator after five minutes of flowing bubbly water, driven by five 200 ms linear sweeps from 0-5 kHz

Next, the air was turned off, and the modal peaks began to spread to higher frequencies, as expected. However, the initial pure water result does not immediately return. The bubbles on the wall still remain and continue to affect the spectrum even though the flow is now bubble-free. Shown below in Figure 4.8 is the frequency response of the resonator after two minutes of flowing clean water with bubbles still attached to the tube walls. Notice that now the frequency regime affected by the bubbles on the wall encompasses the first modal peak for pure water. Next, the tube was struck with a deadblow hammer numerous times and the walls were squeegeed with a piece of curved rubber sheet on a rod. Then, the spectrum is again identical to Figure 4.2.

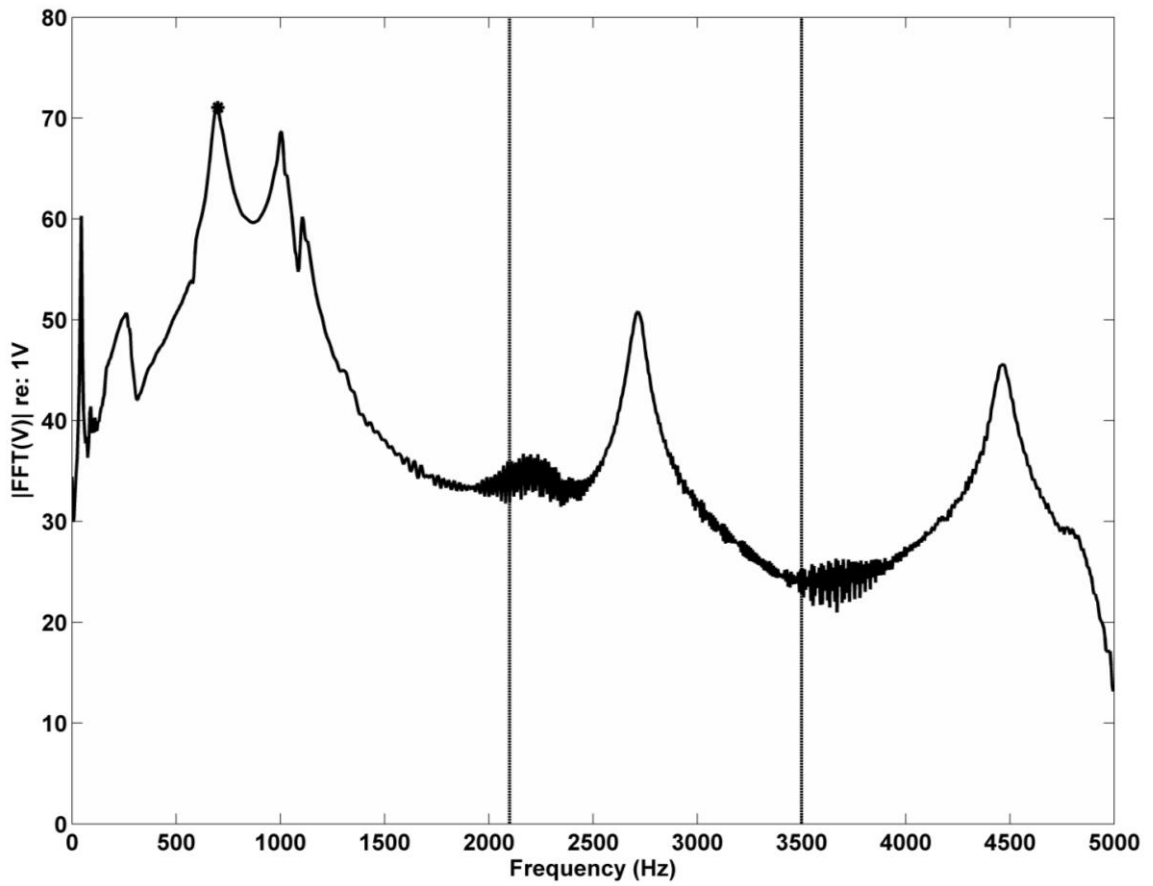


Figure 4.8: Frequency response level versus frequency for the resonator after flowing non-bubbly water for two minutes following a bubbly mixture experiment (bubbles remain on the tube wall), driven by five 200 ms linear frequency sweeps from 0-5 kHz

The test described above was performed for three significantly different air input flow rates (*i.e.* void fractions) that span the capable range of the flowmeter/controller to ensure that the first modal peak always remained robust during the collection of bubbles on the wall. The ‘low’ void fraction (air input rate 1.0 SCCM) was the experiment shown in the above figures. The same phenomena were observed for the higher void fractions as well. The low void fraction experiment was chosen for display since the frequency peak shifts are more easily seen in spectra when the x-axis range is kept constant; at higher void fractions, peaks shift to the left further and more rapidly upon the introduction of air.

The robustness of the first modal peak for bubbly measurements of all void fractions suggests the solution of using only this fundamental modal peak for phase speed measurement. After these tests, only the first modal peak was used for all bubbly mixture experiments.

4.2.2 Bubbly Water Benchmark Experiment

With the information gleaned from the experiments in Section 4.1, the experiments intended to validate the bubbly mixture performance of the instrument were set up and conducted via the arrangement and method described in Chapter 3. Some details will be reiterated for the sake of clarity.

Bubbly water experiments for a range of 26 void fractions were performed. Void fraction variation was achieved by changing the setting on the flowmeter/controller

from between 0.6 and 50 SCCM in varying increments. No fluid was re-circulated to avoid re-circulation of bubbles that would prevent the injected void fraction from being a “known” value. For each measurement, the flowmeter/controller was set to the desired value while the air was diverted to the atmosphere. The flow was turned on and the valve switched to allow air to be forced into the Mott sparger. The system was allowed to flow for two minutes, which is enough time for the tube to be filled six times, in order to allow the bubbling flow to hopefully reach a steady state. Then, a standard resonator measurement (five 200 ms linear frequency sweeps from 0-5 kHz whose response spectra are then averaged) was recorded every 30 seconds for 120 seconds. These five measurements were averaged into a final spectrum after an inspection to ensure the data did not exhibit gross spectral changes over the two minute time period.

In Figure 4.9 below is shown the theoretical sound speed versus void fraction curve, along with the data extracted from the resonator. The resonator measured sound speed is plotted versus the injected void fraction given by the flowmeter/controller and liquid flow rate, that is:

$$\beta_{injected} = \frac{\dot{V}_{gas}}{\dot{V}_{gas} + \dot{V}_{liquid}}, \quad (4.4)$$

where \dot{V}_{gas} is the reading on the flowmeter in SCCM, and \dot{V}_{liquid} is the liquid flow rate, which for the Cole Parmer peristaltic pump at full power is 2300 mL/min; this was the pump and power level used for all experiments.

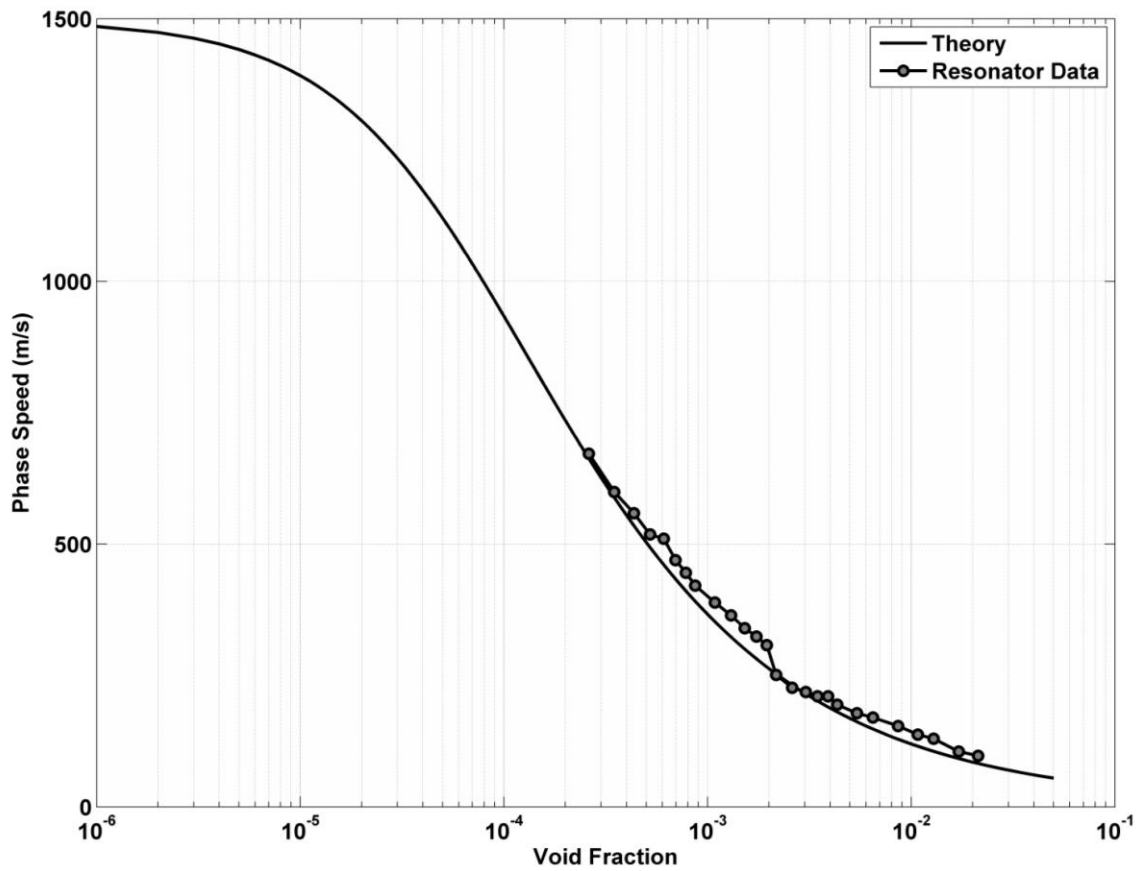


Figure 4.9: Sound speed versus injected void fraction for bubbly water resonator measurements of 26 different air flow rates. The independent variable is derived from measured liquid and gas flow rates via Equation (4.4)

Equation (4.3) is used to calculate the propagated frequency-dependent uncertainty in the phase speed based on the first modal peak due to the uncertainty in the FFT and the column length. Combining Equation (4.2) and Equation (4.4) yields the propagated uncertainty in the injected void fraction, u_β , due to the uncertainty in the volumetric air flow rate and fluid flow rate as follows:

$$u_\beta = \sqrt{\left(\frac{2\dot{V}_{gas} + \dot{V}_{liquid}}{(\dot{V}_{gas} + \dot{V}_{liquid})^2} u_{\dot{V}_{gas}} \right)^2 + \left(\frac{\dot{V}_{gas}}{(\dot{V}_{gas} + \dot{V}_{liquid})^2} u_{\dot{V}_{liquid}} \right)^2}, \quad (4.5)$$

where $u_{\dot{V}_{gas}}$ and $u_{\dot{V}_{liquid}}$ are the uncertainties in the gas and fluid flow rates, respectively. Applying both phase speed and void fraction uncertainties to the data and magnifying the region of interest results in Figure 4.10 below. One can see that in general, the data provides an overestimate of the void fraction. The deviation of 80 percent of the data from the theoretical curve cannot be accounted for via the uncertainty analysis discussed above. Therefore, considerations into possible causes for this deviation needed examination.

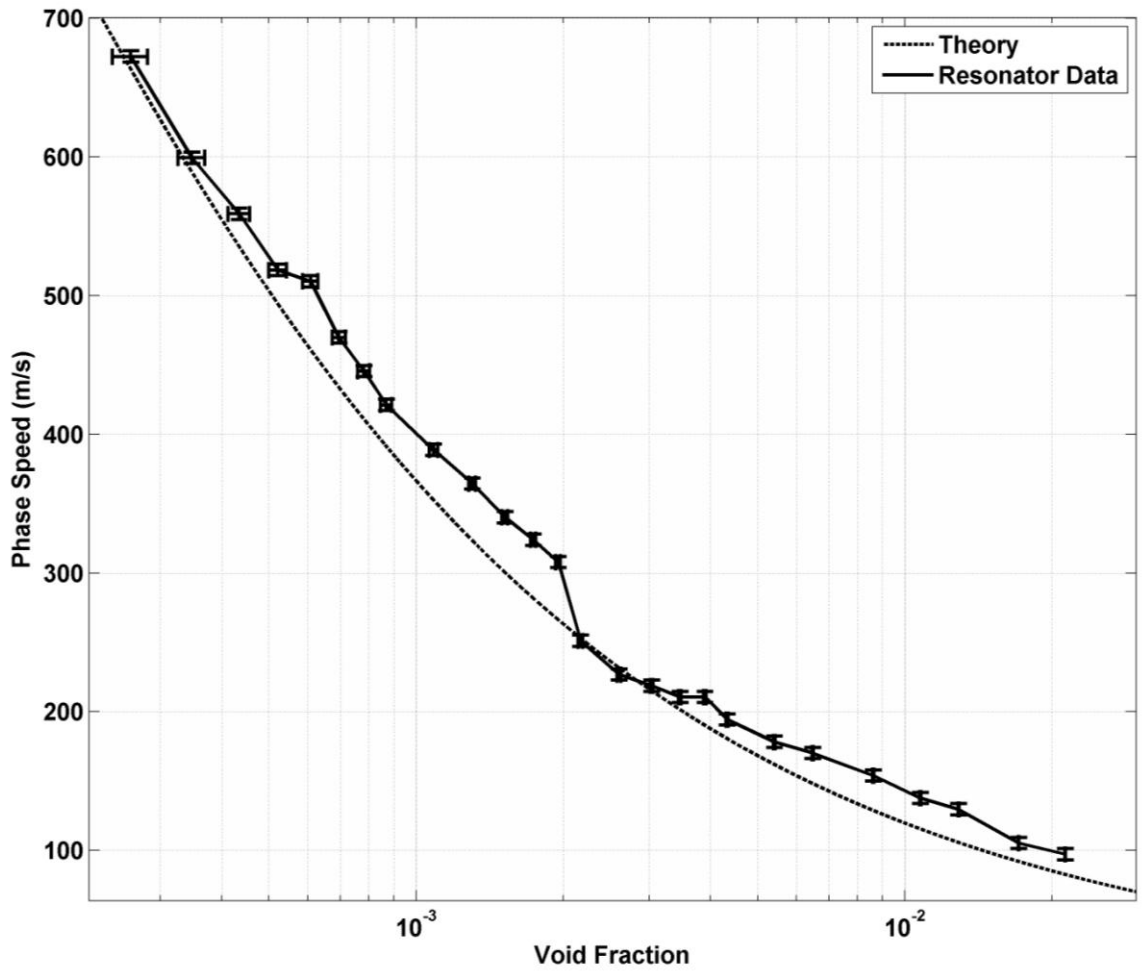


Figure 4.10: Sound speed versus injected void fraction for bubbly water resonator measurements of 26 different air flow rates. The independent variable is based upon liquid and gas flow rates via Equation (4.4)

4.2.3 Bubble Rise Velocity Correction and Results

Equation (4.4) assumes that the gas and liquid travel as one. This is true as the bubbly liquid leaves the Mott unit, heading towards the resonator. However, as the bubbly fluid enters the resonator, all gas bubbles will be subject to the effects of buoyancy. Bubbles will have a rise velocity relative to the fluid that can be significant depending on fluid flow velocity and bubble radius; this effect can be accounted for with knowledge of bubble radius. The rise velocity of a bubble, v_{bubble} , can be described by a simple Stokes' model that balances the buoyancy force and drag force acting on the bubble as it rises through the fluid, described by

$$v_{bubble} = \frac{2(\rho_{air} - \rho_{water})gR^2}{9\mu}, \quad (4.6)$$

where the dynamic viscosity μ is taken to be 1E-3 Pa*s. This model assumes a no-slip boundary condition applicable to rigid spheres. Since bubbles can experience internal re-circulation flows, the actual drag could be reduced and the predicted rise velocity slightly greater than that given by Equation (4.6).

The bubble rise time through the resonator tube is given by

$$t = \frac{l_{tube}}{v_{bubble}}, \quad (4.7)$$

where it is assumed that the bubble radius is constant, that is, bubble dissolution and changes in hydrostatic pressure are ignored. Using the method described by Nicholas *et al* [61], the void fraction is given by

$$\beta_{resonator} = \frac{t\dot{v}}{V_{tube}} = \frac{9l\mu\dot{v}}{2V_{tube}(\rho_{water} - \rho_{air})gR^2}, \quad (4.8)$$

where \dot{v} is the injected air flow rate and V_{tube} is the resonator tube volume. The value of R used in practice in this case is the root mean square radius gathered from the bubble image processing algorithm described in Section 3.4.6. Since the void fraction is dependent on the square of the radius, it is sensible to weight the averaging of imaged bubble radii accordingly. Below in Figure 4.11 and Figure 4.12 are shown the bubbly image with circles denoting the bubbles chosen by the algorithm and the histogram of bubble radii, respectively, for a low void fraction (injected air flow rate of 0.6 SCCM, or rise-time-corrected VF = 1.92E-4). The same are shown in Figure 4.13 and Figure 4.14 for a medium void fraction (injected air flow rate of 5 SCCM, or rise-time-corrected VF = 1.37E-3), and in Figure 4.15 and Figure 4.16 for a high void fraction (injected air flow rate of 50 SCCM, or rise-time-corrected VF = 1.40E-2). Not only are these three void fractions approximately an order of magnitude apart each, they also span the entire usable range of the flowmeter/controller. For all images the scale is in pixels, and the calibration applied sets one pixel equal to 14.4 μm . This calibration was calculated by measuring the inner diameter of the flow cell with calipers, then dividing that

dimension by the number of pixels across the flow cell as seen in the captured images.

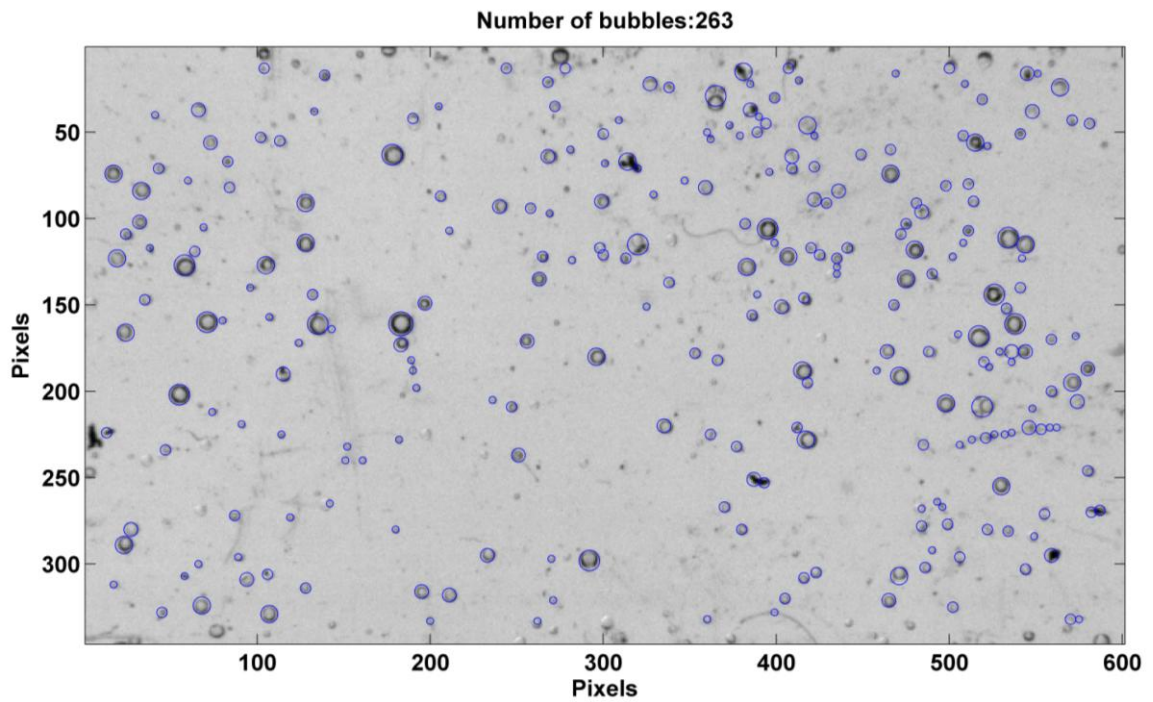


Figure 4.11: Bubbly image captured for an air flow rate of 0.6 SCCM; this corresponds to a corrected injected void fraction of $1.92E-4$. Blue circles indicate bubbles chosen via the image processing algorithm.

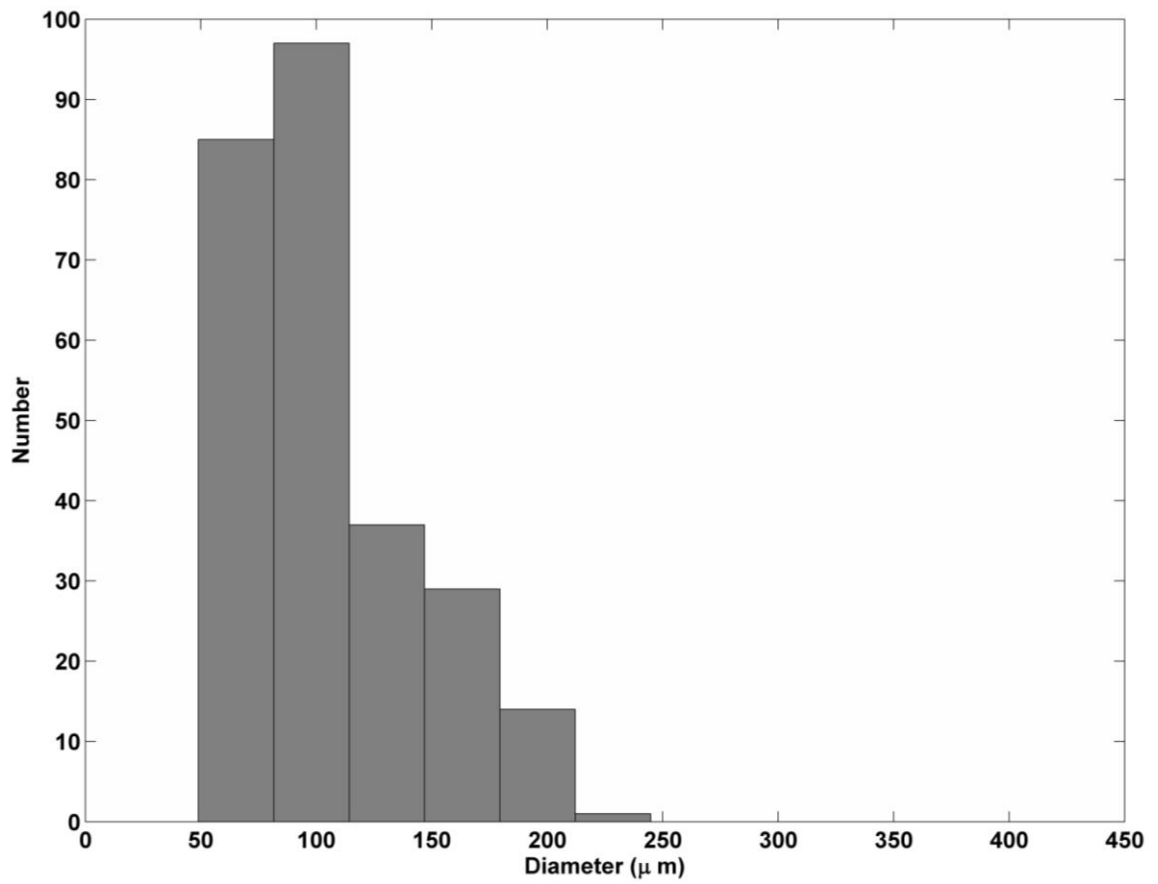


Figure 4.12: Histogram of bubble diameters corresponding to Figure 4.11. Diameters were calculated using a calibration of 14.4 microns per pixel.

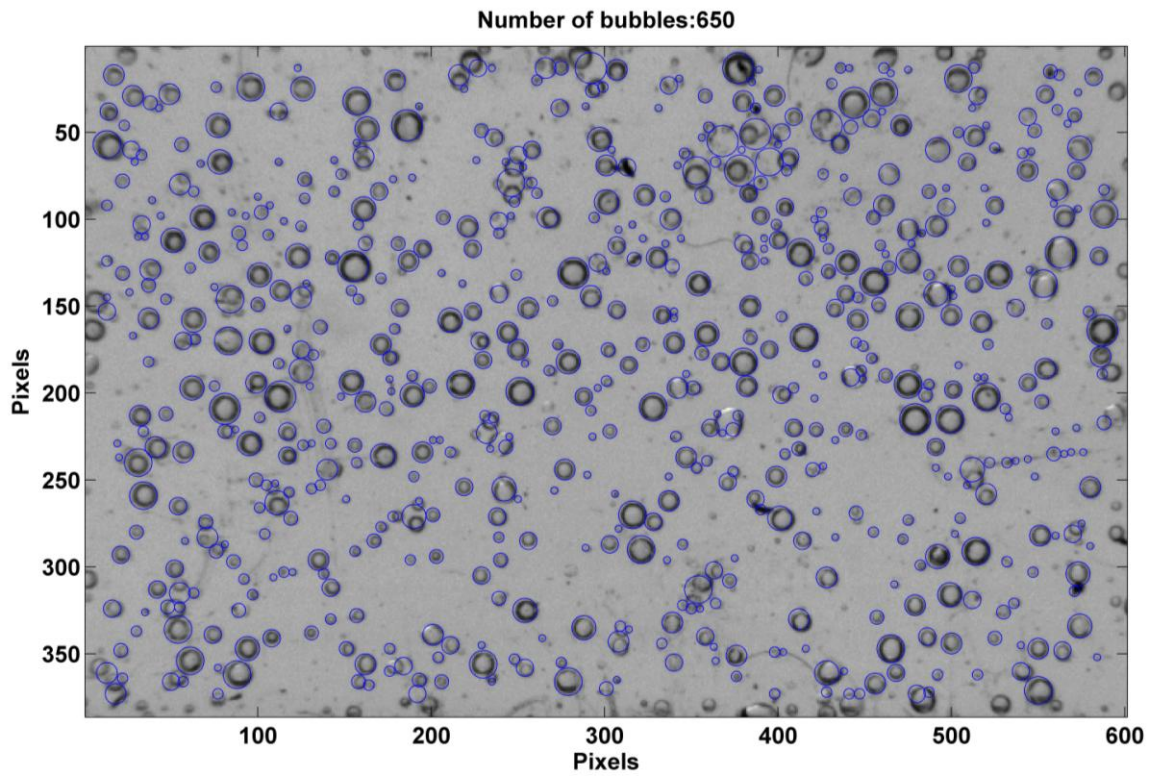


Figure 4.13:Bubbly image captured for an air flow rate of 5.0 SCCM; this corresponds to a corrected injected void fraction of $1.37E-3$. Blue circles indicate bubbles chosen via the image processing algorithm.

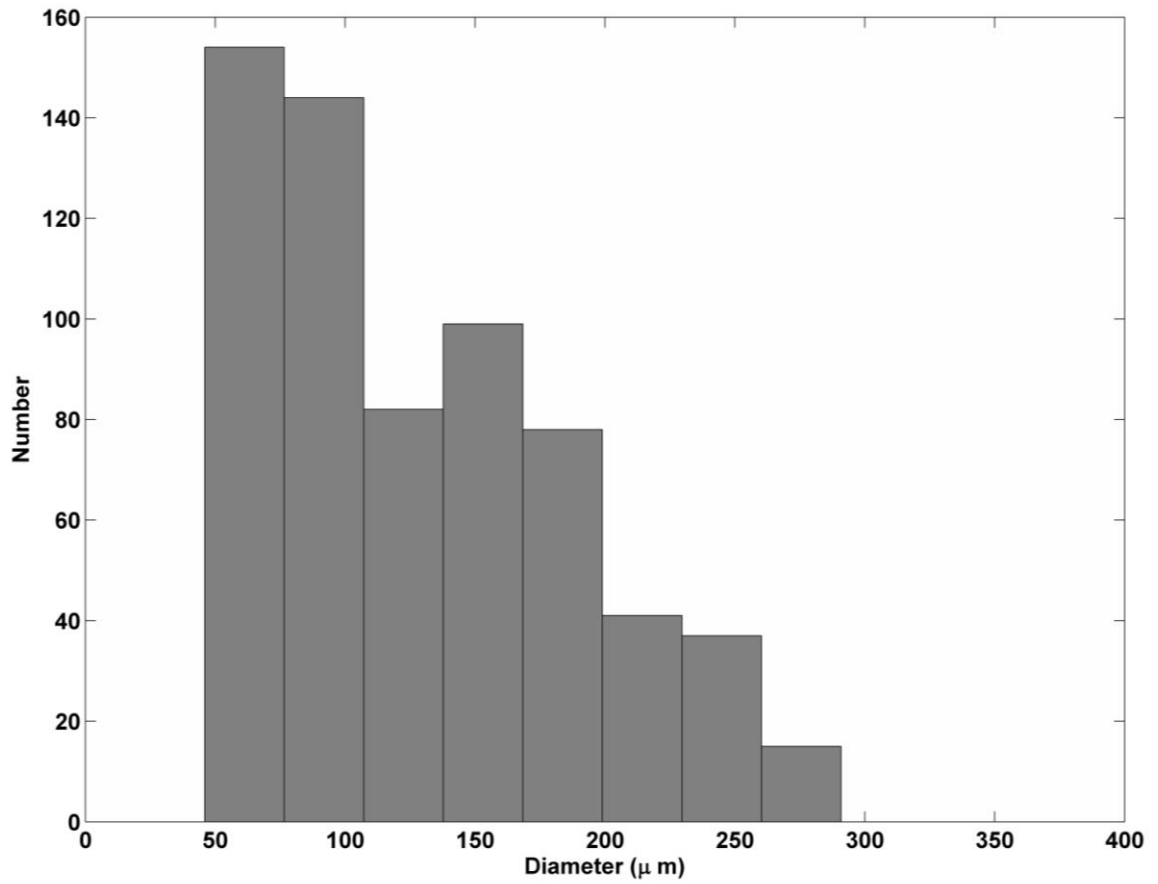


Figure 4.14: Histogram of bubble diameters corresponding to Figure 4.13. Diameters were calculated using a calibration of 14.4 microns per pixel.

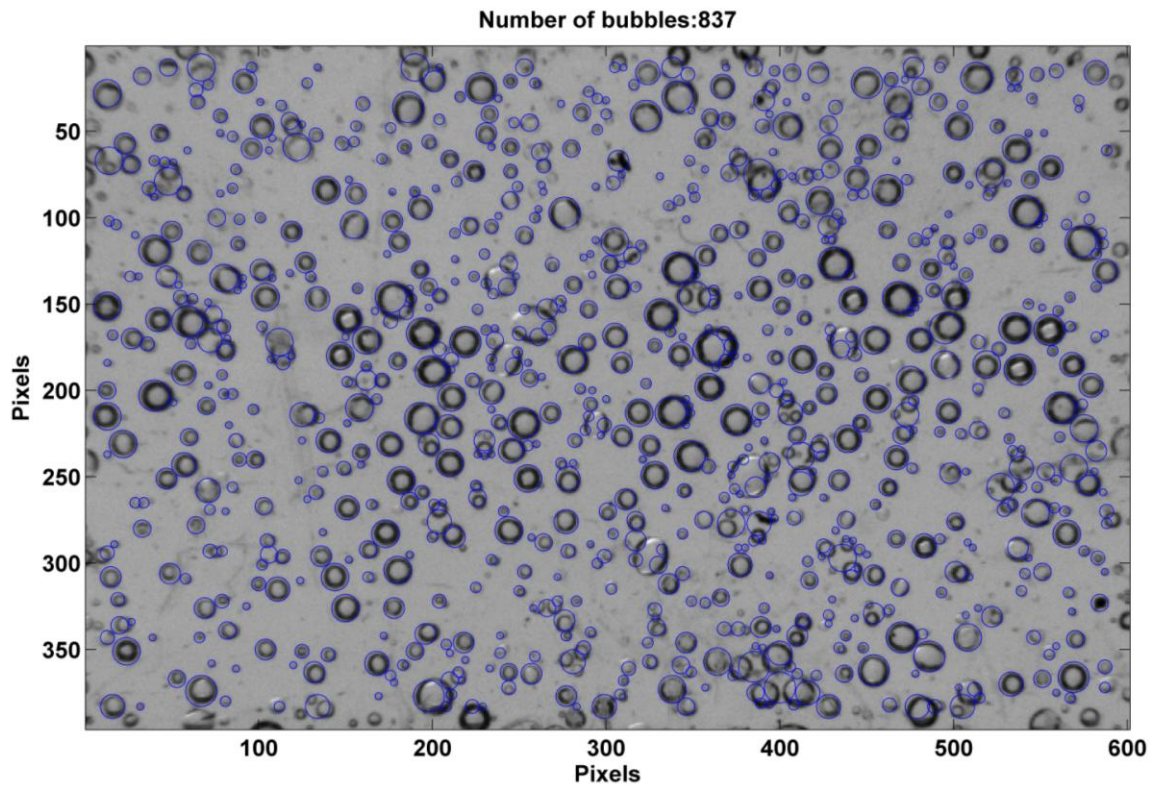


Figure 4.15: Bubbly image captured for an air flow rate of 50 SCCM; this corresponds to a corrected injected void fraction of $1.40E-2$. Blue circles indicate bubbles chosen via the image processing algorithm.

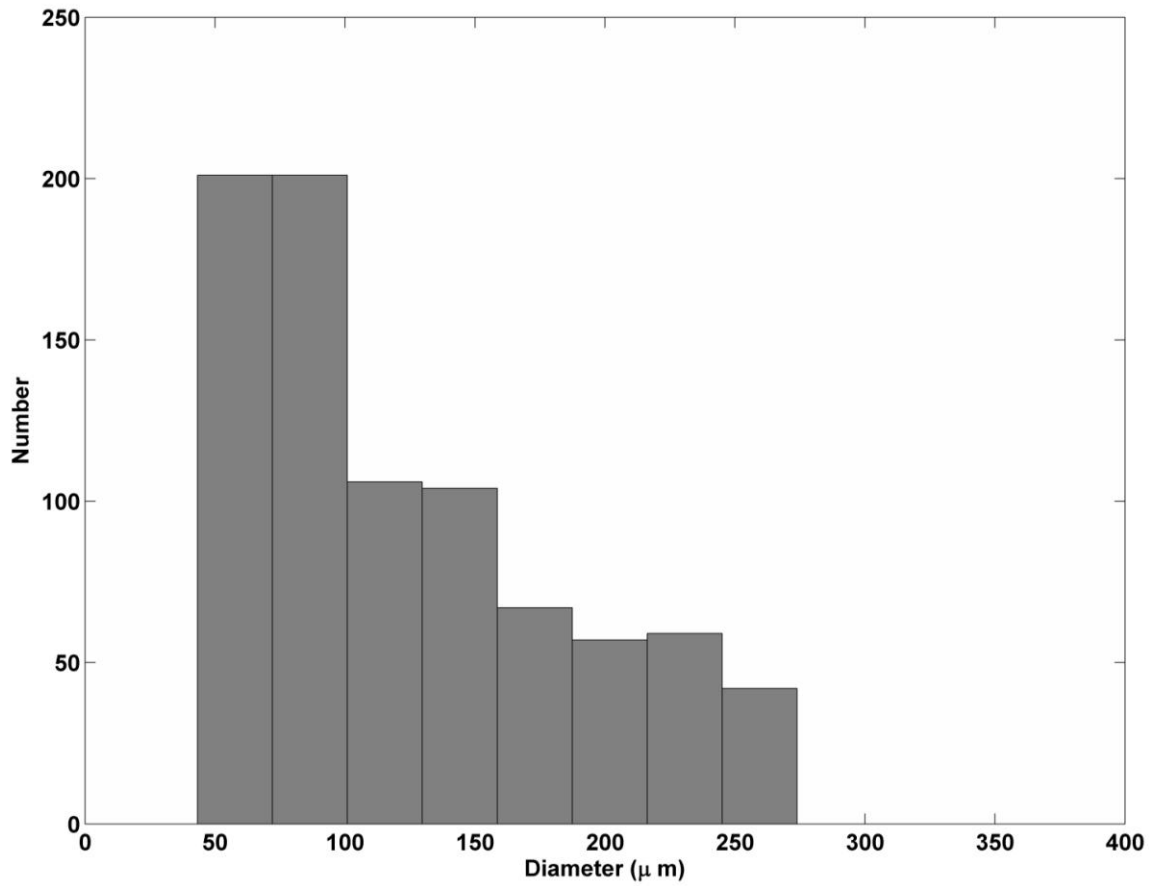


Figure 4.16: Histogram of bubble diameters corresponding to Figure 4.15. Diameters were calculated using a calibration of 14.4 microns per pixel.

Using the root mean square bubble radius from the images allowed calculation of a rise-velocity-corrected void fraction via Equation (4.8). Shown below in Figure 4.17 is the resonator measured phase speed versus the rise-velocity-corrected void fraction. One can qualitatively see that unlike Figure 4.10, the measurements are now an underestimate of the void fraction with respect to the theoretical curve. In order to determine if this is of concern, the uncertainties in measured quantities must be considered.

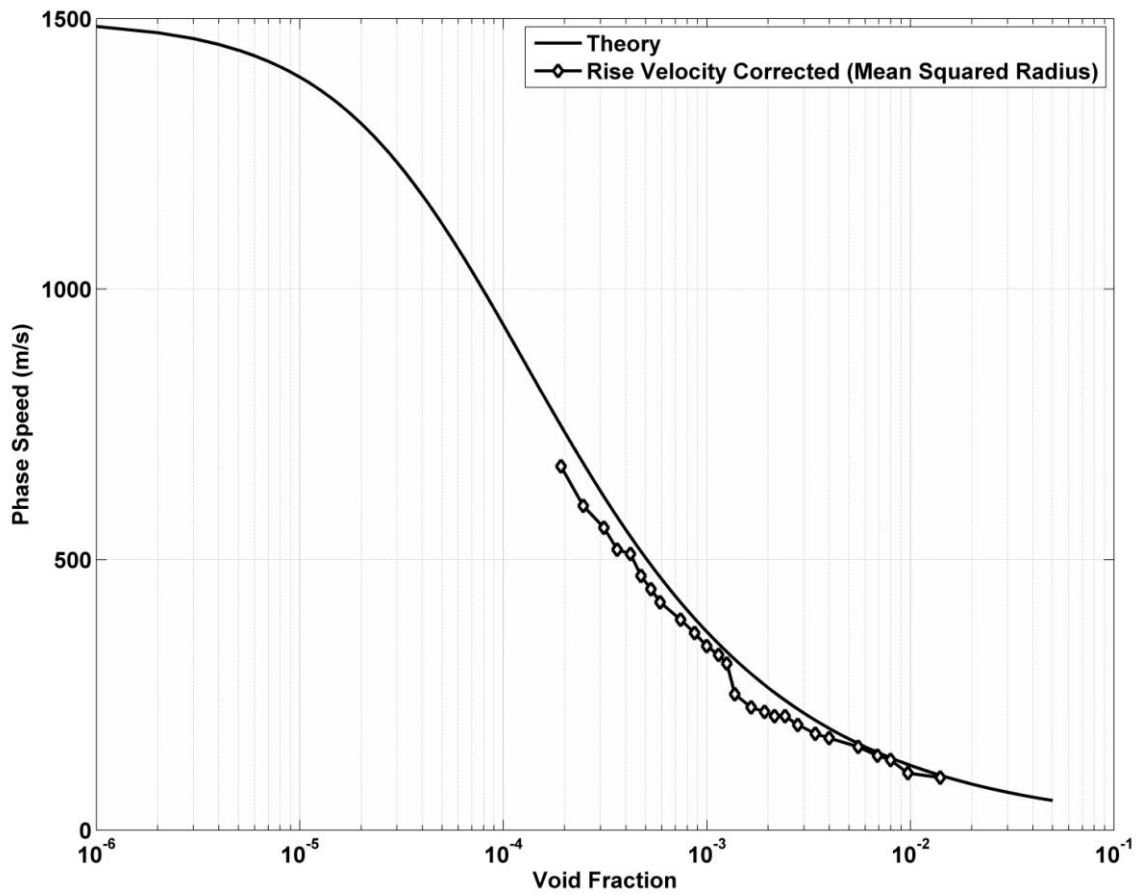


Figure 4.17: Sound speed versus injected void fraction for bubbly water resonator measurements of 26 different air flow rates. The independent variable is based upon a rise velocity and tube volume.

The uncertainty in the phase speed remains identical to the values shown in the previous Section. In order to calculate the uncertainty in the void fraction, associated uncertainties must be propagated through Equation (4.8). These uncertainties are in the tube length, the volumetric air flow rate, and the mean squared bubble radius measured via the imaging system. However, examining Equation (4.8) indicates that the length of the column actually cancels out since it is part of the tube volume in the denominator. The tube diameter was provided with a high enough precision by the machinist for its uncertainty to be negligible. Thus, applying Equation (4.2) to Equation (4.8) yields the expression for the uncertainty in the void fraction,

$$u_{\beta} = \sqrt{\left(\frac{9\mu l}{(60s) * 2V_{tube} (\rho_{water} - \rho_{air}) g R_{rms}^2} u_{\dot{V}_{gas}} \right)^2 + \left(\frac{-9\mu l \dot{V}_{gas}}{(60s) * 2V_{tube} (\rho_{water} - \rho_{air}) g R_{rms}^3} u_R \right)^2} \quad (4.9)$$

where $u_{\dot{V}_{gas}}$ and u_R are the uncertainties in the air flow rate and imaged bubble radius, respectively, and R_{rms} is the root mean square bubble radius chosen by the bubbly image processing algorithm. Applying both phase speed and void fraction uncertainties to the data and magnifying the region of interest results in Figure 4.18 below.

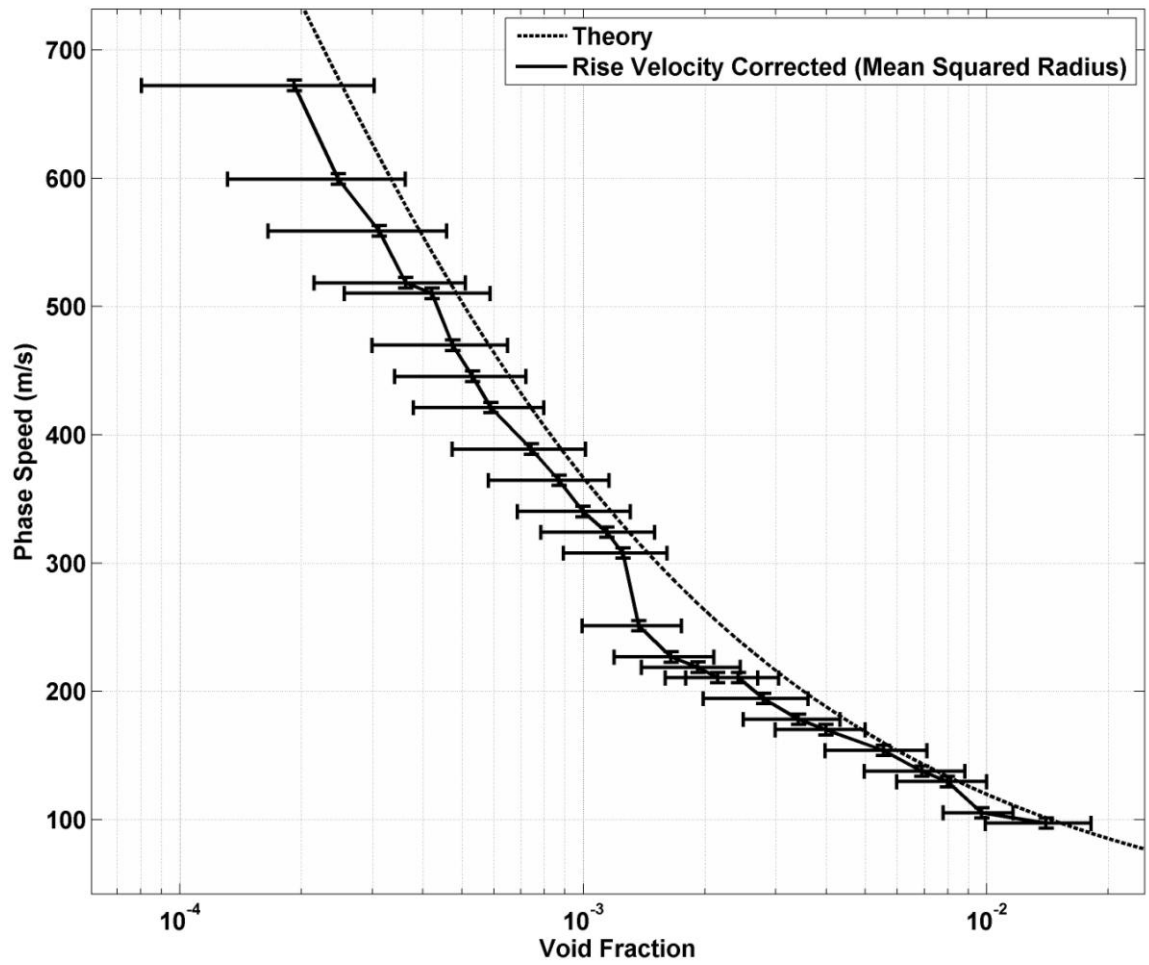


Figure 4.18: Sound speed versus injected void fraction for bubbly water resonator measurements of 26 different air flow rates. The independent variable is based upon a rise velocity and tube volume.

As mentioned before, the data is now, on average, an underestimate compared to the theoretical curve. The propagated uncertainties in the measurements allow 80% of the data bounds to encompass the theory. Although the uncertainties in this data are larger than the data described in Section 4.2.2, this data includes a correction for an effect that certainly occurs and must be considered. Since most of the data coincides with the theory when the bounds of uncertainty are taken into account, agreement can be considered very good.

One cause for underestimate of the mean value of the range from the theory is believed to be a bias in the image processing technique. The image processing requires a thresholding to be performed at one stage, which inherently causes error. Additionally, when there are caustics in the bubbly image, these can cause the boundaries of some bubbles to be incomplete circles; in order to correct for this, a dilation followed by an erosion is necessary. This can cause some bubbles to join with others, which results in a larger bubble mask to fit into the inner region of a group of bubbles, biasing the result towards a larger bubble radius. Also, imperfections in the acrylic flow cell material forced thresholding to not include some smaller bubbles, again biasing the distribution towards larger radii. Additionally, low resolution caused some small bubbles to be missed. Thus, there is an inherent bias in the image processing to yield a larger root mean square radius than is truly present in the resonator, which could lower the rise-velocity-corrected value of the injected 'known' void fraction significantly, since it is dependent on the

square of the RMS radius value. This effect could explain the average underestimate of the data.

Other considerations mentioned previously could also play a role, albeit more minor, which will be briefly presented here. The change in hydrostatic pressure over the height of the tube would serve to increase the size of the bubble as it rose, contributing again to account for the discrepancy from theory. This change is simply given by ρgh , which gives a total pressure change of about 4% from the bottom of the tube to the top (where the pressure is ambient, 1 atmosphere). This would yield an average change to the void fraction of about 2%, which is not significant compared to the error bars in Figure 4.18 which can be as great as 25%.

The applicability of Equation (4.6) is dependent on the Reynolds number of the flow and the bubble radius. Depending on bubble size and flow velocity, there is a tangential component of the velocity near the gas-liquid interface which causes an increase in the gas bubble rise velocity that can be very significant. This can increase velocities on the order of 50% for some bubbles and flows [62]. For the Reynolds numbers present in the current work (<10) and the bubble size distributions present, the total correction to be made to the void fraction due to the bubbles not rising as rigid spheres is predicted by [62] to be roughly 10% at most, which is of a larger but similar order to the hydrostatic pressure correction. Again, this effect would tend to decrease the discrepancy from theory.

Another consideration is the dissolution of gas into the fluid over the time scale of an experiment. Since bubbles were not re-circulated, their lifetime is essentially the time of travel through the tube. This time would be 20 second or less, depending on the bubble size. It has been shown thoroughly in the literature that the dissolution rate can be highly dependent on the surrounding fluid velocity [62, 63], which in this case is equal to the bubble rise velocity. Also, the concentration of gas in the liquid is an important parameter. Spring water from a five gallon jug was used that had been open to air for two hours before experiments were begun; a conservative estimate of 2/3 saturation was used in calculations. Based on a model developed in [63], bubbles on the order of 10 micron radius would dissolve completely in the tube rise time, whereas bubbles with 100 micron radii would take hundreds of seconds to dissolve; over the time frame of rising through the tube they would simply be decreased in size by about 5% during the tube rise time. Since all distributions in this effort were found to be weighted towards smaller bubbles, many of which would disappear via dissolution, the overall result of this effect is again a shift in the correction term in the direction of accounting for the discrepancy from theory. Furthermore, the fluid flow velocity with respect to the bubble (in this case due to the bubble rising) encourages this effect. The smaller bubbles would dissolve more quickly, whereas the increased dissolution rate of the larger bubbles is offset by their far decreased rise time through the tube. Detailed knowledge of actual gas concentrations, bubbles sizes, and distributions would be required for

accurate estimate of the effect of dissolution phenomena; further experiments would be necessary.

Regardless of all corrections significant or insignificant, both the uncorrected data and corrected data provide void fraction measurements with high enough accuracy and precision to determine a narrow void fraction range ideal for mitigation of cavitation damage in the SNS mercury target. This will be achieved via the testing of various targets under different bubbly flow conditions and investigating the damage results to find the optimal microbubble injection parameters. The discrepancies in results from theory during validation are truly believed to be experimental variations that surfaced in light of the resonator being a precise and accurate “gold standard” for measuring void fraction of bubbly mixtures.

Chapter 5

5 Conclusion and Path Forward

This Section will recapitulate the findings of the work discussed in this publication, as well as discuss the future experiments to be conducted and possible modifications to improve performance.

The Boston University acoustic resonator, as designed and constructed, is a both accurate and precise instrument that can measure the void fraction of two-phase flows using the standing wave sound speed measurement technique. The device meets or exceeds all of the design constraints set forth in the proposal document, as well as provides additional features for performance enhancement, ease of use, and modularity.

In order to perform extensive tests with mercury, the resonator has been sent to the ORNL SNS facility; SNS has the capability to easily handle toxic mercury without

restriction. This will prove extremely useful when the device must be disassembled or modified.

The device can be arranged or modified for various experimental configurations. Since mercury has an acoustic impedance that is over an order of magnitude larger than that of water, the non-ideality of boundary conditions can become more prominent. Initial tests with pure mercury and the 1" thick plate indicate that the method of experiments will be successful, and further stressed the importance of the boundary condition. Acoustic standing waves were certainly present, but the frequency of the modal peaks did not match the quarter-wavelength or half-wavelength theory; the boundary condition acts dispersively since the impedance mismatch is not extremely large. Because of this, it is anticipated that the thin plate, will be a better option for the bottom boundary condition in order to provide an acoustic pressure release, as mentioned previously. However, other modifications may provide better performance. The use of a rigid stainless steel piston mounted to a baffle on the bottom of the tube that can be driven mechanically from below can provide very close to a true velocity source. A rigid piston that fills the entire tube diameter and physically drives the fluid column is a very efficient way of creating pressure perturbations to propagate plane wave acoustics and set up standing waves; this has been observed experimentally by many, including Wilson [38]. This arrangement may be an excellent choice for mercury experiments. Furthermore, this end condition will result in odd-integer multiples of quarter-wavelength modes,

as did this rigid plate in water; an added benefit of this is that these modes reduce the fundamental modal frequency by a factor of two when compared to half-wavelength modes, which increases the acceptable bubble radius and void fraction.

The dimensions of the resonator could also be scaled or changed depending on experimental demands. A longer or shorter tube could change the frequency range of interest or acceptable bubble radius. Different driving or end conditions could optimize for various types of fluids or driving requirements. Additional instrumentation could be added to the assembly to probe other desired parameters; one possibility is a passive hydrophone near the bubbler unit to listen to acoustic noise emission for purposes of determining the upper and lower bounds of the bubble size distribution.

In conclusion, the resonator is a precise and accurate device for two-phase flow diagnostics. Not only does it succeed in meeting its design requirements, but it can be modified easily to accommodate other experiments. The unit or one like it could also be of interest for various other applications, such as oceanic acoustic research, diagnostics in the food and beverage field, or industrial flow diagnostic applications.

Appendix A

A Engineering Drawings

This Section contains engineering drawings of the individual resonator components as machined by L&M Machine of Everett, MA. Note that the thin plate for use with mercury is shown, not the thick plate used with water.

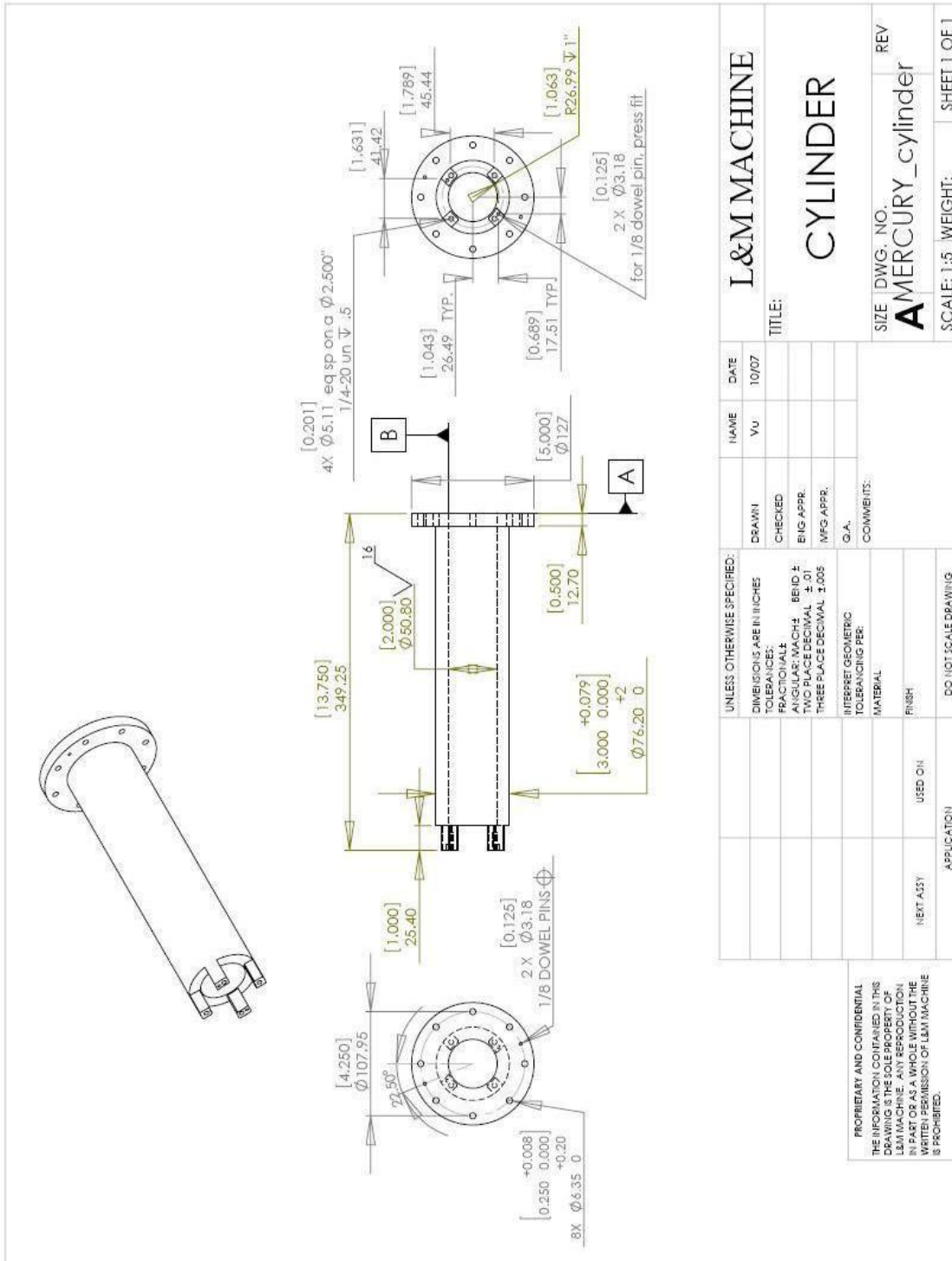


Figure A.1: Engineering drawing of the main resonator tube

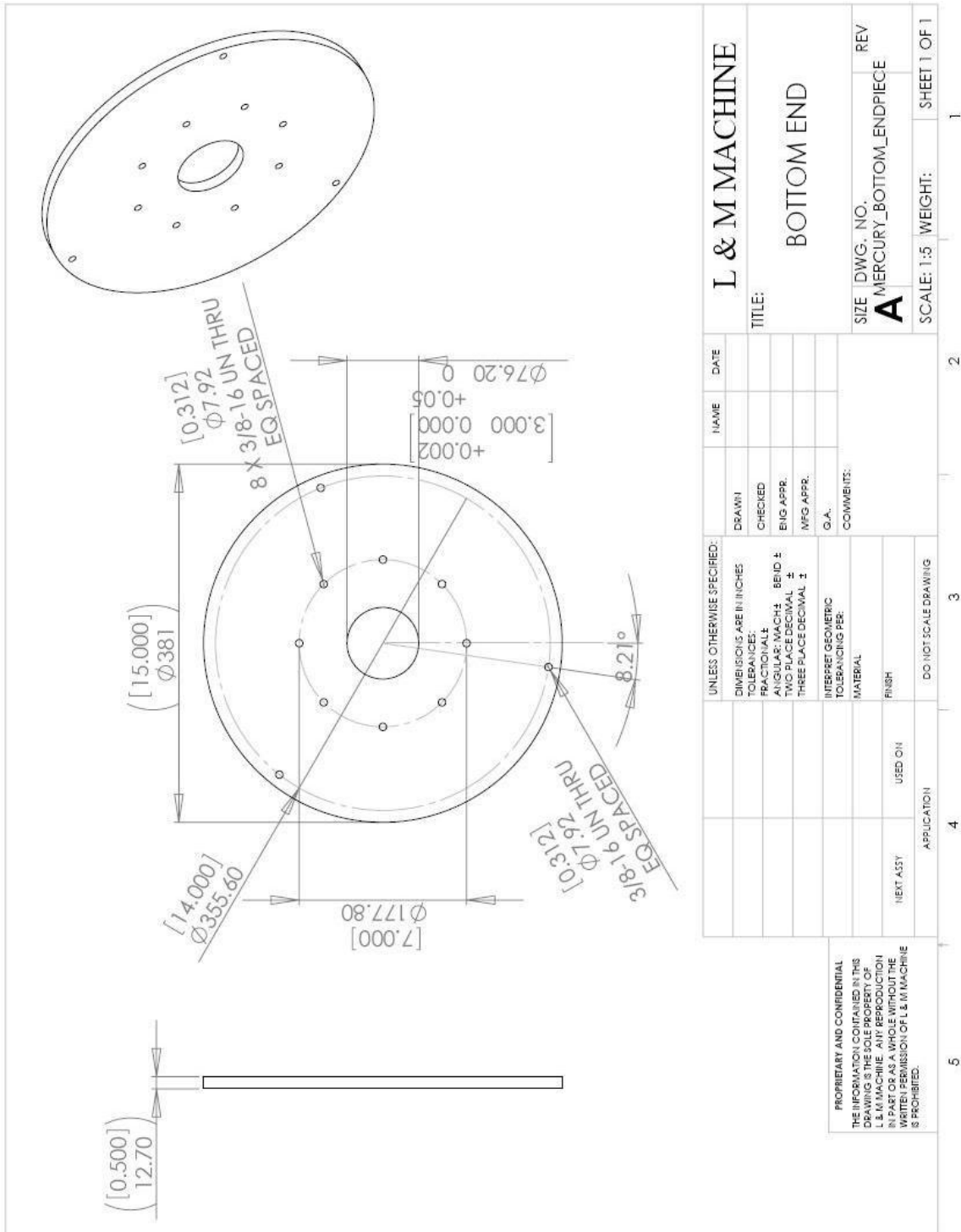


Figure A.2: Engineering drawing of the base support plate

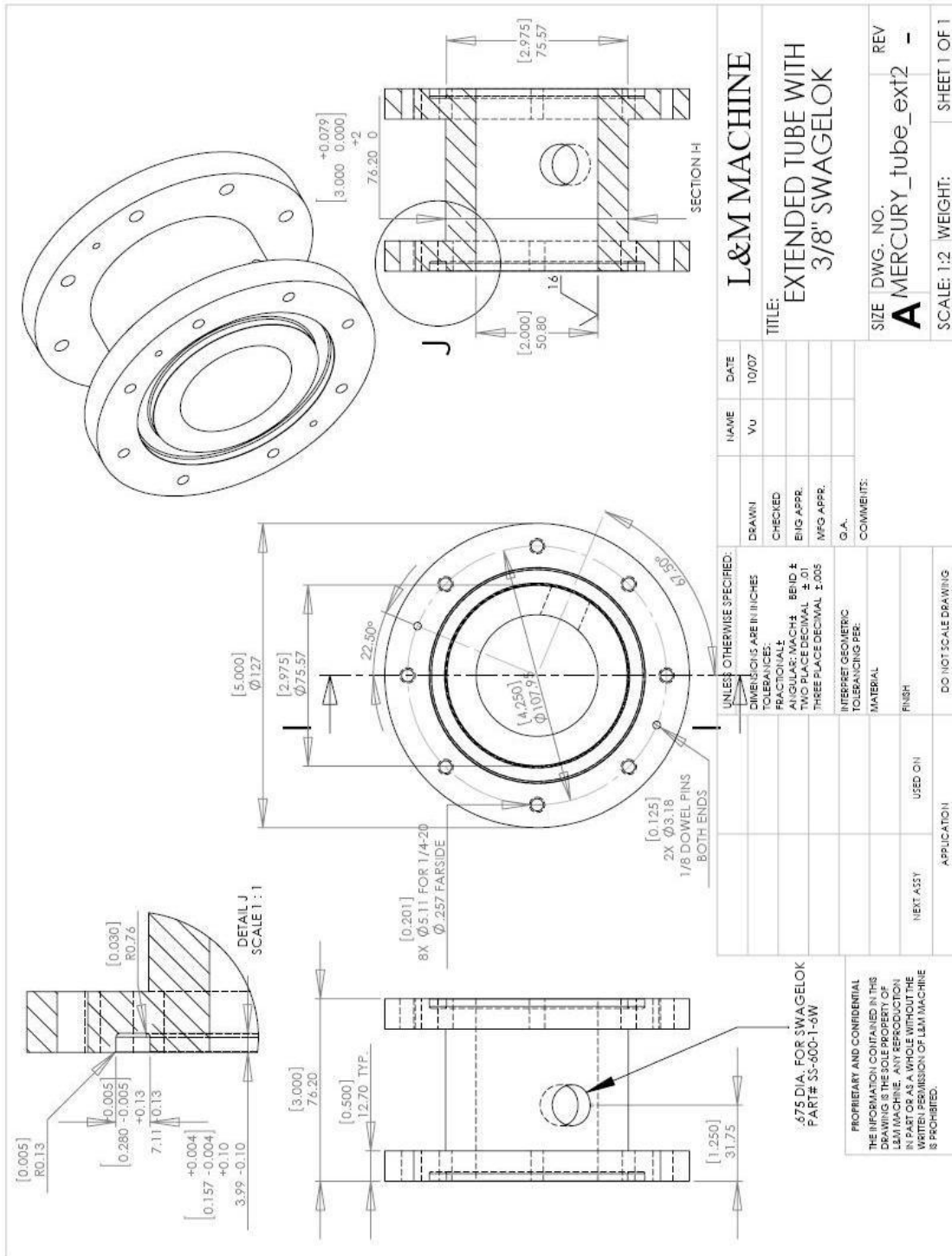


Figure A.3: Engineering drawing of the inlet section

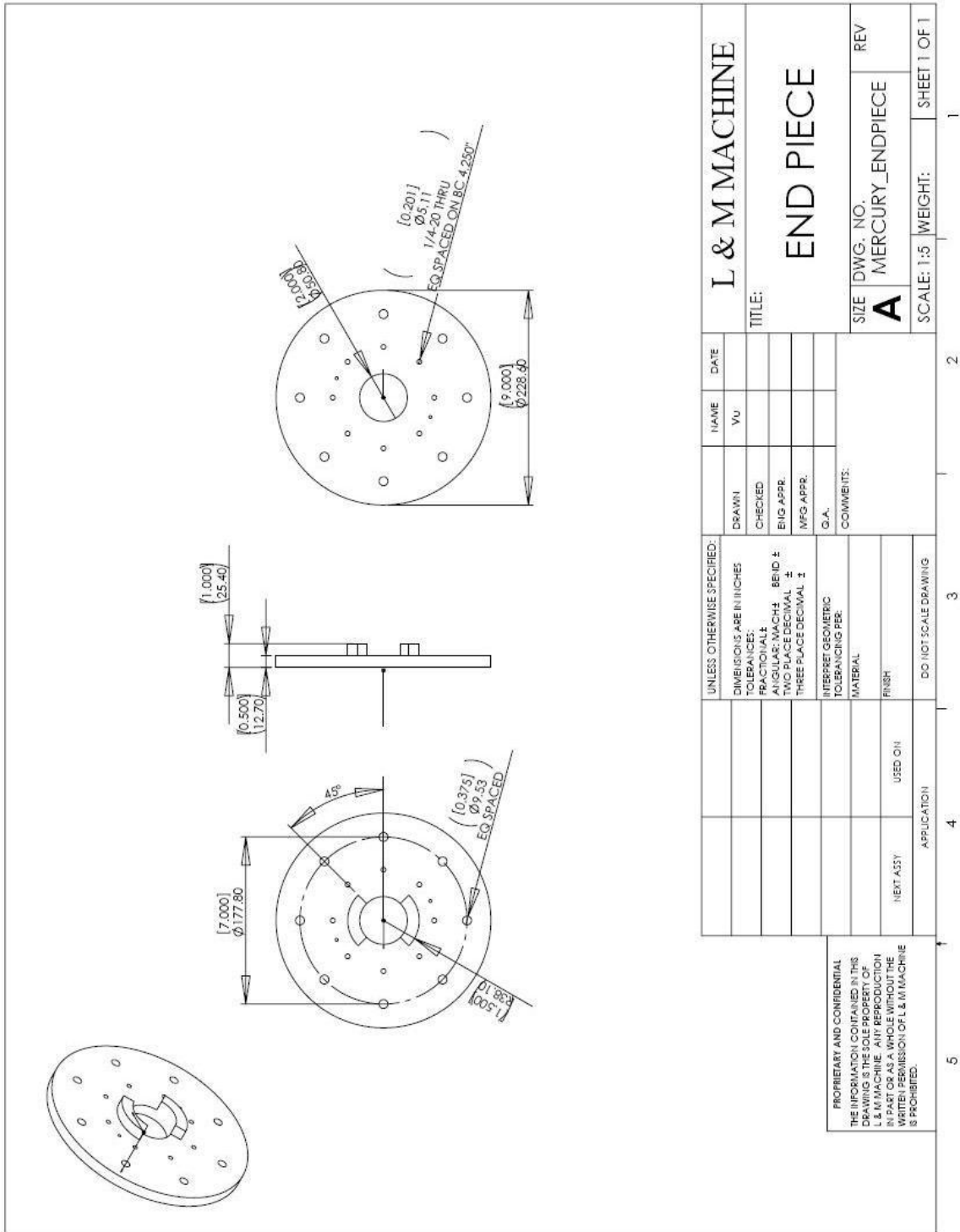


Figure A.4: Engineering drawing of the intermediate support plate

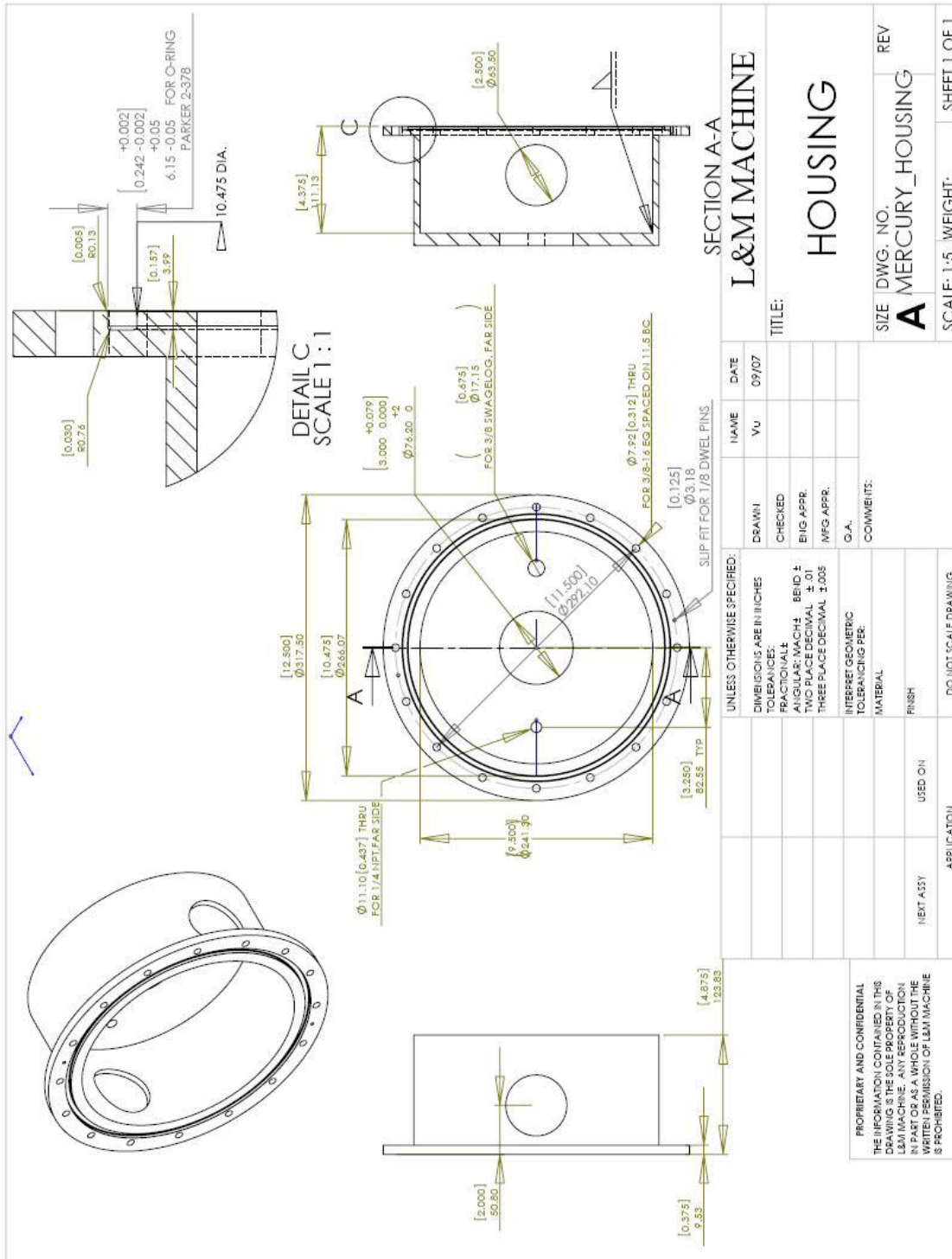


Figure A.5: Engineering drawing of the spillover reservoir

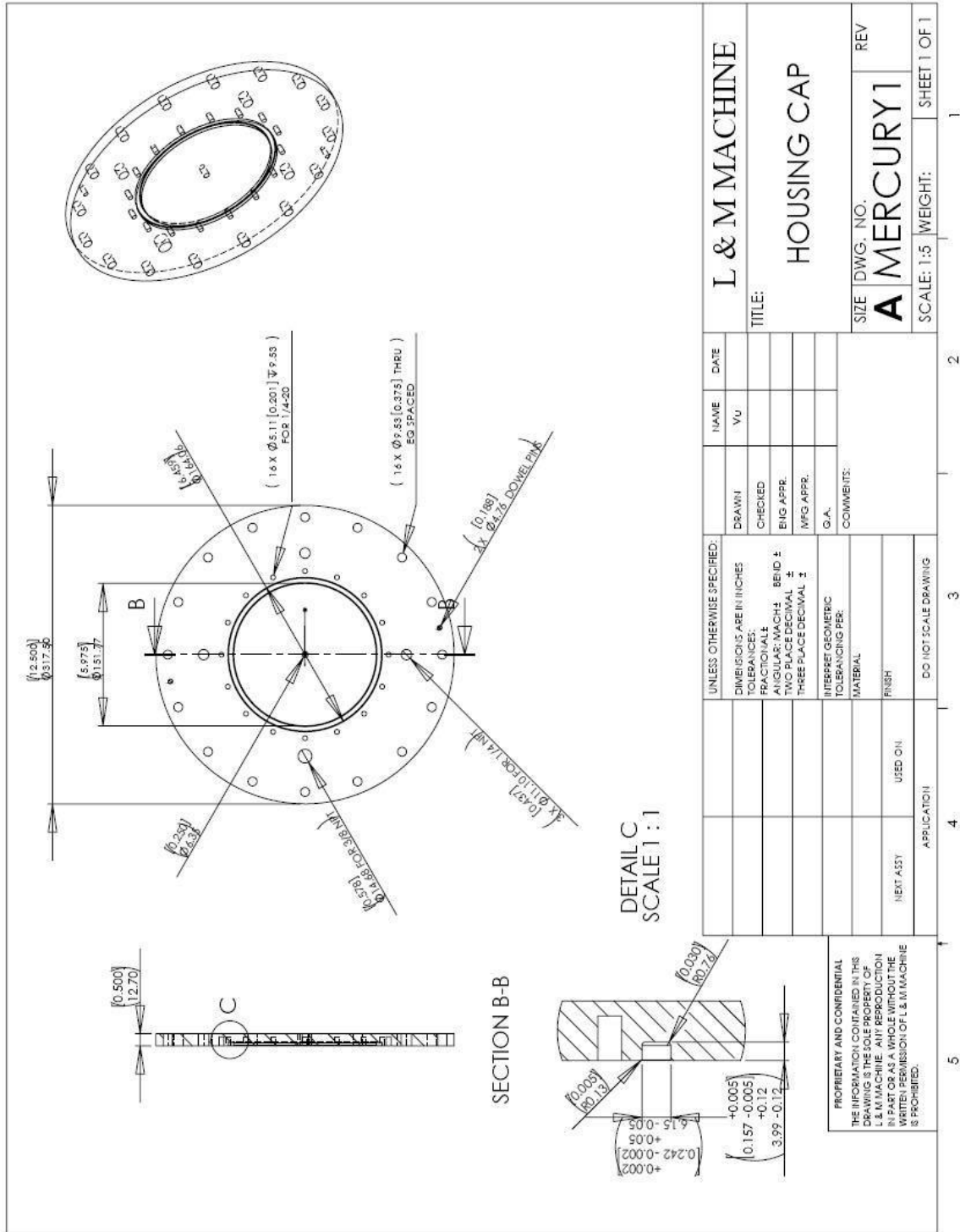


Figure A.6: Engineering drawing of the reservoir lid

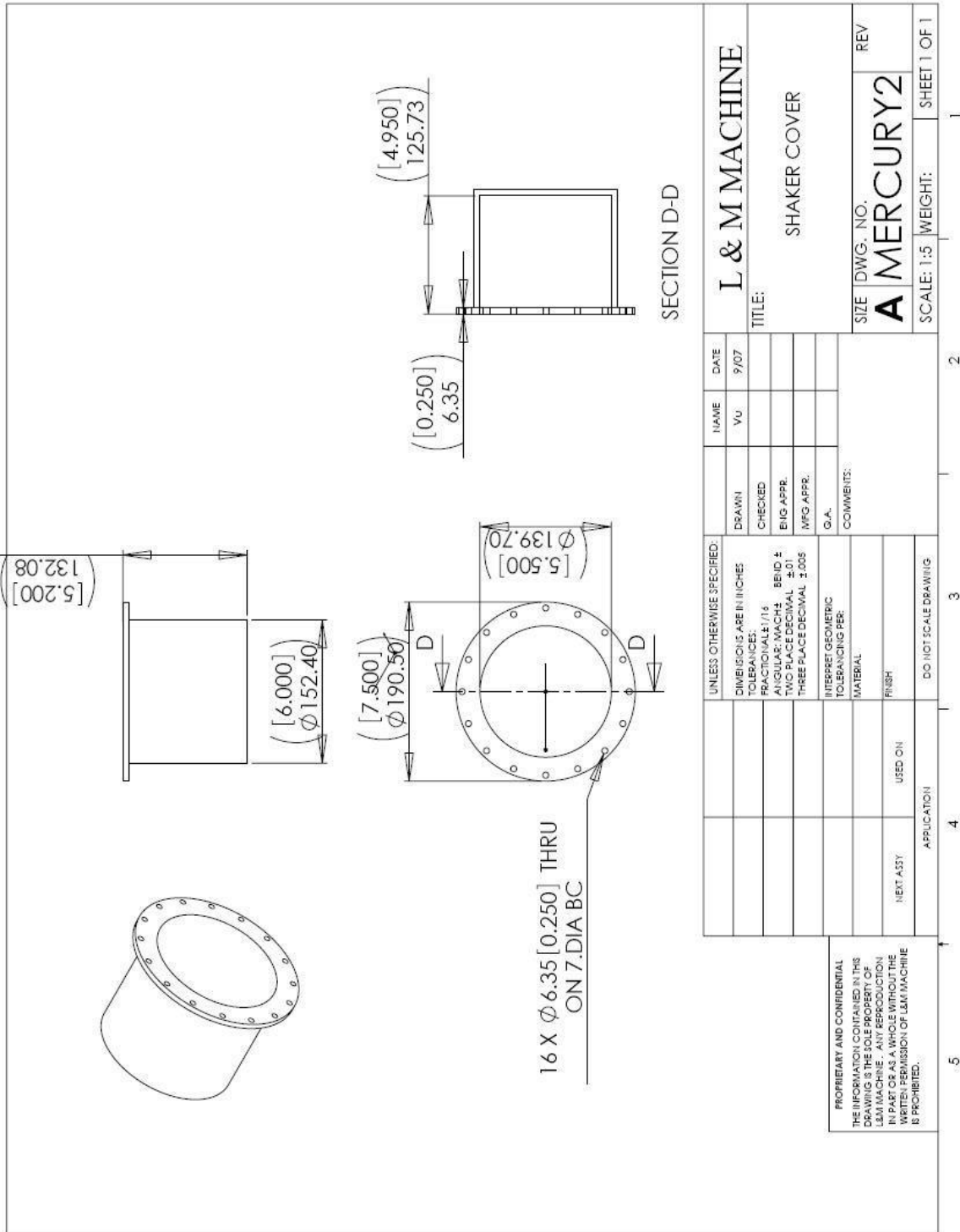


Figure A.7: Engineering drawing of the shaker cover

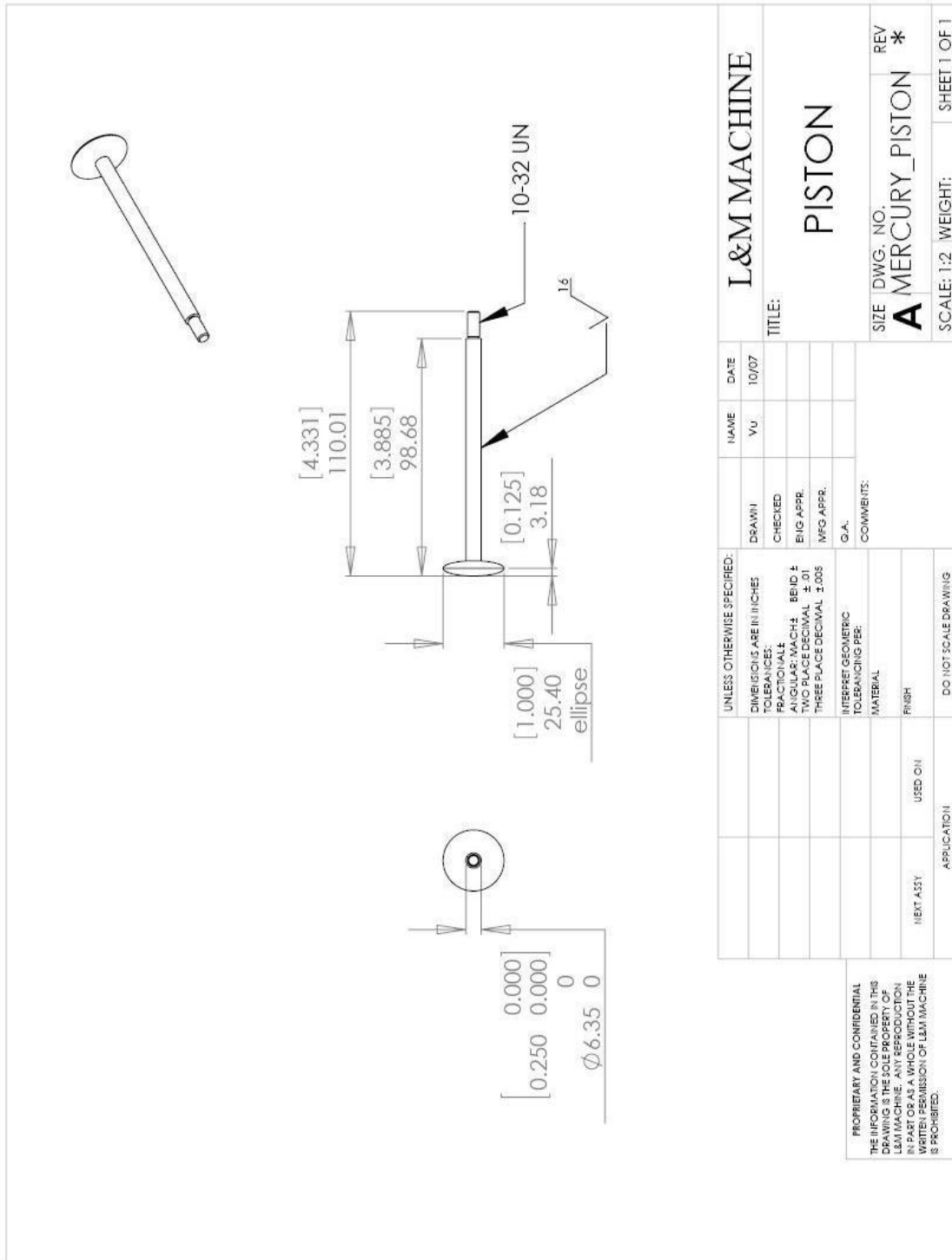


Figure A.8: Engineering drawing of the piston driver

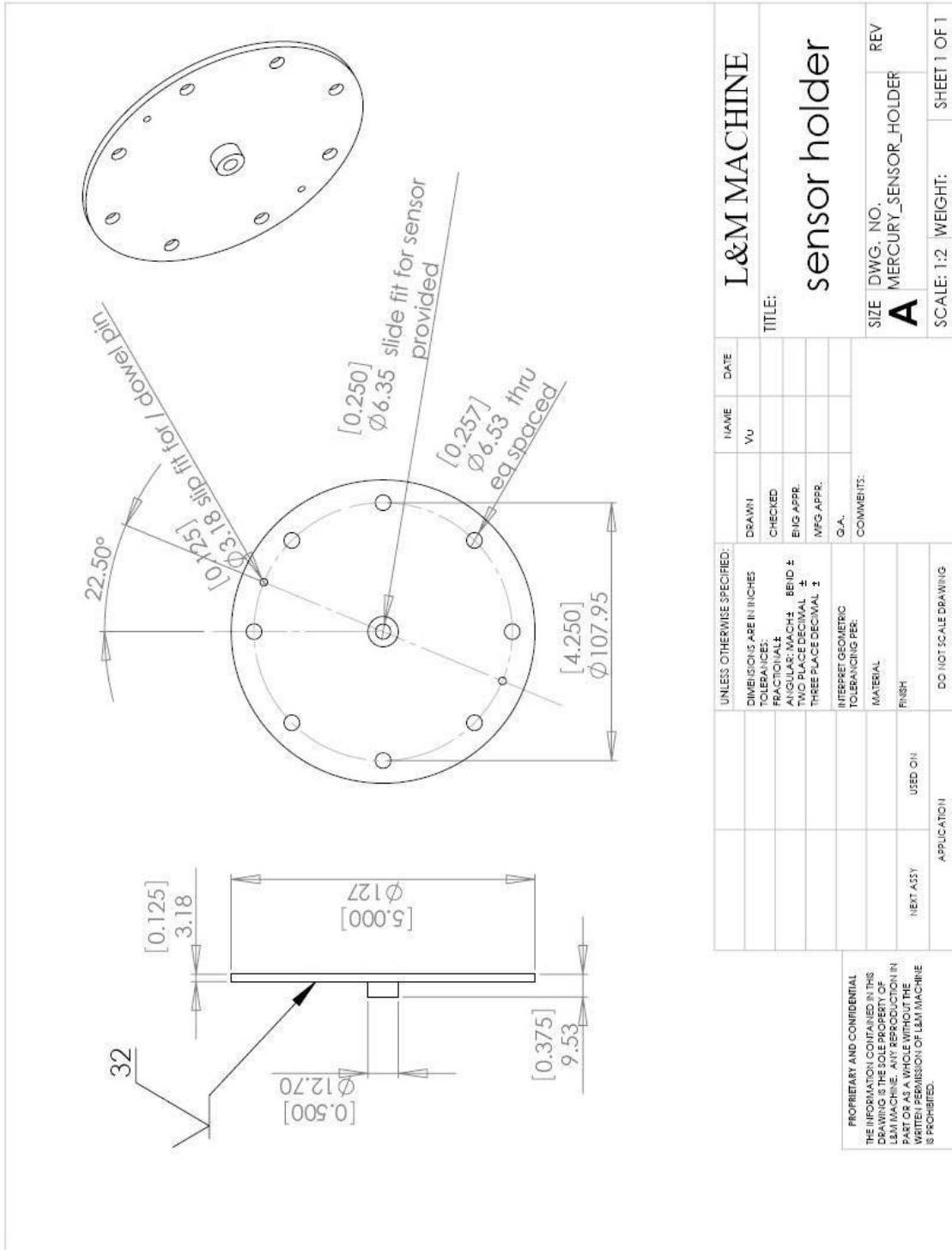


Figure A.9: Engineering drawing of the thin end plate

Bibliography

1. Plesset, M.S. and S.A. Zwick, *The growth of vapor bubbles in superheated liquids*. Journal of Applied Physics, 1954. **25**(4): p. 493-500.
2. Rayleigh, *On the pressure developed in a liquid during the collapse of a spherical cavity*, in *Philosophical Magazine*. 1917. p. 94-98.
3. Plesset, M.S., and Andrea Prosperetti, *Bubble dynamics and cavitation*. Annual Review of Fluid Mechanics, 1977. **9**: p. 145-185.
4. Plesset, M.S. and R.B. Chapman, *Collapse of an initially spherical vapour cavity in the neighbourhood of a solid boundary*. Journal of Fluid Mechanics, 1971. **47**(02): p. 283-290.
5. Lauterborn, W. and H. Bolle, *Experimental investigations of cavitation-bubble collapse in the neighbourhood of a solid boundary*. Journal of Fluid Mechanics, 1975. **72**(02): p. 391-399.
6. Futakawa, M., et al., *Pitting damage formation up to over 10 million cycles*. Journal of Nuclear Science and Technology, 2003. **40**(11): p. 895-904.
7. Futakawa, M., et al., *Pitting damage by pressure waves in a mercury target*. Journal of Nuclear Materials, 2005. **343**: p. 70-80.
8. Futakawa, M., et al., *Micro-impact damage caused by mercury bubble collapse*. Japan Society of Mechanical Engineering International Journal, 2005. **48**(4): p. 234-239.
9. Kogawa, H., et al., *Numerical study on pressure wave propagation in a mercury loop*. Journal of Nuclear Materials, 2008. **377**: p. 195-200.

10. Haines, J.R., B. W. Riemer, D. K. Felde, J. D. Hunn, S. J. Pawel and C. C. Tsai, *Summary of cavitation erosion investigations for the SNS mercury target*. Journal of Nuclear Materials, 2005. **343**: p. 58-69.
11. Riemer, B., *Status report on mercury target related issues*. Oak Ridge National Laboratory Technical Report, 2002(SNS-101060100-TR0006-R00).
12. Futakawa, M., et al., *Effects of pitting damage on fatigue limit and lifetime in mercury target*. Journal of Nuclear Materials, 2006. **356**(1-3): p. 168-177.
13. Futakawa, M., et al., *Pressure wave issues in high power mercury target*. Nuclear Instruments and Methods in Physics Research, 2006. **562**(2): p. 676-679.
14. Futakawa, M., et al., *Cavitation damage prediction for spallation target vessels by assessment of acoustic vibration*. Journal of Nuclear Materials, 2008. **377**: p. 182-188.
15. Okita, K., S. Takagi, and Y. Matsumoto, *(In Japanese)*. Nihon Kikai Gakkai Ronbunshu B, 2006. **72**(716): p. 885.
16. Futakawa, M., et al., *Cavitation erosion by proton beam bombarding mercury target for spallation neutron source: Damage potential evaluation by measuring acoustic vibration*. Sixth International Symposium on Cavitation, 2006.
17. Ida, M., *Suppression of cavitation inception by gas bubble injection: A numerical study focusing on bubble-bubble interaction*. Physical Review, 2007. **76**(046309): p. 1-10.

18. Lu, T., R. Samulyak, and J. Glimm, *Direct numerical simulation of bubbly flows and application to cavitation mitigation*. Journal of Fluids Engineering, 2007. **129**: p. 595-604.
19. Futakawa, M., et al., *Mitigation technologies for damage induced by pressure waves in high-power mercury spallation neutron sources: Bubbling effect to reduce pressure wave*. Journal of Nuclear Science and Technology, 2008. **45**(10): p. 1041-1048.
20. Naoe, T., M. Ida, and M. Futakawa, *Cavitation damage reduction by microbubble injection*. Nuclear Instruments and Methods in Physics Research, 2008. **586**: p. 382-386.
21. Okita, K., et al., *Numerical study on a mitigation strategy using micro bubbles for cavitation erosion caused by a thermal shock in liquid mercury*. Sixth International Symposium on Cavitation, 2006: p. 1-10.
22. Riemer, B.W., et al., *Requirements for a high-power target test facility*. Nuclear Instruments and Methods in Physics Research, 2006. **562**: p. 921-923.
23. Okita, K., S. Takagi, and Y. Matsumoto, *Propagation of pressure waves, caused by a thermal shock, in liquid metals containing gas bubbles*. Journal of Fluid Science and Technology, 2008. **3**(1): p. 116-128.
24. Kogawa, H., et al., *Effect of wettability on bubble formation at gas nozzle under stagnant condition*. Journal of Nuclear Materials, 2008. **377**: p. 189-194.
25. Maxwell, J.C., *A Treatise on Electricity and Magnetism*. Vol. 1. 1892: Oxford.
26. Lamarre, E.a.W.K.M., *Instrumentation for the measurement of void-fraction in breaking waves: Laboratory and field results*. IEEE Journal of Oceanic Engineering, 1992. **17**(2): p. 204-215.

27. Dong, F., et al., *Two methods for measurement of gas-liquid flows in vertical upward pipe using dual-plane ERT system*. IEEE Transactions on Instrumentation and Measurement, 2006. **55**(5): p. 1576-1586.
28. Merilo, M., R.L. Dechene, and W.M. Cichowlas, *Void fraction measurement with a rotating electric field conductance gauge*. ASME Journal of Heat Transfer, 1997. **99**: p. 330.
29. Huang, Z., B. Wang, and H. Li, *Application of electrical capacitance tomography to the void fraction measurement of two-phase flow*. IEEE Transactions on Instrumentation and Measurement, 2003. **52**(1): p. 7-12.
30. Filippov, Y.P., *Characteristics of horizontal two-phase helium flows Part 1: Flow patterns and void fraction*. Cryogenics, 1999. **39**: p. 59-68.
31. Chien, K.H., et al., *Void fraction measurement using the side-tube method*. Flow Measurement Instrumentation, 1997. **8**(2): p. 103-112.
32. Ma, Y., et al., *Two simplified methods to determine void fractions for two-phase flow*. Nuclear Technology, 1991. **94**(1): p. 124-133.
33. Silberman, E., *Sound velocity and attenuation in bubbly mixtures measured in standing wave tubes*. The Journal of the Acoustical Society of America, 1957. **29**(8): p. 925-933.
34. Pike, R.W., B.J. Wilkins, and H.C. Ward, *Measurement of the void fraction in two-phase flow by X-ray attenuation*. American Institute of Chemical Engineers Journal, 1965. **11**(5): p. 794-800.
35. Harvel, G.D., et al., *Cross-sectional void fraction distribution measurements in a vertical annulus two-phase flow by high-speed X-ray computed tomography*

- and real-time neutron radiology techniques*. Flow Measurement and Instrumentation, 1999. **10**: p. 259-266.
36. Thiyagarajan, T.K., et al., *Gamma-ray attenuation method for void fraction measurement in fluctuating two-phase liquid metal flows*. Measurement Science Technology, 1991. **2**: p. 69-74.
 37. Hibiki, T., K. Mishima, and H. Nishihara, *Measurement of radial void fraction distribution of two-phase flow in a metallic round tube using neutrons as microscopic probes*. Nuclear Instruments and Methods in Physics Research, 1997. **399**: p. 432-438.
 38. Wilson, P.S., *Sound propagation and scattering in bubbly liquids*. 2002, PhD Dissertation, Boston University.
 39. Ruggles, A.E., et al., *An investigation of the propagation of pressure perturbations in bubbly air/water flows*. ASME Journal of Heat Transfer, 1988. **110**(2): p. Pages: 494-499.
 40. Mallock, A., *The damping of sound by frothy liquids*. Proceedings of the Royal Society, 1910. **84**(A572): p. 391-395.
 41. Wood, A.B., *A Textbook of Sound*. 1st ed. 1930, New York: MacMillan.
 42. Minnaert, M., *On musical air bubbles and the sounds of running water*. The London, Edinburgh, and Dublin Philosophical Magazine and Journal of Science, Series 7, 1933. **16**: p. 235-248.
 43. Carey, W.M., *A Review of the Sonic Properties of Bubbly Liquids, in Unpublished Appendix Draft*. 2006.

44. Caflisch, R.E., et al., *Effective equations for wave propagation in bubbly liquids*. Journal of Fluid Mechanics, 1985. **153**: p. 259-273.
45. Wijngaarden, L.v., *On the equations of motion for mixtures of liquid and gas bubbles*. Journal of Fluid Mechanics, 1968. **33**(3): p. 465-474.
46. Prosperetti, A., L.A. Crum, and K.W. Commander, *Nonlinear bubble dynamics*. The Journal of the Acoustical Society of America, 1988. **83**: p. 502-513.
47. Keller, J.B. and M. Miksis, *Bubble oscillations of large amplitude*. The Journal of the Acoustical Society of America, 1980. **68**(2): p. 628-633.
48. Foldy, L.L., *The multiple scattering of waves*. Physical Review, 1945. **67**(3/4): p. 107-119.
49. Carstensen, E.L. and L.L. Foldy, *Propagation of sound through a liquid containing bubbles*. The Journal of the Acoustical Society of America, 1947. **19**(3).
50. Commander, K.W. and A. Prosperetti, *Linear pressure waves in bubbly liquids: Comparison between theory and experiments*. The Journal of the Acoustical Society of America, 1989. **85**(2): p. 732-746.
51. Hsieh, D.-Y. and M.S. Plesset, *On the propagation of sound in a liquid containing gas bubbles*. The Physics of Fluids, 1961. **4**(8): p. 970-975.
52. Wijngaarden, L.v., *One-dimensional flow of liquids containing small gas bubbles*. Annual Review of Fluid Mechanics, 1972. **4**: p. 369-396.
53. Gibson, F.W., *Measurement of the effect of air bubbles on the speed of sound in water*. The Journal of the Acoustical Society of America, 1970. **48**(5): p. 1195-1197.

54. Cheyne, S.A., C.T. Stebbings, and R.A. Roy, *Phase velocity measurements in bubbly liquids using a fiber optic laser interferometer*. The Journal of the Acoustical Society of America, 1995. **97**(3): p. 1621-1624.
55. Blackstock, D.T., *Fundamentals of Physical Acoustics*. 5th ed. 2000: Wiley-IEEE.
56. Redwood, M., *Mechanical waveguides*. 1960, Oxford: Pergamon.
57. Del Grosso, V.A., *Analysis of multimode acoustic propagation in liquid cylinders with realistic boundary conditions: Applications to sound speed and absorption measurements*. *Acustica*, 1971. **24**(6): p. 299-307.
58. Lafleur, L.D. and F.D. Shields, *Low-frequency propagation modes in a liquid-filled elastic tube waveguide*. The Journal of the Acoustical Society of America, 1995. **97**(3): p. 1435-1445.
59. Wilson, P.S., et al., *Gassy sediment acoustics: Low-frequency sound speed measurements paired with computer x-ray tomography imaging in reconstituted natural sediments*. The Journal of the Acoustical Society of America, 2006. **119**(5): p. 3448.
60. Wendel, M., et al. *Gas bubble formation in stagnant and flowing mercury*. in *Proceedings of FEDSM2007: 5th Joint ASME/JSME Fluids Engineering Conference*. 2007. San Diego, CA, USA.
61. Nicholas, M., R. A. Roy, L. A. Crum, H. Oguz, and A. Prosperetti, *Sound emissions by a laboratory bubble cloud*. The Journal of the Acoustical Society of America, 1994. **95**(6): p. 3171-3182.
62. Karichev, Z.R. and A.L. Muler, *Dissolution of gas bubbles moving in a liquid*. *Theoretical Foundations of Chemical Engineering*, 2006. **40**(1): p. 96-99.

63. Shedd, T.A., *General model for estimating bubble dissolution and droplet evaporation times*. Journal of Microlithography, Microfabrication, and Microsystems, 2005. **4**(3): p. 033004-1 - 033004-8.

Vita

Christopher Edward Ormonde was born in 1984 at the Newton-Wellesley Hospital in Newton, MA. He is the only child of Henry Edward and Lesley Jean Ormonde. Christopher grew up in Wayland, MA, and attended and graduated from Wayland High School in 2002. In the fall of 2002, he moved to Boston, MA, to attend Boston University. During the first three summers, Christopher taught model rocketry, basic math, and physics to gifted 5th through 9th graders at a renowned summer camp for bright students. During the latter two summers, Christopher worked as a mechanical engineering intern for the army at the Natick Soldier Center in Natick, MA. Christopher Graduated *magna cum laude* from Boston University with a Bachelor of Science in Mechanical Engineering in 2006.

In the fall of 2006, he re-matriculated at Boston University to pursue his graduate studies in Mechanical Engineering, where he took acoustics and fluids courses, worked as a teaching assistant, and became a Research Assistant under Professor Ronald A. Roy, primarily, as well as Robin O. Cleveland and R. Glynn Holt.

Christopher is an avid sport motorcyclist in his free time and races in the Loudon Road Race Series and Championship Cup Series. He permanently resides at 213 W. Plain St., Wayland, MA 01778.

A curriculum vitae follows on the next page.

Christopher Edward Ormonde

213 W. Plain St., Wayland, MA 01778 • Cell # 508-868-0404 • chrisceo@bu.edu

EDUCATION

Boston University, College of Engineering, Boston MA

Master of Science, Mechanical Engineering

May 2009

Thesis: "A Flow-through Acoustic Waveguide for Two-phase Bubbly Flow Void Fraction Measurement"

GPA: 3.8/4.0

Bachelor of Science, Mechanical Engineering

May 2006

Dean's List for seven semesters

Senior capstone design project: A DVT (Deep Vein Thrombosis) prevention device for use on commercial aircraft

GPA: 3.5/4.0

MEMBERSHIP

ASA (Acoustical Society of America) Member

ASME (American Society of Mechanical Engineers) Member

Former Vice-President of BU chapter of Pi Tau Sigma (Mechanical Engineering Honors Fraternity)

Tau Beta Pi (Engineering Honors Fraternity) Member

National Society of Collegiate Scholars member

SELECTED PUBLICATIONS AND PRESENTATIONS

- Christopher E. Ormonde, Seth B. Cohen, Parag V. Chitnis, Robin O. Cleveland, Ronald A. Roy, and R. Glynn Holt, "Resonant bubble effects in void fraction measurements from modal frequencies of a bubbly impedance tube", JASA 122(5), 2992-2992 (2007)
- Roy, Ronald A.; Ormonde, Christopher E.; Chitnis, Parag V.; Cleveland, Robin O.; Holt, R. Glynn, "An acoustic resonator for determining the void fraction of bubbly mercury flows", JASA 123(5), 3559 (2008)
- Christopher E. Ormonde, Parag V. Chitnis, Robin O. Cleveland, R. Glynn Holt, and Ronald A. Roy; "A Vertical Acoustic Waveguide for Two-phase Mercury-helium Flow Void Fraction Determination", ASME IMECE Congress, Track 10, Topic 31, Session 2; (2008)

WORK EXPERIENCE

Boston University, Boston, MA

Research Fellow

Spring 2007 - Present

- Designed, constructed, and tested a flow-through acoustic resonator for determining the void fraction of two-phase mercury-helium flow
- This work is supported by the DOE (Department of Energy) for study into the mitigation of cavitation damage to the ORNL (Oak Ridge National Laboratory) SNS (Spallation Neutron Source) mercury target chamber.
- The device will ultimately be taken to the SNS for implementation in their TTF (Target Test Facility)

Boston University, Boston, MA

Teaching Fellow

Fall 2006

- For an undergraduate thermodynamics course: Taught discussion and review sections, and led lab sessions. Provided one-on-one help to students for homework, labs, and exam-preparation. Graded homework, tests, and labs
- For an undergraduate compressible aerodynamics course: Developed a new lab for the course in MATLAB, creating a GUI (Graphic User Interface) allowing the students to remotely run a CFD (Computational Fluid Dynamics) simulation for flow around various airfoils and view the effects of changing parameters. The code used PuTTY to send information to an off-site supercomputer to run the CFD code and return the completed simulation for analysis

US Army Natick Soldier Center, Natick, MA

Mechanical Engineer

Summer 2005 - Winter 2006 (Part Time)

- Engineering summer/part-time hire on the Joint Precision AirDrop System (JPADS) team. The JPADS team develops autonomously guided precision cargo airdrop systems ranging from 500 to 60,000 pounds capable of just-in-time resupply for our forces. Systems are in use by our soldiers in the Middle East; millions of pounds of ammo and supplies have been dropped into the area of threat to date
- Performed modeling analysis of airdrop sequences using the NASA-developed Decelerator System Simulation Application (DSSA) software. Using collected data, airdrop behavior for system modifications can be predicted
- Took part in two operational test weeks at the US Army Yuma Proving Ground (YPG), Yuma, Arizona, providing instrumentation installation and analysis, system recovery, cargo system rigging, mission and aircraft loadings